Nanoscale Spatial Distribution of Supported Nanoparticles Controls Activity and Stability in Powder Catalysts

Alexander Holm,[†,‡,*] Emmett D. Goodman,[†] Joakim Halldin Stenlid,[‡] Aisulu Aitbekova,[†] Rosadriana Zelaya,[†] Benjamin T. Diroll,[§] Aaron C. Johnston-Peck,[‖] Kun-Che Kao,[†] Curtis W. Frank,[#] Lars G. M. Pettersson,[‡] Matteo Cargnello[†,*]

[†] Department of Chemical Engineering and SUNCAT Center for Interface Science and Catalysis, Stanford University, Stanford, CA 94305, USA

[‡] Department of Physics, AlbaNova University Center, Stockholm University, SE-106 91 Stockholm, Sweden

[§] Center for Nanoscale Materials, Argonne National Laboratory, 9700 S. Cass Avenue, Lemont, Illinois 60439, USA

[#] Department of Chemical Engineering, Stanford University, Stanford, CA 94305, USA

[‖] Material Measurement Laboratory, National Institute of Standards and Technology, Gaithersburg, MD, 20899, USA

Corresponding Authors

*E-mail: mcargnello@stanford.edu

*E-mail: alexander.holm@fysik.su.se

ABSTRACT

Supported metal nanoparticles are essential components of high-performing catalysts, and their structures are intensely researched. In comparison, nanoparticle spatial distribution in powder catalysts is conventionally not quantified, and the influence of this collective property on catalyst performance remains poorly investigated. Here, we demonstrate a general colloidal self-assembly method to control uniformity of nanoparticle spatial distribution on common industrial powder supports. We quantify distributions on the nanoscale using image statistics and show that the type of nanospatial distribution determines not only the stability, but also the activity of heterogeneous catalysts. Widely investigated systems (Au-TiO_2 for CO oxidation thermocatalysis and Pd-TiO_2 for H_2 evolution photocatalysis) were used to showcase the universal importance of nanoparticle spatial organization. Spatially and temporally resolved microkinetic modelling revealed that non-uniformly distributed Au nanoparticles suffer from local depletion of surface oxygen—and therefore lower CO oxidation activity—compared to uniformly distributed nanoparticles. Nanoparticle spatial distribution also determines stability of Pd-TiO_2 photocatalysts, because non-uniformly distributed nanoparticles sinter while uniformly distributed nanoparticles do not. This work introduces new tools to evaluate and understand catalyst collective (ensemble) properties in powder catalysts, thereby paving way to more active and stable heterogeneous catalysts.

INTRODUCTION

Nanoparticles (NPs) are key components in heterogeneous catalysts, owing to properties that differ from bulk materials such as quantum effects and high numbers of undercoordinated atoms.[1,2] These properties stem from unique NP structural features such as tunable size, shape and composition.[3,4] However, some important NP properties arise not from their individual structure but from their collective behavior, which is determined by the NP spatial organization.[5] As an example, spectroscopic signals from surface plasmon resonance or Raman scattering are greatly modified when NPs in solution aggregate and the spectra are dependent on the NP spatial organization in the aggregates, opening many new characterization opportunities.[6,7] Collective behavior also appears in two-dimensional films of ferromagnetic NPs where the magnetic field of each NP becomes weaker as the assemblies become denser.[8] Thus, NP collective properties are pervasive in seemingly disparate disciplines, with further examples being mechanical behavior of NP-polymer composites[9] and exciton coupling in NP superstructures.[10] Although established in nanoscience, NP collective properties in heterogeneous catalysts have received little attention.

Heterogeneous catalysts are usually developed with focus on the supported NP structure.[11–15] This is reasonable, since the NP and/or NP-support interface provides active sites where reactants interact to lower the reaction activation energy.[15] However, because heterogeneous catalysts consist of enormous ensembles of individual NPs, collective properties could also influence catalyst performance. It was recently shown in model planar systems that the distance between supported NPs can influence the local microkinetics through effects such as hydrogen spillover.[16] Thus, NP spatial distribution may influence activity in realistic (powder) catalysts because different NP spatial distributions should give different distributions of local microkinetics, in turn giving different overall catalytic rates. In addition, particle growth[17–19] and atomic redispersion[20] are also strongly dependent on the interparticle distance so the type of NP spatial distribution may also impact catalyst stability.[17] The influence of NP spatial distribution on catalyst performance in powder catalysts remains essentially unexplored because conventional catalyst preparation has not allowed varying spatial distribution of supported NPs without simultaneously changing their size distribution.[17,21–23] Thus, because NP size strongly influences both activity[24–27] and stability,[28–30] it has been challenging to deconvolute NP distribution effects from NP size effects.[17,23] Still, there has been a small number of studies attempting to correlate NP spatial

distribution to stability of thermocatalysts. Unfortunately, the catalysts in these studies had both different spatial and size distribution of NPs,[17,23] which makes elucidation of correlation between NP spatial distribution and catalyst stability difficult (since NPs of different size distributions also sinter at different rates[28–30]).

To accurately study the influence of NP spatial distribution on catalysis, realistic catalysts must be prepared that have different distributions, but are otherwise identical. Here we present a colloidal self-assembly method to change NP spatial distribution on common industrial supports (such as TiO_2 and Al_2O_3) without changing weight loading, NP size distribution or other NP structural properties. Using this novel approach, we demonstrate that NP spatial distribution strongly influences both activity and stability in heterogeneous thermo- and photocatalysis. Moreover, we show that non-uniform distributions—distinguished by log-normally distributed NPs—commonly found in heterogeneous catalysts are not optimal, but that uniform distributions—distinguished by normally distributed NPs—give better catalytic performance. Because NP spatial distribution scarcely has been investigated, new quantities must be introduced to characterize this collective property. We introduce NP number-density as an easily measured quantity with predictive power for catalyst performance.

RESULTS AND DISCUSSION

Control and Characterization of NP Spatial Distributions. The most common catalyst preparation techniques, impregnation-drying and coprecipitation are cheap and versatile and therefore used across industry and academia.[3] In impregnation-drying, supports are impregnated with a metal salt solution and then dried to form the catalyst, while in coprecipitation separate salt solutions of metal and support are mixed with ensuing precipitation of solid catalyst.[3] Unfortunately, these techniques frequently result in NP spatial distributions that are non-uniform and uncontrolled on the nanoscale.[3,17,21–23,31–40] As an example, industrially relevant cobalt Fischer–Tropsch catalysts prepared by impregnation-drying exhibit significant nanoscale clustering with many NPs in some regions, but few in others.[36,37] More uniform NP spatial distributions have been achieved by judiciously modifying the drying atmosphere, but NP size distributions were not conserved.[17,21] To isolate the influence of NP spatial distribution from size distribution, we propose an alternative approach, using pre-synthesized NPs to generate different

spatial distributions. In this work, we used colloidal methods to prepare catalysts with varied nanoparticle spatial distributions that led to different catalytic properties (Figure 1). Colloidal Au NPs (3.2 nm +/- 0.5 nm, Figure 1 A) and Pd NPs (3.8 nm +/- 0.2 nm, Figure 1 B) were synthesized in organic solvents (Experimental Section) with oleylamine as a stabilizing ligand. As is conventional,[3,20,41–43] the NPs were then deposited onto TiO_2 by direct addition to the support grains, also in organic solvent. This protocol, similarly to what is frequently observed with impregnation-drying or coprecipitation,[3,17,21–23,31–40] gave non-uniform distribution on supports with some regions having many, and others few NPs (Figure 2 summarizes particle distributions for the samples shown in Figure 1; more below). Because of their non-uniform distributions, the conventionally impregnated samples, labelled Au-TiO_2-C and Pd-TiO_2-C, represent conditions typically observed in heterogeneous catalysts (Figure 2 B,D,H,J).[3,17,21–23,31–40]

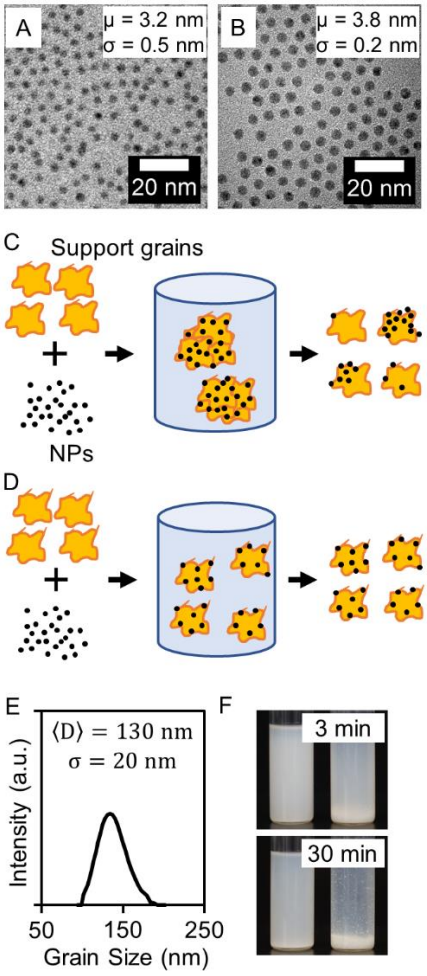

Figure 1. Conventional and surfactant-assisted deposition of NPs onto TiO_2. **(A)** TEM micrograph of Au NPs and **(B)** of Pd NPs. NP size distributions are included in Figure S1. **(C)** Schematic illustration of conventional impregnation and **(D)** surfactant-assisted impregnation of NPs on metal oxide support grains. **(E)** DLS size distribution of TiO_2 grains in hexanes with surfactant. DLS measurement of TiO_2 in pure hexanes was not possible due to fast agglomeration and sedimentation of grains. **(F)** Photographs of TiO_2 dispersion in hexanes with surfactant (left) and in pure hexanes (right) at different times, 3 min and 30 min, after sonication.

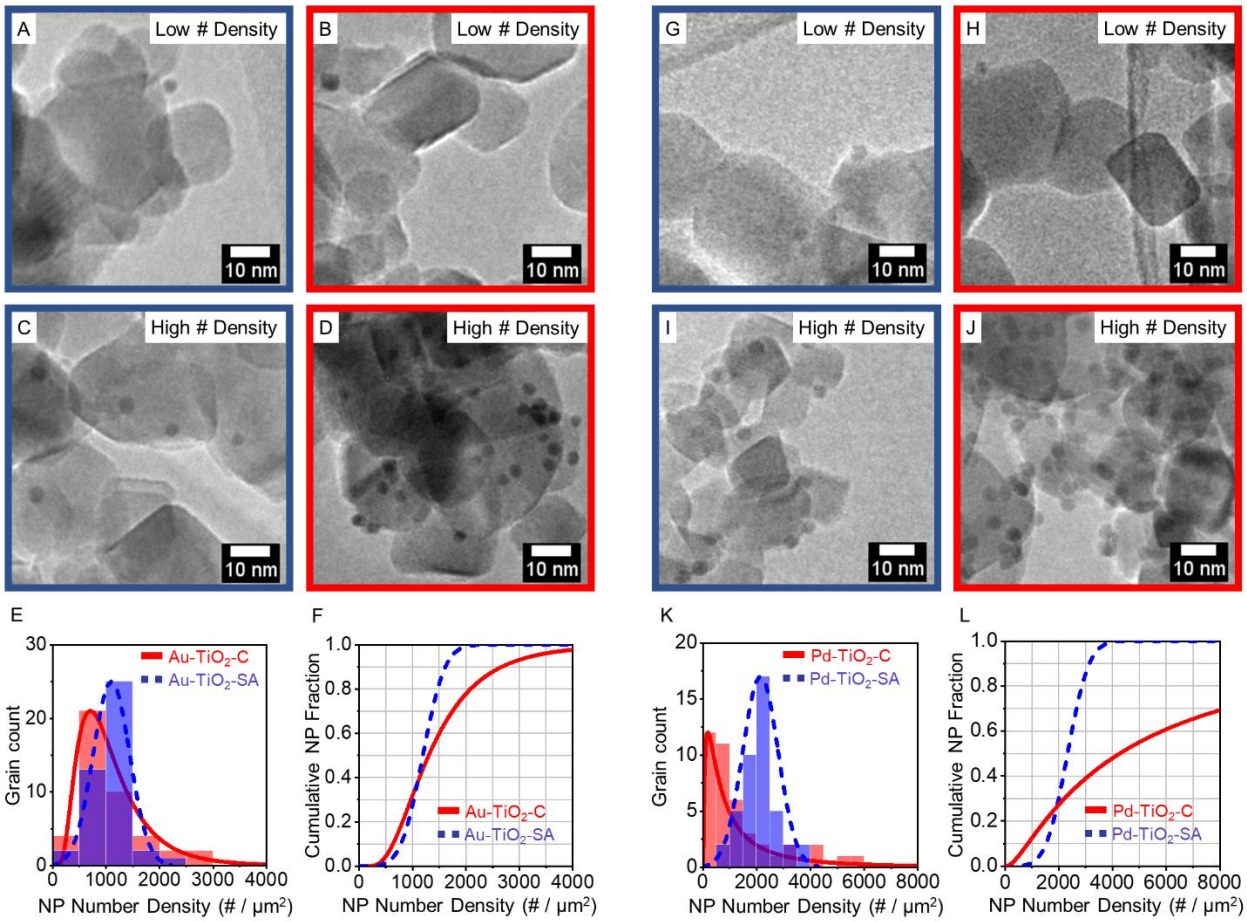

Figure 2. Statistics of NP spatial distributions. **(A, C)** Typical TEM micrographs of Au-TiO_2-SA and **(B, D)** Au-TiO_2-C exemplifying regions with low and high NP number-density. **(E)** NP number-density distributions of Au NPs on TiO_2 grains. Au-TiO_2-C has non-uniform, log-normal distribution (red curve), and Au-TiO_2-SA has uniform, normal distribution (blue, dashed curve). **(F)** Cumulative fractions of Au NPs vs NP number-density on Au-TiO_2-C, red curve and Au-TiO_2-SA, blue dashed curve. **(G, I)** Typical TEM micrographs of Pd-TiO_2-SA and **(H,J)** Pd-TiO_2-C exemplifying regions with low and high NP number-density. **(K)** NP number-density distributions of Pd NPs on TiO_2 grains. Pd-TiO_2-C has non-uniform, log-normal distribution (red curve), while Pd-TiO_2-SA has uniform, normal distribution (blue, dashed curve). **(L)** Cumulative fractions of

Pd NPs vs NP number-density on Pd-TiO_2-C, red curve and Pd-TiO_2-SA, blue dashed curve. The statistical parameters describing the normal, $\rho_{\#} \sim N(\mu, \sigma^2)$ and log-normal, $ln(\rho_{\#}) \sim N(\mu, \sigma^2)$, distributions in (E,K) are given in Table S1.

It is commonly thought that an optimal catalyst should consist of monodisperse, size-, shape- and composition-tunable NPs deposited on porous powder supports.[14,44,45] It is further thought, but rarely studied, that uniform NP spatial distributions are needed for optimal performance.[17,23] Colloidal synthesis affords monodisperse size-, shape- and composition-tunable NPs from a wide range of metals and is therefore ideally suited to produce catalysts.[4,44] However, the final step for obtaining optimal catalysts, namely a general method for uniform deposition of colloidal NPs is, until now, lacking. We hypothesized that the non-uniform NP distribution obtained by adding pre-synthesized NPs to support grains results from poor dispersion of the hydrophilic grains in organic solvent, such that large areas of the grains were not exposed to the solvent during impregnation (Figure 1 C). Consequently, we sought a method to better disperse the grains for more uniform NP deposition. Surfactants can be used to render hydrophilic mineral grains hydrophobic, a property frequently used to recover minerals by froth flotation in the mining industry.[46] We discovered that the appropriate choice of surfactant also makes common support grains (TiO_2 and Al_2O_3) hydrophobic and therefore dispersible in organic solvents, allowing uniform NP impregnations.

We used the surfactant sodium hexadecane sulfonate (NaHDS) to better disperse supports (Figure 1 D), which resulted in visually slowed sedimentation (Figure 1 F). Dynamic light scattering (DLS) measurements (Figure 1 E) further showed that the average size (≈130 nm) of TiO_2 grains suspended with surfactant was similar to the size of single grains observed by transmission electron microscopy (TEM) (Figure S2), suggesting that grain agglomeration was negligible. Here, we define a TiO_2 grain as a cluster of irreversibly fused primary TiO_2 nanoparticles. As hypothesized, addition of metal NPs to the suspension of surfactant stabilized TiO_2 resulted in more uniform NP spatial distributions (Figure 2 A,C,G,I). Surfactant-assisted impregnations, labelled Au-TiO_2-SA and Pd-TiO_2-SA, and conventional impregnations were made from the same NP stocks—Au and Pd respectively—such that catalysts only differed in NP spatial distribution and not in NP structural properties. After impregnation, all catalysts were thoroughly washed to remove surfactant (Experimental Section).

Spatial distribution of Cu/Zn NPs on porous silica has previously been quantified by measuring the distribution of nearest neighbor distances between particles using electron tomography which is time-consuming to implement.[17] However, although this quantity may be relevant for particle growth,[17] it fails to provide information on the local NP surface concentration in different spatial regions of catalyst and may therefore be less effective in rationalizing microkinetic effects. Moreover, to determine nearest neighbor distributions, distances must be measured for each particle. The time-consuming effort of image acquisition and analysis meant that only one support grain was evaluated,[17] which, considering statistical variance between grains, likely is not representative of the entire catalyst sample. Here we instead propose a novel quantitative description of NP spatial distributions that is more representative of the entire sample and that can be obtained from simple TEM images. Images of many individual support grains were acquired, the number of NPs on each grain counted and the projected grain area measured (Experimental Section). The NP number-density, $\rho_{\#}$, was then defined:

$$\rho_{\#} = \frac{Number\ of\ NPs}{Projected\ grain\ area\ (\mu m^2)} \qquad \text{(eqn. 1)}$$

This quantity captures both the local average interparticle distance, which is relevant for NP growth, and the local NP surface concentration, which is relevant for the microkinetic environment. NP spatial distributions were then described by mapping the NP number-densities across many TiO_2 support grains (Figure 2 E,K). A detailed discussion regarding the appropriateness of NP number-density for describing NP spatial distribution is given in the Supporting Section S1.

In the literature, electron microscopy is often used to support notions such as "uniform" or "non-uniform" NP spatial distributions without substantiating the terms with image statistics or other means.[3,33,43,47,48] Here, using the NP number-density distributions generated by image analysis, these qualitative notions could be quantified. The NP number-density in the uniform samples, Au-TiO_2-SA and Pd-TiO_2-SA, was normally distributed (eqn. 2 and Figure 2 E,K, blue curves) —while the NP number-density in the conventional samples, Au-TiO_2-C and Pd-TiO_2-C, was log-normally distributed (eqn. 3 and Figure 2 E,K, red curves).

$$\rho_{\#} \sim N(\mu, \sigma^2) \qquad \text{(eqn. 2)}$$

$$ln(\rho_{\#}) \sim N(\mu, \sigma^2) \qquad \text{(eqn. 3)}$$

Where $\rho_{\#}$ is the NP number-density, μ is the mean and σ is the standard deviation. In the case of uniform, normally distributed samples the average NP number-density, $\langle\rho_{\#}\rangle$, is identical to μ:[49]

$$\langle\rho_{\#}\rangle = \mu \qquad \text{(eqn. 4)}$$

while in the case of non-uniform, log-normally distributed samples $\langle\rho_{\#}\rangle$ is given by:[49]

$$\langle\rho_{\#}\rangle = exp\left(\mu + \frac{\sigma^2}{2}\right) \qquad \text{(eqn. 5)}$$

The average NP number-density in conventional and surfactant-assisted catalysts differed by less than 10 %, confirming that the catalysts only differed in NP spatial organization, not in number of NPs, which was also confirmed by inductively coupled plasma – mass spectrometry (ICP-MS) measurements. NP number-density averages, ICP-MS results and statistical parameters describing all samples are given in Table S1.

Thus, even though the catalysts were macroscopically identical, their nanoscale NP spatial distributions were strikingly different. To illustrate the difference between uniform, normal and non-uniform, log-normal distributions, the fractions of NPs residing in high NP number-density regions can be extracted from Figure 2 F and L. In Au-TiO_2-SA, only 1 % of NPs are in regions with more than 2000 NPs μm^{-2}, while 23 % of NPs are in such regions in Au-TiO_2-C. In Pd-TiO_2-SA, 1 % of NPs are in regions with more than 3800 NPs μm^{-2}, while 54 % of NPs are in such regions in Pd-TiO_2-C.

The normal distribution achieved by surfactant-assisted impregnation is a distinguishing feature of NP depositions with maximized interparticle spacing, because it suggests (by the central value theorem[49], see also Supporting Section S1) that NPs were equally probable to deposit on each support grain. The normal distribution of NP number-density thus corroborates that support grains were fully dispersed and exposed to solvent in the presence of NaHDS surfactant. In contrast, the log-normal distribution observed in the conventional samples indicates unequal probability[49] for NPs to deposit on different support grains, showing that grains were agglomerated in the impregnation solvent such that some grains were exposed, having high probability of NP attachment, while most grains were not exposed, having low probability of NP attachment.

Distribution-Dependent CO Oxidation Catalysis on Au-TiO_2. CO oxidation rates were measured at atmospheric pressure in a conventional quartz microreactor at 80 °C. The Au-TiO_2

catalysts were diluted with inert silicon carbide and high space velocities were used to eliminate heat and mass transfer limitations (Experimental Section). Interestingly, while oxidation rates, O_2 rate orders and activation energies were comparable to previous reports,[50–60] Au-TiO_2-SA showed substantially higher rate (≈ 2 x) than Au-TiO_2-C (Figure 3 A,B,C). Both catalysts deactivated to stable rates over time which is commonly observed with Au-TiO_2 catalysts,[51,55–57,61] but the relative rate enhancement remained (Figure 3 A). Deactivation of Au-TiO_2 during CO oxidation usually cannot be ascribed to particle growth, but to blocking of active sites by chemical species such as carbonates.[55,61] TEM image analysis demonstrated that NP size distributions also in our catalysts were identical before and after catalytic activity (Figure 3 D) and different activity between the samples due to Au NP size can thus be ruled out. Because catalysts differed only in their NP spatial distribution (Figure 2 E,F) the difference in rates can only be due to this collective property. Thus, our results establish the crucial importance of NP spatial distribution for optimizing not only stability,[17] but also activity of heterogeneous catalysts.

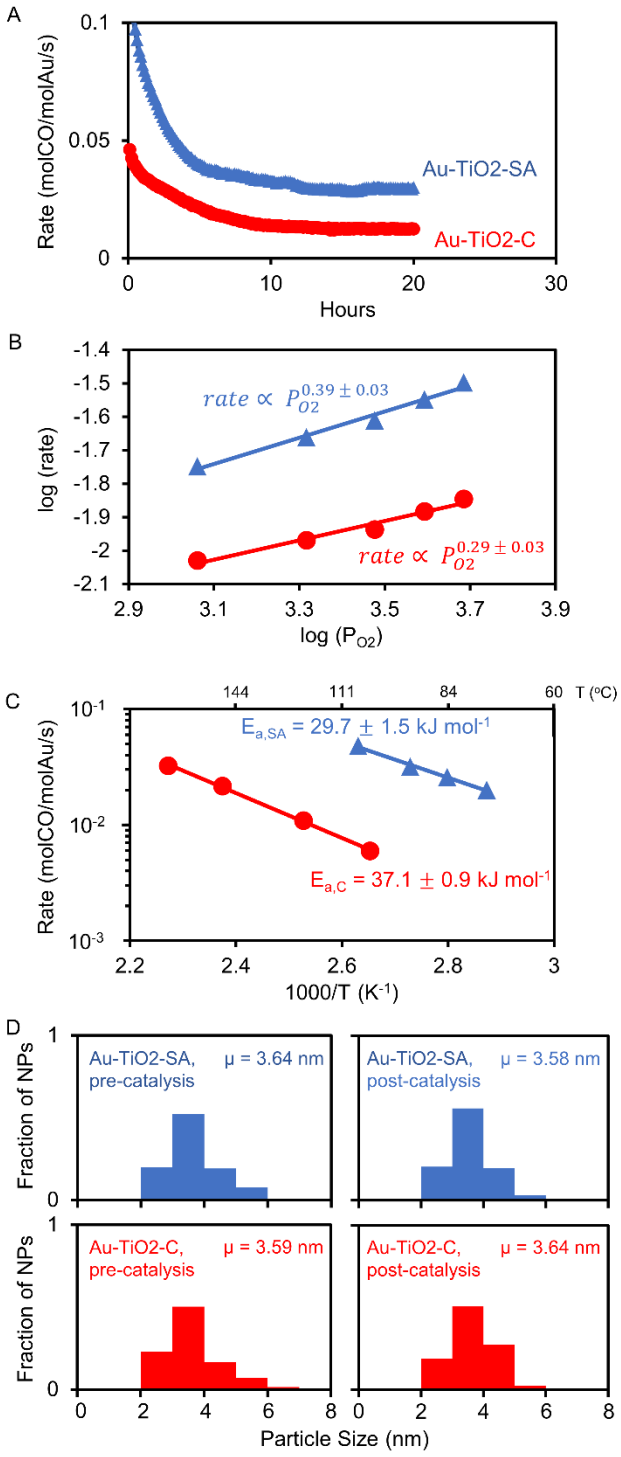

Figure 3. Distribution-Dependent CO Oxidation Catalysis on Au-TiO$_2$. (A) Transient CO oxidation rates on Au-TiO$_2$-SA, upper curve and Au-TiO$_2$-C, lower curve. Additional repeat measurements (Figure S3) show high reproducibility. **(B)** O_2 reaction orders measured after reaction rate stabilization on Au-TiO$_2$-SA, upper curve and Au-TiO$_2$-C, lower curve. **(C)** Arrhenius plots collected after reaction rate stabilization on Au-TiO$_2$-SA, upper curve and Au-

TiO_2-C, lower curve. The apparent activation energy of CO oxidation on Au-TiO_2-C (37.1 ± 0.9 kJ mol^{-1}) is higher than on Au-TiO_2-SA (29.7 ± 1.5 kJ mol^{-1}) with a 99.993 % confidence level (see Supporting Section S2). **(D)** Particle size distributions before and after catalytic activity for Au-TiO_2-SA and Au-TiO_2-C. Typical TEM images before and after catalytic activity are given in Figure S4.

To elucidate the experimentally observed rate dependence on NP spatial distribution, reaction mechanisms must be considered. Substantial evidence suggests that CO oxidation on Au-TiO_2 in dry conditions and slightly elevated temperatures (T ≥ 80 °C) occurs through the Au-assisted Mars-van Krevelen mechanism.[50,57,62–68] The full mechanism (Supporting Section S3) can be reduced to two steps, reduction and oxidation of the TiO_2 support:[64,68]

$$CO\ (g) + O_{act} \xrightarrow{k_{red}^{eff}} CO_2\ (g) + \square_{O_{act}} \qquad \text{(eqn. 6)}$$

$$O_2\ (g) + 2\ \square_{O_{act}} \xrightarrow{k_{ox}^{eff}} 2\ O_{act} \qquad \text{(eqn. 7)}$$

Equation (6) describes reduction of the TiO_2 surface by abstraction of surface lattice oxygen (O_{act}) with Au-adsorbed CO to form CO_2 and surface lattice oxygen vacancies ($\square_{O_{act}}$). Equation (7) describes re-oxidation of the TiO_2 surface by reaction of newly formed $\square_{O_{act}}$ and gaseous O_2. At 80° C, $\square_{O_{act}}$ diffusion rate is significantly smaller compared to O_{act} abstraction rate,[50] meaning that the surface coverage of $\square_{O_{act}}$ will be higher and O_{act} coverage lower in regions with high Au NP number-density than in regions with low NP number-density (Figure 4 A). A lower O_{act} coverage (a more reduced TiO_2 surface) is expected to result in higher activation energy for the CO_2 production step (eqn. 6).[69] A significantly larger fraction of NPs resides in high number-density regions in Au-TiO_2-C compared to in Au-TiO_2-SA (Figure 2 F). Thus, we propose that compared to Au-TiO2-SA, Au-TiO2-C has a larger fraction of NPs in regions with low O_{act} coverage under reaction conditions at steady-state, causing the experimentally observed (Figure 3 A, C) higher activation energy and lower overall catalytic rate.

To further unveil the role of O_{act} depletion on CO oxidation rates, we developed a spatially and temporally resolved microkinetic model for the Mars-van Krevelen mechanism. This mechanism has previously been microkinetically modelled, but without considering spatial variation of local microkinetics (i.e. without considering surface concentration gradients of reaction intermediates).[69] Here we developed a spatially resolved model by adding surface

diffusion of reaction intermediates to the previously proposed elementary steps[64] (see Supporting Section S3 for details).

Our model consists of two gold NPs, separated by a variable distance of TiO_2 surface (Figure 4 B). High NP number-density regions in the real catalysts are then represented by short distances between the gold regions in the model, while low NP number-density regions are represented by larger distances. NP separation in the model was varied between 0.5 nm and 20 nm, a range which at the low end represents high NP number-density regions in Au-TiO_2-C (Figure 2 D), and at the high end represents high NP number-density regions in Au-TiO_2-SA (Figure 2 C). The surface coverage of O_{act} during steady-state operation of the catalyst was then computed as a function of position between the Au regions (Figure 4 C). For larger Au separation (10 nm and 20 nm), the TiO_2 surface at the midpoint between the Au regions had identical O_{act} coverage (i.e. ≈ 100 %) under steady-state operation as during rest. However, O_{act} coverage at the Au-TiO_2 perimeter was decreased to ≈ 90 % during steady-state operation. More interestingly, at shorter Au separation, O_{act} coverage was further decreased, both at the perimeter and between the Au regions. The effect is seen already at an Au separation of 5 nm, after which the O_{act} steady-state coverage monotonically decreases with decreasing NP separation (Figure 4 C). Because O_{act} is a reacting species in the CO_2 production step (eqn. 6), lower O_{act} coverage near the Au-TiO_2 perimeter leads to lower CO oxidation rates. Moreover, a lower O_{act} coverage (a more reduced TiO_2 surface) leads to a higher activation barrier for the CO_2 production step,[69] further lowering CO oxidation rates (see Supporting Section S3 for details). Thus, at small Au separation the overall reaction rate is reduced ≈ 4-fold compared to larger Au separation (Figure 4 D).

The computational results are robust, as demonstrated by exploring a wide range of reaction barriers reported in the literature, with qualitatively similar results (Supporting Section S3). The results therefore support our hypothesis that local depletion of O_{act} in Au-TiO_2-C compared to in Au-TiO_2-SA causes lower overall CO oxidation rates. Our results suggest that discrepancy in the literature regarding CO oxidation activity over Au-TiO_2 may in part be due to differences in hierarchical organization of nanoparticles, with clustered Au NPs leading to lower CO oxidation rates. Moreover, this result is generalizable to many oxidation reactions proceeding by the Mars-van Krevelen mechanism, which includes oxidation over metal NPs on reducible supports (e.g. CeO_2, Fe_xO_y and ZrO_2).

In fact, all catalytic reactions where intermediates transport across the NP/support boundary potentially could exhibit a rate dependence on the NP spatial distribution. This is because in such reactions, different NP spatial distributions may give rise to different distributions of local microkinetics, and therefore different catalytic rates. Reactions where intermediates transport or react across the NP/support boundary include not only those of Mars-van-Krevelen type, but also all reactions involving spillover of adsorbed intermediates. The importance of such reactions is enormous and include for example hydrogenation, Fisher-Tropsch, ammonia and methanol synthesis.[70–73]

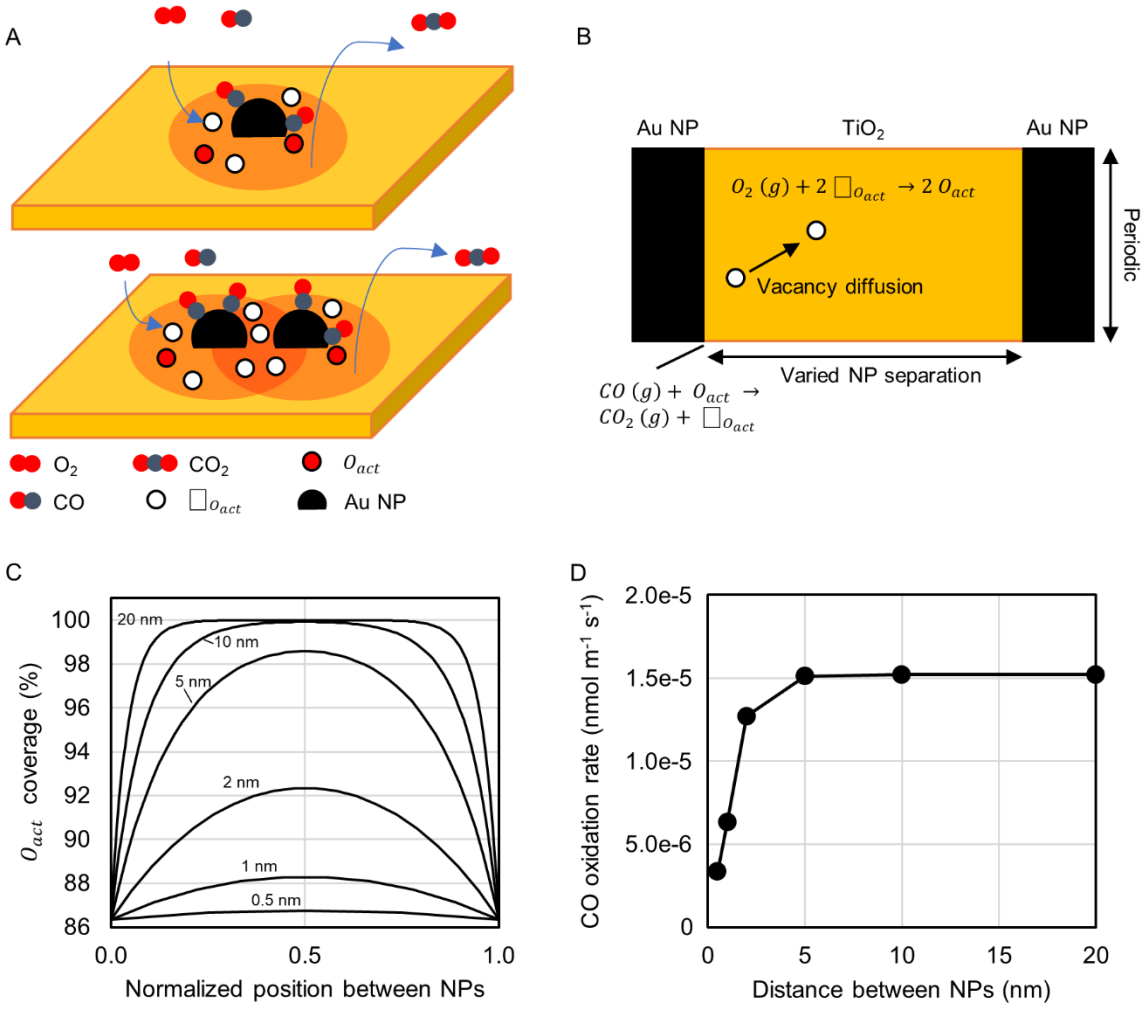

Figure 4. Spatially and temporally resolved microkinetic model of CO oxidation on Au-TiO_2. **(A)** Schematic illustration of reaction zones, illustrated in semi-transparent red, around NPs in a low NP number-density region (top) and high NP number-density region (bottom). Surface coverage of O_{act} is lower in the high NP number-density region because the reaction zones around individual NPs overlap to a larger degree than in low NP number-density regions. **(B)** Illustration

of model used for computational treatment. Our model consists of two Au regions, separated by a variable distance of TiO_2 surface. High NP number-density regions are thus represented by short distances between the gold regions, while lower NP number-density regions are represented by larger distances. **(C)** Surface coverage of O_{act} as a function of position between Au regions during steady-state CO oxidation. Plots were generated for different separations between Au regions ranging from 0.5 nm to 20 nm. **(D)** Steady-state CO oxidation rates (per meter of Au/TiO_2 perimeter) as a function of separation between Au regions.

Distribution-Dependent H_2 Evolution Photocatalysis on Pd-TiO_2. Photocatalytic measurements were carried out using a quartz photoreactor (Figures S5 and S6) irradiated with collimated light of wavelength 337 nm. Pd-TiO_2 photocatalysts were dispersed in 1:1 water:ethanol and transient H_2 evolution quantum efficiencies (QEs) were determined using an online gas-chromatograph (Experimental Section). No H_2 evolution was observed from Pd-TiO_2 in the dark, and no H_2 evolution was observed in irradiated suspensions of TiO_2 without Pd NPs. Thus, both light and Pd NPs are necessary for H_2 generation. Initial QEs were the same for Pd-TiO_2-C and Pd-TiO_2-SA (≈ 50 %) and similar to previous reports,[74–76] but Pd-TiO_2-C deactivated substantially quicker than Pd-TiO_2-SA such that after 20 h irradiation, QE was ≈ 30 % in the former and ≈ 40 % in the latter (Figure 5 A). Thus, our results underline that control of nanoscale NP spatial distribution is crucial not only in thermocatalysis, but also in photocatalysis.

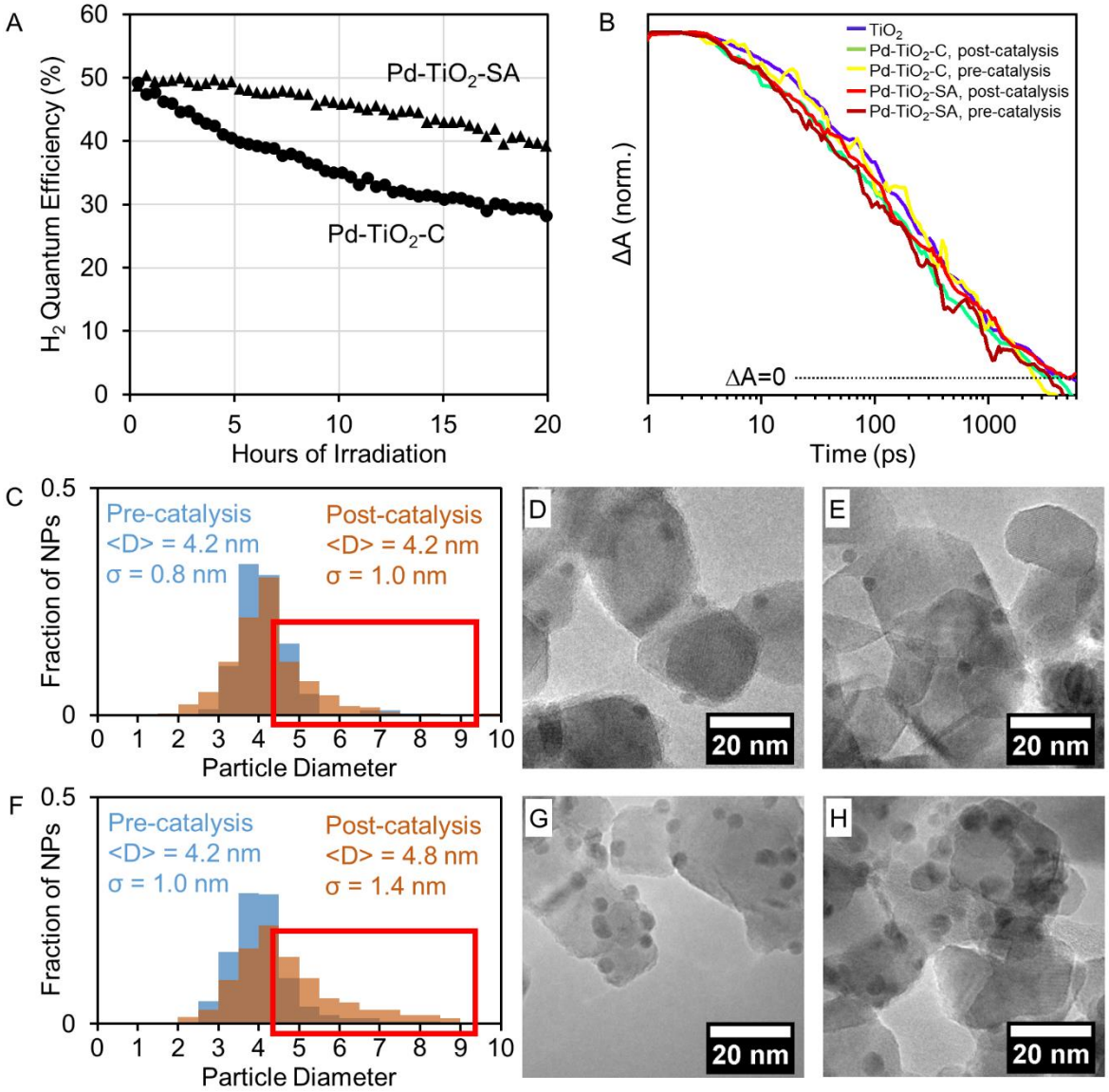

Figure 5. Distribution-Dependent H_2 Evolution Photocatalysis on Pd-TiO_2. (A) Transient H_2 production QEs with Pd-TiO_2-SA, upper curve and Pd-TiO_2-C, lower curve. Additional repeat measurements (Figure S7) show high reproducibility. **(B)** Transient absorption measured at 770 nm in 1:1 water:ethanol of pure TiO_2, Pd-TiO_2-SA and Pd-TiO_2-C before and after photocatalysis. Full spectra at 50 ps delay time are given in Figure S8. **(C)** Size distributions of Pd NPs on Pd-TiO_2-SA before (blue) and after (brown) catalysis. **(D)** TEM micrograph of high NP number-density region on Pd-TiO_2-SA before and **(E)** after catalysis. **(F)** Size distributions of Pd NPs on Pd-TiO_2-C before (blue) and after (brown) catalysis. **(G)** TEM micrograph of high NP number-density region on Pd-TiO_2-C before and **(H)** after catalysis. Boxed sections in the size distributions **(C, F)** are used to highlight the difference in particle growth between Pd-TiO_2-SA and Pd-TiO_2-C.

It is usually assumed that enhanced QEs with metal NPs on semiconductors result from improved charge separation via electron injection from semiconductor to metal.[74,77–80] This mechanism implies there is an optimal NP number-density,[77,79] in turn suggesting that uniform NP spatial distributions should result in higher QEs than non-uniform distributions. Thus, it is surprising that NP spatial distribution (Figure 2 K,L) does not influence initial activity (Figure 5), suggesting that electrons may not transfer to the NPs. To further investigate charge separation, we used transient absorption (TA) spectroscopy. A broad photoinduced absorption at 770 nm has been assigned to trapped electrons at the TiO_2 surface,[81] and if excited electrons are injected from TiO_2 to Pd, both a decrease in initial absorption and more rapid decay is expected with Pd-TiO_2 compared to pure TiO_2. However, catalysts both before and after photocatalytic activity and irrespective of NP spatial distribution showed similar initial absorption and decay transients as pure TiO_2 (Figure 5 B), similar to observations recently made on Au-TiO_2 and Pt-TiO_2 with TA and time-resolved fluorescence spectroscopies.[80] The result suggests that electrons are not injected into Pd NPs.

Our results suggest that for Pd-TiO_2, electron injection into the metal is not necessary for high QEs. Instead the results suggest that the role of Pd is purely catalytic. In heterogeneous photocatalysis both photoinduced charge separation and surface catalysis are needed to carry out complete catalytic cycles. Photoinduced charge separation occurs in the semiconductor (TiO_2). However, although broadly assumed, but rarely shown, there is no inherent need for electrons to separate into the metallic NPs for catalysis to occur. An alternative mechanism, where intermediates are photogenerated on the semiconductor surface and then, catalyzed by the metal NPs, form products have been previously proposed,[82] and recently garnered strong experimental evidence.[80] Our results support this interpretation, rather than the paradigm that electron injection into the metal is necessary for photocatalysis to proceed.

Although initial activity was similar irrespective of NP spatial distribution, Pd-TiO_2-C showed markedly lower stability compared to Pd-TiO_2-SA (Figure 5 A). Commonly, particle growth is a major cause for catalyst deactivation.[17,83] To elucidate if growth differed depending on NP spatial distribution, we quantified NP size distributions by TEM image analysis (Experimental Section) before and after catalytic activity (Figure 5 C,F). In contrast to the case of Au-TiO_2 for CO oxidation, with no reaction-induced particle growth (Figure 3 D and Figure S4), significant

NP distribution-dependent growth was observed in Pd-TiO_2 for H_2 generation photocatalysis. In fact, Pd-TiO_2-SA showed negligible, and Pd-TiO_2-C substantial growth (Figure 5 C-H). Because the particle growth was very severe in regions of high NP number-density, it can be concluded that the more severe particle growth in Pd-TiO_2-C compared to Pd-TiO_2-SA was due to the substantially higher fraction of NPs residing in high number-density regions in Pd-TiO_2-C (Figure 2 L). One of two mechanisms, particle migration and coalescence or Ostwald ripening is usually invoked to rationalize particle growth during catalysis. In the first mechanism, individual particles move on the support surface until they meet and coalesce. In the second mechanism, atomic or molecular species eject from smaller particles, migrate on the support surface and incorporate into larger particles.[83] Both mechanisms imply more severe sintering in high NP number density regions.[17] However, further study is needed to elucidate which of these mechanisms cause sintering of Pd NPs in Pd-TiO_2 during photocatalysis.

Using the measured change in NP size (Figure 5 C,F) and simple geometric arguments, the reaction-induced loss of active sites in Pd-TiO_2-C compared to Pd-TiO_2-SA could be estimated (Supporting Section S4). The analysis suggests that after deactivation, Pd-TiO_2-SA had ≈ 31 % more perimeter sites and ≈ 14 % more surface sites than Pd-TiO_2-C. Interestingly, the final difference (≈ 31 %) in perimeter sites between Pd-TiO_2-SA and Pd-TiO_2-C scales closely with the activity difference (≈ 33 %) between the catalysts after deactivation (Figure 5 A). In the absence of other plausible catalyst differences—the NPs were initially identical—our results show that NP distribution-dependent particle growth is the main cause for faster deactivation in Pd-TiO_2-C compared to Pd-TiO_2-SA. The results also give support for a rate-determining step at the Pd NP/TiO_2 perimeter, which was previously proposed by some authors.[82]

CONCLUSIONS

We have shown that NP spatial distributions profoundly influence catalyst performance. Moreover, distributions affect different systems in different ways—activity in Au-TiO_2 for CO oxidation and stability in Pd-TiO_2 for H_2 generation photocatalysis—that may be difficult to predict *a priori*. Consequently, the mode of influence—activity, stability or both—must be evaluated and explained (depletion of reaction intermediates, particle growth, etc.) on a system-by-system basis. Our approach provides means to do this, because NP spatial distribution can be

tuned while keeping weight loading, size distribution and other structural properties constant, and many NPs and supports can be combined, e.g. Pd-Al_2O_3 is demonstrated in Figure S9. We expect knowledge of how NP spatial distribution influences catalyst performance will pave way to more rational catalyst design, since such knowledge can inform when spatial distributions must be controlled for optimal performance. Also important, our method can show when control over NP spatial distribution is not necessary, such that simpler preparation techniques can be used.

The possible impact of controlling NP spatial distribution is enormous. This is because activity in all reactions involving spillover of reaction intermediates could potentially be improved by optimizing NP spatial distribution. Such reactions include, but are not limited to hydrogenation, Fisher Tropsch, ammonia and methanol synthesis and many oxidation reactions.[70–73] Finally, our results show that it is important to control and quantify NP spatial distribution before studying other NP structural effects, because changing NP structural properties frequently changes spatial distributions, which may then convolute effects stemming from the NP structural properties.

EXPERIMENTAL SECTION

Chemicals. Isopropyl alcohol (IPA), ethanol, methanol, hexanes, potassium hydroxide (KOH), conc. hydrochloric acid (HCl), concentrated nitric acid (HNO_3) were purchased from Fisher Scientific. Sodium hexadecane sulfonate (NaHDS)**,** CAS 15015-81-3 was purchased from TCI chemicals. P25 TiO_2 (Aeroxide), $HAuCl_4 \bullet 3H_2O$ (ACS reagent grade), tetralin (1,2,3,4-tetrahydronaphthalene), Palladium (II) acetylacetonate ($Pd(acac)_2$), 0.35 mass fraction Pd, 1-dodecene (DDE, 93-95 %), 1-octadecene (ODE, 90 %) were purchased from Acros Organics. *tert*-butylamine borane (TBAB, 97 %) 1-oleylamine (OLAM, 70 %), oleic acid (OLAC, 90 %), trioctylphosphine (TOP, 97 %) were purchased from Sigma-Aldrich. 1-tetradecene (TDE, 94 %) was purchased from Alfa Aesar. High purity gases (> 99.999 % purity) from Airgas were used for all experiments, giving a water content below 10 ppm. All reagents and solvents were used as received.

Cleaning procedures. A base bath (8 L isopropyl alcohol, 2 L deionized (DI) water and 500 g KOH) was used to clean all glassware. After immersion for at least 1 h in the base bath, the glassware was rinsed copiously in DI water, and then in Milli-Q water. The glassware was then

washed with aqua regia (0.66 : 0.71 volume HCl (conc.) : volume HNO_3 (conc.)) and rinsed copiously with Milli-Q water before drying in a clean oven at 120 ^oC.

Preparation of colloidal Au NPs. Au NPs were synthesized using a modification of previously reported protocols.[84,85] First, 20 mL tetralin and 20 mL OLAM were mixed in a 125 mL 3-neck reaction flask, stirred with a magnetic stir bar and brought to 42 ^oC in an oil-bath. A glass-coated thermocouple inside the 3-neck flask was used to control the temperature *via* feedback control. After the reaction temperature (42 ^oC) was reached, 200 mg of $HAuCl_4 \bullet 3H_2O$ was added. Note: a Teflon-coated spatula should be used for handling the $HAuCl_4 \bullet 3H_2O$. Immediately after $HAuCl_4 \bullet 3H_2O$ dissolved, a reducing solution (88.7 mg of TBAB dissolved in a mixture of 2 mL OLAM and 2 mL tetralin) was quickly injected. The reaction mixture was then stirred for 60 min. To remove reaction by-products and excess OLAM, the reaction mixture was washed by repeated (3 times) precipitation with addition of anti-solvents (IPA and ethanol), collection of NPs by centrifugation (discarding the supernatant) and redispersion of NPs in solvent (hexanes). Concentration of the final dispersion of Au NPs in hexanes (typically 0.05 mg mL^{-1} to 0.25 mg mL^{-1}) was measured by UV-Vis absorption spectroscopy calibrated with ICP-MS.

Preparation of colloidal Pd NPs. Pd NPs were synthesized using a modification of previously reported protocols.[86] First, 305 mg of $Pd(acac)_2$ was added to a 125 mL 3-neck reaction flask, then 19 mL TDE and 21 mL ODE were added followed by 0.82 mL OLAM and 1.58 mL OLAC, and the mixture was stirred with a magnetic stir bar. The flask was then closed with septa, connected to a Schlenk line and degassed under vacuum at room temperature for 50 min. After the initial de-gassing, 1.12 mL TOP (stored and handled in a glovebox) was added to the reaction mixture. The reaction mixture was then brought to 50 ^oC using feedback control from a thermocouple to a heating mantle, and the mixture was degassed for another 60 min. The reaction mixture was then put under N_2 gas and heated to 280 ^oC at a ramp rate of $\approx$ 40 ^oC min^{-1}. After reaching the reaction temperature (+/- 5 ^oC), the mixture was held for 15 min before removing the heating mantle, allowing the reaction mixture to cool down to room temperature. To remove reaction by-products, the reaction mixture was washed by repeated (3 times) precipitation with addition of anti-solvents (IPA, methanol and Milli-Q water), collection of NPs by centrifugation (discarding the supernatant) and redispersion of NPs in solvent (hexanes). Concentration of the final stock

dispersions of Pd NPs in hexanes (typically 0.05 mg mL^{-1} to 0.25 mg mL^{-1}) was measured by UV-Vis calibrated with ICP-MS.

Preparation of supported NPs by conventional impregnation. Conventional impregnation was carried out similarly to previously reported protocols.[41,84,86] In a 500 mL reaction flask, 160 mg of P25 TiO_2 was mixed with 240 mL hexanes, and the dispersion was sonicated for 15 min. An appropriate volume (5 mL to 15 mL) of NP stock solution needed to reach the desired weight loading (0.0035 mass fraction Au for Au-TiO_2 and 0.01 mass fraction Pd for Pd-TiO_2) was then fed into the P25 TiO_2 dispersion (stirred by magnetic stir bar) with a syringe pump at a rate of 0.5 mL min^{-1}. After NP adsorption, catalysts (Au-TiO_2-C or Pd-TiO_2-C) were collected by centrifugation. To mimic the washing of samples produced by surfactant-assisted impregnation (see below), the catalysts were further washed by repeated (2 times) dispersion (with sonication) into 40 mL methanol followed by collection of the catalyst with centrifugation, discarding the supernatant. Finally, the samples were dried under vacuum. In the case of Au-TiO_2-C, ligands on the Au NPs were removed by a previously reported fast annealing protocol.[87] To avoid oxidation of the Pd NPs, in the case of Pd-TiO_2-C, ligands on the Pd NPs were instead removed with dilute acid, similarly to what has been previously reported.[88] The Pd-TiO_2-C catalyst was washed by dispersion of the catalyst in weakly acidified methanol (0.02 mol HCl L^{-1}), followed by collection of the catalyst by centrifugation (discarding the supernatant). The procedure was then repeated in weakly acidified ethanol (0.02 mol HCl L^{-1}) followed by pure ethanol (2 times) to remove acid. The Pd-TiO_2-C catalyst was then dried under vacuum. The methods for removing capping agents have been previously validated.[87,88] However, in the unlikely case that capping agents are still present, they are the same on the pairwise compared catalysts and the catalyst washing and pretreatment procedure is also identical between the samples, so any unlikely influence of the capping agents will be the same for both catalysts. Finally, the surfactant that is added to disperse TiO_2 is highly soluble in methanol, and it is therefore highly unlikely that any remains after extensive washing.

Preparation of supported NPs by surfactant-assisted impregnation. First, a NaHDS stock solution (5 mg mL^{-1}) was prepared by dissolving 50 mg of NaHDS in 10 mL of methanol with sonication. In a 500 mL reaction flask, 160 mg P25 TiO_2 was then mixed with 240 mL hexanes, 0.96 mL of IPA and 2 mL of the NaHDS stock solution, and the dispersion was sonicated for 15

min. An appropriate volume (5 mL to 15 mL) of NP stock solution needed to reach the desired weight loading (0.0035 mass fraction Au for Au-TiO_2 and 0.01 mass fraction Pd for Pd-TiO_2) was then fed into the P25 TiO_2 dispersion (stirred by magnetic stir bar) with a syringe pump at a rate of 0.5 mL min^{-1}. After NP adsorption, catalysts (Au-TiO_2-SA or Pd-TiO_2-SA) were collected by centrifugation. The catalysts were further washed by repeated (2 times) dispersion (with sonication) into 40 mL methanol followed by collection of the catalyst with centrifugation, discarding the supernatant. Finally, the samples were dried under vacuum. In the case of Au-TiO_2-SA, as for Au-TiO_2-C, ligands on the Au NPs were removed by a previously reported fast annealing protocol.[87] Ligands on the Pd-TiO_2-SA catalyst were removed as described above for the Pd-TiO_2-C catalyst.

Characterization Techniques. Transmission electron microscopy (TEM) images were acquired on a FEI Tecnai operating at 200 kV. The powder samples were deposited on lacey C/Cu grids by first gently sonicating in ethanol and then immediately drop-casted onto the grid.

Transient absorption spectroscopy was performed using a chopped 1 kHz 325 nm pump excitation generated from an optical parametric amplifier using 35 fs amplified Ti: sapphire laser (SpectraPhysics). The pump power used for experiments was 200 μJ/cm^2. A 2 kHz probe beam was generated by focusing the 800 nm Ti: sapphire fundamental through a sapphire plate to produce a supercontinuum. Samples were prepared by dispersing dried photocatalyst powder in 1:1 water:ethanol mixtures by sonication and measured in 2 mm cuvettes in transmission geometry. Data was collected and analyzed with Ultrafast Systems software.

UV-Vis spectroscopy for concentration determination of NP stock solutions was carried out on an Agilent Cary 300 UV-Vis system. DLS measurements were carried out on a Brookhaven instrument, Nanobrook Omni. NaHDS stock solution (5 mg mL^{-1}) was prepared by dissolving 50 mg of NaHDS in 10 mL of methanol with sonication. In a 500 mL reaction flask, 160 mg P25 TiO_2 was then mixed with 240 mL hexanes, 0.96 mL of IPA and 2 mL of the NaHDS stock solution, and the dispersion was sonicated for 15 min just before the DLS measurement. Samples were prepared for ICP-MS by digestion in aqua regia and analyzed on a Thermo Scientific XSERIES 2 Quadrupole instrument.

Image analysis for NP size distributions. The freely available, open source image processing tool ImageJ[89] was used for image analysis. Size distributions of colloidal and supported NPs were

estimated from TEM images. To reduce observer bias, the longest dimension across the particles was always measured. At least 100 particles were measured to generate distributions.

Image analysis for NP number-density distributions on supports. ImageJ[89] was used for image analysis. An estimate of the number-density of NPs on a TiO_2 grain was found by dividing the number of NPs observed on the grain with the projected area of the grain. To capture spatial variation of number-density within a grain, each micrograph of a grain was tiled into 16 sub-images before NPs were counted. The workflow was:

1) One micrograph per grain was acquired. (280 nm x 280 nm, 1024 pixels x 1024 pixels for Au-TiO_2-C and Au-TiO_2-SA and 312 nm x 312 nm, 1024 pixels x 1024 pixels for Pd-TiO_2-C and Pd-TiO_2-SA).
2) Each micrograph was split into 16 tiles.
3) The number of NPs were counted in each tile.
4) The projected area of the TiO_2 grain in each tile was measured.
5) The ratio ***number of NPs / projected grain area*** was calculated. This is the NP number-density.
6) Histograms of grain count (or region count) vs NP number-density were created. For each sample, 43 grains were used for generation of histograms.

The workflow described here is exemplified with TEM micrographs in the Supporting Information, Figure S10 and Figure S11. A detailed discussion regarding the image statistics is given in Supporting Section S1.

CO oxidation rate measurements. Catalytic rate measurements were conducted using a plug flow reactor (quartz U-tube, 1 cm inner diameter). The catalyst bed consisted of 10 mg catalyst (Au-TiO_2-SA or Au-TiO_2-C) diluted and thoroughly mixed (using mortar and pestle) with 490 mg silicon carbide (1:49 dilution ratio). To ensure reproducible mass-loading of catalyst, at least 30 mg of catalyst was measured for each experiment and diluted with silicon carbide to a 1:49 ratio. In the quartz U-tube reactor, the reaction bed was sandwiched between two layers of granular acid-washed quartz (900 mg bottom layer, 800 mg top layer). It was checked that the silicon carbide and quartz, in absence of catalyst, was not active for CO oxidation under the reaction conditions

used. The catalyst bed was heated using a Micromeritics Eurotherm 2416 furnace, and the temperature was measured with a thermocouple inserted in the catalyst bed.

Gas flows for CO oxidation rate measurements (transient rates, apparent activation energies and O_2 reaction orders) were prepared by combining 5 % O_2 in Ar (certified standard, Airgas), 5 % CO in Ar (certified standard, Airgas) and Ar (99.999 %, Airgas). The gases were mixed using electronic thermal mass-flow controllers (Brooks SLA5850). In all experiments, the total gas flow was 88 mL min^{-1}, giving a space velocity of 528000 mL h^{-1} g^{-1}_{cat}. The gas composition in the feed and reactor effluent was determined using an online gas chromatograph (Buck Scientific Model 910, Ar carrier gas) with a Hayesep D column, a thermal conductivity detector and a flame ionization detector. The reactor effluent was sampled by the gas chromatograph every 456 s.

Before starting the experiment, it was checked that the reaction lines were gas-tight by flowing pure argon over the catalyst bed to confirm no contaminant gases were observed. Before measuring catalytic rates, the catalysts were pretreated. First, 5 % O_2 in Ar was passed over the catalyst bed while it was heated (25 ^oC min^{-1}) to 330 ^oC (+/- 3 ^oC) and then held for 120 min, then the reaction gas (0.23 $\%_{vol}$ CO, 4.77 $\%_{vol}$ O_2, balance Ar) was passed (88 mL min^{-1}) over the catalyst bed (also at 330 ^oC) for 30 min. The purpose of the pre-treatment is to remove any organic contamination and/or oxide that may have formed on the catalyst surface during storage and handling. The motivation for passing the reaction gas over the catalyst at 330 ^oC during pre-treatment, while data is recorded at 80 ^oC, is to avoid temperature- or reaction-induced structural changes of the catalyst during data collection, which may be difficult to elucidate. After the pre-treatment, Ar was passed over the catalyst bed and it was cooled to reaction temperature (80 ^oC +/- 2 ^oC) while under Ar. Once the reaction temperature was stable at 80 ^oC +/- 2 ^oC, the flow of Ar was replaced by the reaction mixture (0.23 $\%_{vol}$ CO, 4.77 $\%_{vol}$ O_2, balance Ar, 88 mL min^{-1}), and the CO oxidation rate was measured for 20 h. Arrhenius plots for determination of apparent activation energies were the collected.

O_2 reaction orders were measured after measuring the transient CO oxidation rate for 20 h, at which time the CO oxidation rate was stable (Figure 3). The kinetic dependence on O_2 was measured using 5 different O_2 concentrations in the reaction stream (4.77, 3.86, 2.95, 2.05, 1.14)

$\%_{vol}$, with the CO concentration held constant at 0.23 $\%_{vol}$ and with balance of Ar. The gas flow was 88 mL min^{-1} in all measurements.

The above reaction conditions were chosen to ensure differential conditions, i.e. conversion < 20 %,[53] such that rates and rate orders could be accurately extracted. Conversion after rate stabilization was below 5 % for all samples in this study.

Photoreactor. The photoreactor consists of a custom-made quartz beaker in a gas-tight stainless-steel encasing with quartz windows both at the top and bottom of the reactor (Figure S5). The photoreactor is connected to argon gas lines and inserted in a custom-made stage in a solar simulator while the reactor effluent is continuously measured by a Buck Scientific Model 910 gas chromatograph (Figure S6). When the light is turned on, the entire surface area (19 cm^2) of the liquid sample in the quartz beaker is illuminated with collimated light with a wavelength of 337 nm. Collimated white light is generated by a 150 W xenon lamp in an Oriel® Sol1A™ solar simulator (model 94201A). A band pass filter (337 nm, 10 nm FWHM, Edmund Optics, 50 mm diameter) was used to pass only light with a wavelength of 337 nm. A UV-VIS spectrum of the bandpass filter is presented in Figure S12. The intensity of light exiting the photoreactor was measured with a thermopile light sensor (Newport, model 919P-003-10) connected to a power meter (Newport, 843-R). Because the catalyst suspension absorbs 100% of light (optical Density > 10 by UV-Vis absorption spectroscopy with 0.35 mg mL^{-1} catalyst in 25 mL 1:1 water:ethanol), the intensity of light absorbed by catalyst was determined by measuring the light exiting the photoreactor when 25 mL of pure 1:1 water:ethanol was in the photoreactor. The intensity of light absorbed by the catalyst was thus determined to be 7.9 W m^{-2}. Note that part of this light may have been scattered rather than absorbed by the catalyst, but such scattering leads to an underestimation of the true QE, such that the reported QE represents a lower bound. Also note that because both Pd-TiO_2-C and Pd-TiO_2-SA are made from the same batch of P25 TiO_2, the scattering component in both catalyst suspensions should be identical. Measurements of the intensity of light exiting the reactor when filled with 25 mL 1:1 water:ethanol gave identical results before and after the photocatalytic reaction, ensuring stable operation of the lamp during the photocatalytic measurement.

Photocatalysis measurements. The catalyst (Pd-TiO_2-C or Pd-TiO_2-SA) was dispersed by sonication (15 min) in 1:1 water:ethanol at a concentration of 0.35 mg mL^{-1}. At this catalyst

concentration the reaction rate does not change significantly with concentration (Figure S13), a condition which is desirable for QE measurements according to IUPAC guidelines.[90] The photoreactor was then filled with 25 mL of this suspension, a stir bar was added, and the suspension was stirred vigorously. The photoreactor was then connected to the argon line (Figure S6) and the headspace of the reactor was purged (in the dark) with argon (40 mL min^{-1}) until no O_2/N_2 peak could be observed in the reactor effluent. After the photoreactor was fully purged of O_2/N_2, the light was turned on and the suspension was irradiated for 20 h, during which time the effluent gas (40 mL min^{-1}) was analyzed by the gas chromatograph (Buck Scientific Model 910, Ar carrier gas) every 24.5 min.

Quantum efficiency calculation. The photon flux absorbed by the catalyst is calculated from the intensity absorbed by the catalyst (7.9 W m^{-2}, see above) and the irradiated area (19 cm^2) of the photocatalytic suspension. Given that the incident light has a wavelength of 337 nm, the photon flux then becomes:

$$Photon\ Flux = 7.9\left(\frac{J}{s*m^2}\right)*0.0019(m^2)*\frac{337*10^{-9}}{h*c}\left(\frac{m}{J*s*\frac{m}{s}}\right) = 2.55*10^{16}\ \frac{photons}{s}$$

Where h is Planck's constant and c is the speed of light.

The quantum efficiency is then calculated by the following formula:[78,90,91]

$$QE\ (\%) = \frac{2*H_2\ production\ rate}{Photon\ Flux}*100$$

Microkinetic modelling. The microkinetic model was constructed and solved using python and the numpy package. It simulates the spatial and temporal variations in the O_{act} and O_{ad} coverage over a rectangular TiO_2 (101) surface lattice that is periodic in the y-direction and with Au at the two boundaries in the x-direction. The distance between the Au particles was varied (0.5 nm to 20 nm) to simulate different Au distributions in the real catalysts. The kinetics of CO oxidation, TiO_2 re-oxidation and surface oxygen (O_{act} and O_{ad}) diffusion was accounted for as specified in Supporting Section S3.

Complementary DFT calculations were conducted to study the $\square_{O_{act}}$ formation energy as a function of i) distance from the Au particles, and ii) O_{act} coverage at the Au-TiO_2 perimeter. All

calculations where performed at the at the PBE-D3(BJ)[92–94] level of theory using the parameters in reference[68] with the VASP package[95–98] on a periodic (4×5) model of the TiO_2 (101) surface including a 2 nm thick and tall Au-nanorod. See Supporting Section S3 for further details.

ACKNOWLEDGEMENTS

This work is supported by a TomKat seed grant from Stanford University. M.C. acknowledges further support from the School of Engineering at Stanford University and from a Terman Faculty Fellowship. Part of this work was performed at the Stanford Nano Shared Facilities (SNSF, Stanford University), supported by the National Science Foundation under award ECCS-1542152 and at the Center for Nanoscale Materials, a U.S. Department of Energy Office of Science User Facility, and supported by the U.S. Department of Energy, Office of Science, under Contract No. DE-AC02-06CH11357. The Swedish National Infrastructure for Computing (SNIC) is acknowledged for providing computational resources at the National Supercomputer Centre (NSC)

AUTHOR INFORMATION

Corresponding Authors

*E-mail: mcargnello@stanford.edu

*E-mail: alexander.holm@fysik.su.se

ORCID

Alexander Holm: 0000-0002-3660-4389

Matteo Cargnello: 0000-0002-7344-9031

Notes

The authors declare no competing financial interest.

Disclaimer: Certain commercial equipment, instruments, or materials are identified in this paper in order to specify the experimental procedure adequately. Such identification is not intended to imply recommendation or endorsement by the National Institute of Standards and Technology, nor is it intended to imply that the materials or equipment identified are necessarily the best available for the purpose.

ASSOCIATED CONTENT

Supporting Information

Supporting discussion and Supporting figures

REFERENCES

(1) Hvolbaek, B.; Janssens, T. V. W.; Clausen, B. S.; Falsig, H.; Christensen, C. H.; Norskov, J. K. Catalytic Activity of Au Nanoparticles. Nano Today 2007, 2 (4), 14–18.

(2) Corma, A.; Garcia, H. Supported Gold Nanoparticles as Catalysts for Organic Reactions. Chem. Soc. Rev. 2008, 37 (9), 2096–2126.

(3) Munnik, P.; de Jongh, P. E.; de Jong, K. P. Recent Developments in the Synthesis of Supported Catalysts. Chem. Rev. 2015, 115 (14), 6687–6718.

(4) Losch, P.; Huang, W.; Goodman, E. D.; Wrasman, C. J.; Holm, A.; Riscoe, A. R.; Schwalbe, J. A.; Cargnello, M. Colloidal Nanocrystals for Heterogeneous Catalysis. Nano Today 2019, 24, 15–47.

(5) Nie, Z.; Petukhova, A.; Kumacheva, E. Properties and Emerging Applications of Self-Assembled Structures Made from Inorganic Nanoparticles. Nat. Nanotechnol. 2010, 5 (1), 15–25.

(6) Elghanian, R.; Storhoff, J. J.; Mucic, R. C.; Letsinger, R. L.; Mirkin, C. A. Selective Colorimetric Detection of Polynucleotides Based on the Distance-Dependent Optical Properties of Gold Nanoparticles. Science 1997, 277 (5329), 1078–1081.

(7) Graham, D.; Thompson, D. G.; Smith, W. E.; Faulds, K. Control of Enhanced Raman Scattering Using a DNA-Based Assembly Process of Dye-Coded Nanoparticles. Nat. Nanotechnol. 2008, 3 (9), 548–551.

(8) Puntes, V. F.; Gorostiza, P.; Aruguete, D. M.; Bastus, N. G.; Alivisatos, A. P. Collective Behaviour in Two-Dimensional Cobalt Nanoparticle Assemblies Observed by Magnetic Force Microscopy. Nat. Mater. 2004, 3 (4), 263–268.

(9) Maillard, D.; Kumar, S. K.; Fragneaud, B.; Kysar, J. W.; Rungta, A.; Benicewicz, B. C.; Deng, H.; Brinson, L. C.; Douglas, J. F. Mechanical Properties of Thin Glassy Polymer Films Filled with Spherical Polymer-Grafted Nanoparticles. Nano Lett. 2012, 12 (8), 3909–3914.

(10) Lee, J.; Govorov, A. O.; Kotov, N. A. Bioconjugated Superstructures of CdTe Nanowires and Nanoparticles: Multistep Cascade Förster Resonance Energy Transfer and Energy Channeling. Nano Lett. 2005, 5 (10), 2063–2069.

(11) Cargnello, M.; Delgado Jaén, J. J.; Hernández Garrido, J. C.; Bakhmutsky, K.; Montini, T.; Calvino Gámez, J. J.; Gorte, R. J.; Fornasiero, P. Exceptional Activity for Methane Combustion over Modular Pd@CeO_2 Subunits on Functionalized Al_2O_3. Science 2012, 337 (6095), 713–717.

(12) Torres Galvis, H. M.; Bitter, J. H.; Khare, C. B.; Ruitenbeek, M.; Dugulan, A. I.; de Jong, K. P. Supported Iron Nanoparticles as Catalysts for Sustainable Production of Lower Olefins. Science 2012, 335 (6070), 835–838.

(13) Turner, M.; Golovko, V. B.; Vaughan, O. P. H.; Abdulkin, P.; Berenguer-Murcia, A.; Tikhov, M. S.; Johnson, B. F. G.; Lambert, R. M. Selective Oxidation with Dioxygen by

Gold Nanoparticle Catalysts Derived from 55-Atom Clusters. Nature 2008, 454 (7207), 981–983.

(14) Bell, A. T. The Impact of Nanoscience on Heterogeneous Catalysis. Science 2003, 299 (5613), 1688–1691.

(15) Nørskov, J. K.; Bligaard, T.; Hvolbæk, B.; Abild-Pedersen, F.; Chorkendorff, I.; Christensen, C. H. The Nature of the Active Site in Heterogeneous Metal Catalysis. Chem. Soc. Rev. 2008, 37 (10), 2163–2171.

(16) Karim, W.; Spreafico, C.; Kleibert, A.; Gobrecht, J.; Vandevondele, J.; Ekinci, Y.; Van Bokhoven, J. A. Catalyst Support Effects on Hydrogen Spillover. Nature 2017, 541 (7635), 68–71.

(17) Prieto, G.; Zečević, J.; Friedrich, H.; de Jong, K. P.; de Jongh, P. E. Towards Stable Catalysts by Controlling Collective Properties of Supported Metal Nanoparticles. Nat. Mater. 2013, 12 (1), 34–39.

(18) Ono, L. K.; Roldán-Cuenya, B. Effect of Interparticle Interaction on the Low Temperature Oxidation of CO over Size-Selected Au Nanocatalysts Supported on Ultrathin TiC Films. Catal. Lett. 2007, 113 (3–4), 86–94.

(19) Kielbassa, S.; Häbich, A.; Schnaidt, J.; Bansmann, J.; Weigl, F.; Boyen, H. G.; Ziemann, P.; Behm, R. J. On the Morphology and Stability of Au Nanoparticles on TiO_2(110) Prepared from Micelle-Stabilized Precursors. Langmuir 2006, 22 (18), 7873–7880.

(20) Goodman, E. D.; Johnston-Peck, A. C.; Dietze, E. M.; Wrasman, C. J.; Hoffman, A. S.; Abild-Pedersen, F.; Bare, S. R.; Plessow, P. N.; Cargnello, M. Catalyst Deactivation via Decomposition into Single Atoms and the Role of Metal Loading. Nat. Catal. 2019, 2 (9), 748–755.

(21) Eggenhuisen, T. M.; Friedrich, H.; Nudelman, F.; Zečević, J.; Sommerdijk, N. A. J. M.; de Jongh, P. E.; de Jong, K. P. Controlling the Distribution of Supported Nanoparticles by Aqueous Synthesis. Chem. Mater. 2013, 25 (6), 890–896.

(22) van der Meer, J.; Bardez, I.; Bart, F.; Albouy, P. A.; Wallez, G.; Davidson, A. Dispersion of Co_3O_4 Nanoparticles within SBA-15 Using Alkane Solvents. Microporous Mesoporous Mater. 2009, 118 (1–3), 183–188.

(23) Prieto, G.; Meeldijk, J. D.; de Jong, K. P.; de Jongh, P. E. Interplay between Pore Size and Nanoparticle Spatial Distribution: Consequences for the Stability of $CuZn/SiO_2$ Methanol Synthesis Catalysts. J. Catal. 2013, 303, 31–40.

(24) van den Berg, R.; Prieto, G.; Korpershoek, G.; van der Wal, L. I.; van Bunningen, A. J.; Lægsgaard-Jørgensen, S.; de Jongh, P. E.; de Jong, K. P. Structure Sensitivity of Cu and CuZn Catalysts Relevant to Industrial Methanol Synthesis. Nat. Commun. 2016, 7, 13057.

(25) Lopez, N.; Janssens, T. V. W.; Clausen, B. S.; Xu, Y.; Mavrikakis, M.; Bligaard, T.; Nørskov, J. K. On the Origin of the Catalytic Activity of Gold Nanoparticles for Low-Temperature CO Oxidation. J. Catal. 2004, 223 (1), 232–235.

(26) den Breejen, J. P.; Radstake, P. B.; Bezemer, G. L.; Bitter, J. H.; Frøseth, V.; Holmen, A.; De Jong, K. P. On the Origin of the Cobalt Particle Size Effects in Fischer-Tropsch Catalysis. J. Am. Chem. Soc. 2009, 131 (20), 7197–7203.

(27) Ben-Shahar, Y.; Scotognella, F.; Kriegel, I.; Moretti, L.; Cerullo, G.; Rabani, E.; Banin, U. Optimal Metal Domain Size for Photocatalysis with Hybrid Semiconductor-Metal Nanorods. Nat. Commun. 2016, 7, 10413.

(28) Campbell, C. T.; Parker, S. C.; Starr, D. E. The Effect of Size-Dependent Nanoparticle Energetics on Catalyst Sintering. Science 2002, 298 (5594), 811–814.

(29) Wettergren, K.; Schweinberger, F. F.; Deiana, D.; Ridge, C. J.; Crampton, A. S.; Rotzer, M. D.; Hansen, T. W.; Zhdanov, V. P.; Heiz, U.; Langhammer, C. High Sintering Resistance of Size-Selected Platinum Cluster Catalysts by Suppressed Ostwald Ripening. Nano Lett. 2014, 14 (10), 5803–5809.

(30) Zhang, S.; Cargnello, M.; Cai, W.; Murray, C. B.; Graham, G. W.; Pan, X. Revealing Particle Growth Mechanisms by Combining High-Surface-Area Catalysts Made with Monodisperse Particles and Electron Microscopy Conducted at Atmospheric Pressure. J. Catal. 2016, 337, 240–247.

(31) Lee, S.-Y.; Aris, R. The Distribution of Active Ingredients in Supported Catalysts Prepared by Impregnation. Catal. Rev. - Sci. Eng. 1985, 27 (2), 207–340.

(32) Torres Galvis, H. M.; Koeken, A. C. J.; Bitter, J. H.; Davidian, T.; Ruitenbeek, M.; Dugulan, I. A.; de Jong, K. P. Effect of Precursor on the Catalytic Performance of Supported Iron Catalysts for the Fischer – Tropsch Synthesis of Lower Olefins. Catal. Today 2013, 215, 95–102.

(33) Munnik, P.; de Jongh, P. E.; de Jong, K. P. Control and Impact of the Nanoscale Distribution of Supported Cobalt Particles Used in Fischer − Tropsch Catalysis. J. Am. Chem. Soc. 2014, 136 (20), 7333–7340.

(34) Qiu, S.; Zhang, X.; Liu, Q.; Wang, T.; Zhang, Q.; Ma, L. A Simple Method to Prepare Highly Active and Dispersed Ni/MCM-41 Catalysts by Co-Impregnation. Catal. Commun. 2013, 42, 73–78.

(35) Jiao, L.; Regalbuto, J. R. The Synthesis of Highly Dispersed Noble and Base Metals on Silica via Strong Electrostatic Adsorption : I . Amorphous Silica. J. Catal. 2008, 260 (2), 329–341.

(36) Saib, A. M.; Moodley, D. J.; Ciobîca, I. M.; Hauman, M. M.; Sigwebela, B. H.; Weststrate, C. J.; Niemantsverdriet, J. W.; van de Loosdrecht, J. Fundamental Understanding of Deactivation and Regeneration of Cobalt Fischer-Tropsch Synthesis Catalysts. Catal. Today 2010, 154 (3–4), 271–282.

(37) Arslan, I.; Walmsley, J. C.; Rytter, E.; Bergene, E.; Midgley, P. A. Toward Three-Dimensional Nanoengineering of Heterogeneous Catalysts. J. Am. Chem. Soc. 2008, 130 (17), 5716–5719.

(38) Cornu, C.; Bonardet, J. L.; Casale, S.; Davidson, A.; Abramson, S.; André, G.; Porcher, F.; Grčić, I.; Tomasic, V.; Vujevic, D.; Koprivanac, N. Identification and Location of Iron Species in Fe/SBA-15 Catalysts: Interest for Catalytic Fenton Reactions. J. Phys. Chem. C 2012, 116 (5), 3437–3448.

(39) Ward, E. P. W.; Yates, T. J. V.; Fernández, J. J.; Vaughan, D. E. W.; Midgley, P. A. Three-Dimensional Nanoparticle Distribution and Local Curvature of Heterogeneous Catalysts Revealed by Electron Tomography. J. Phys. Chem. C 2007, 111 (31), 11501–11505.

(40) Marceau, E.; Che, M.; Čejka, J.; Zukal, A. Nickel(II) Nitrate vs. Acetate: Influence of the Precursor on the Structure and Reducibility of Ni/MCM-41 and Ni/Al-MCM-41 Catalysts. ChemCatChem 2010, 2 (4), 413–422.

(41) Cargnello, M.; Doan-Nguyen, V. V. T.; Gordon, T. R.; Diaz, R. E.; Stach, E. A.; Gorte, R. J.; Fornasiero, P.; Murray, C. B. Control of Metal Nanocrystal Size Reveals Metal-Support Interface Role for Ceria Catalysts. Science 2013, 341 (6147), 771–773..

(42) Gross, A. F.; Diehl, M. R.; Beverly, K. C.; Richman, E. K.; Tolbert, S. H. Controlling Magnetic Coupling between Cobalt Nanoparticles through Nanoscale Confinement in Hexagonal Mesoporous Silica. J. Phys. Chem. B 2003, 107 (23), 5475–5482.

(43) Hondow, N.; Fuller, R. O. The Use of Preformed Nanoparticles in the Production of Heterogeneous Catalysts. J. Colloid Interface Sci. 2014, 417, 396–401.

(44) Somorjai, G. A.; Park, J. Y. Colloid Science of Metal Nanoparticle Catalysts in 2D and 3D Structures. Challenges of Nucleation, Growth, Composition, Particle Shape, Size Control and Their Influence on Activity and Selectivity. Top. Catal. 2008, 49 (3–4), 126–135.

(45) Cargnello, M. Colloidal Nanocrystals as Building Blocks for Well-Defined Heterogeneous Catalysts. Chem. Mater. 2019, 31 (3), 576–596.

(46) Rao, S. R. Surface Chemistry of Froth Flotation, 2nd ed.; Springer Science: New York, 2004; Vol. 1.

(47) Bezemer, G. L.; Radstake, P. B.; Koot, V.; van Dillen, A. J.; Geus, J. W.; de Jong, K. P. Preparation of Fischer-Tropsch Cobalt Catalysts Supported on Carbon Nanofibers and Silica Using Homogeneous Deposition-Precipitation. J. Catal. 2006, 237 (2), 291–302.

(48) Feng, H.; Elam, J. W.; Libera, J. A.; Setthapun, W.; Stair, P. C. Palladium Catalysts Synthesized by Atomic Layer Deposition for Methanol Decomposition. Chem. Mater. 2010, 22 (10), 3133–3142.

(49) Grami, A. Probability , Random Variables , Statistics , and Random Processes; JohnWiley & Sons, Inc.: Hoboken, NJ, USA, 2020.

(50) Widmann, D.; Behm, R. J. Activation of Molecular Oxygen and the Nature of the Active Oxygen Species for Co Oxidation on Oxide Supported Au Catalysts. Acc. Chem. Res. 2014, 47 (3), 740–749.

(51) Saavedra, J.; Doan, H. A.; Pursell, C. J.; Grabow, L. C.; Chandler, B. D. The Critical Role of Water at the Gold-Titania Interface in Catalytic CO Oxidation. Science 2014, 345 (6204), 1599–1602.

(52) Aguilar-Guerrero, V.; Gates, B. C. Kinetics of CO Oxidation Catalyzed by Supported Gold: A Tabular Summary of the Literature. Catal. Lett. 2009, 130 (1–2), 108–120.

(53) Schubert, M. M.; Hackenberg, S.; van Veen, A. C.; Muhler, M.; Plzak, V.; Behm, R. J. CO Oxidation over Supported Gold Catalysts -"Inert" and “Active” Support Materials and Their Role for the Oxygen Supply during Reaction. J. Catal. 2001, 197 (1), 113–122.

(54) Overbury, S. H.; Schwartz, V.; Mullim, D. R.; Yan, W.; Dai, S. Evaluation of the Au Size Effect: CO Oxidation Catalyzed by Au/TiO_2. J. Catal. 2006, 241 (1), 56–65.

(55) Denkwitz, Y.; Schumacher, B.; Kučerová, G.; Behm, R. J. Activity, Stability, and Deactivation Behavior of Supported Au/TiO_2 Catalysts in the CO Oxidation and Preferential CO Oxidation Reaction at Elevated Temperatures. J. Catal. 2009, 267 (1), 78–88.

(56) Denkwitz, Y.; Zhao, Z.; Hörmann, U.; Kaiser, U.; Plzak, V.; Behm, R. J. Stability and Deactivation of Unconditioned Au/TiO_2 Catalysts during CO Oxidation in a near-Stoichiometric and O_2-Rich Reaction Atmosphere. J. Catal. 2007, 251 (2), 363–373.

(57) Kotobuki, M.; Leppelt, R.; Hansgen, D. A.; Widmann, D.; Behm, R. J. Reactive Oxygen on a Au/TiO_2 Supported Catalyst. J. Catal. 2009, 264 (1), 67–76.

(58) Calla, J. T.; Bore, M. T.; Datye, A. K.; Davis, R. J. Effect of Alumina and Titania on the Oxidation of CO over Au Nanoparticles Evaluated by 13C Isotopic Transient Analysis. J. Catal. 2006, 238 (2), 458–467.

(59) Choudhary, T. V.; Sivadinarayana, C.; Chusuei, C. C.; Datye, A. K.; Fackler, J. P.; Goodman, D. W. CO Oxidation on Supported Nano-Au Catalysts Synthesized from a $[Au_6(PPh_3)_6](BF_4)_2$ Complex. J. Catal. 2002, 207 (2), 247–255.

(60) Ojeda, M.; Zhan, B. Z.; Iglesia, E. Mechanistic Interpretation of CO Oxidation Turnover Rates on Supported Au Clusters. J. Catal. 2012, 285 (1), 92–102.

(61) Zanella, R.; Giorgio, S.; Shin, C. H.; Henry, C. R.; Louis, C. Characterization and Reactivity in CO Oxidation of Gold Nanoparticles Supported on TiO_2 Prepared by Deposition-Precipitation with NaOH and Urea. J. Catal. 2004, 222 (2), 357–367.

(62) Widmann, D.; Behm, R. J. Active Oxygen on a Au/TiO_2 Catalyst: Formation, Stability, and CO Oxidation Activity. Angew. Chemie - Int. Ed. 2011, 50 (43), 10241–10245.

(63) Maeda, Y.; Iizuka, Y.; Kohyama, M. Generation of Oxygen Vacancies at a Au/TiO_2 Perimeter Interface during Co Oxidation Detected by in Situ Electrical Conductance Measurement. J. Am. Chem. Soc. 2013, 135 (2), 906–909.

(64) Widmann, D.; Behm, R. J. Dynamic Surface Composition in a Mars-van Krevelen Type Reaction: CO Oxidation on Au/TiO_2. J. Catal. 2018, 357, 263–273.

(65) Li, L.; Zeng, X. C. Direct Simulation Evidence of Generation of Oxygen Vacancies at the Golden Cage Au16 and TiO_2 (110) Interface for Co Oxidation. J. Am. Chem. Soc. 2014, 136 (45), 15857–15860.

(66) Duan, Z.; Henkelman, G. CO Oxidation at the Au/TiO_2 Boundary: The Role of the Au/Ti5c Site. ACS Catal. 2015, 5 (3), 1589–1595.

(67) Widmann, D.; Krautsieder, A.; Walter, P.; Brückner, A.; Behm, R. J. How Temperature Affects the Mechanism of CO Oxidation on Au/TiO_2 : A Combined EPR and TAP Reactor Study of the Reactive Removal of TiO_2 Surface Lattice Oxygen in Au/TiO_2 by CO. ACS Catal. 2016, 6 (8), 5005–5011.

(68) Schlexer, P.; Widmann, D.; Behm, R. J.; Pacchioni, G. CO Oxidation on a Au/TiO_2 Nanoparticle Catalyst via the Au-Assisted Mars-van Krevelen Mechanism. ACS Catal. 2018, 8 (7), 6513–6525.

(69) Wang, Y. G.; Cantu, D. C.; Lee, M. S.; Li, J.; Glezakou, V. A.; Rousseau, R. CO Oxidation on Au/TiO_2: Condition-Dependent Active Sites and Mechanistic Pathways. J. Am. Chem. Soc. 2016, 138 (33), 10467–10476.

(70) Conner, W. C.; Falconer, J. L. Spillover in Heterogeneous Catalysis. Chem. Rev. 1995, 95 (3), 759–788.

(71) van der Laan, G. P.; Beenackers, A. A. C. M. Kinetics and Selectivity of the Fischer-Tropsch Synthesis: A Literature Review. Catal. Rev. - Sci. Eng. 1999, 41 (3–4), 255–318.

(72) Kitano, M.; Kanbara, S.; Inoue, Y.; Kuganathan, N.; Sushko, P. V.; Yokoyama, T.; Hara, M.; Hosono, H. Electride Support Boosts Nitrogen Dissociation over Ruthenium Catalyst and Shifts the Bottleneck in Ammonia Synthesis. Nat. Commun. 2015, 6, 6731.

(73) Prins, R. Hydrogen Spillover. Facts and Fiction. Chem. Rev. 2012, 112 (5), 2714–2738.

(74) Su, R.; Dimitratos, N.; Liu, J.; Carter, E.; Althahban, S.; Wang, X.; Shen, Y.; Wendt, S.; Wen, X.; Niemantsverdriet, J. W.; Iversen, B. B.; Kiely, C. J.; Hutchings, G. J.; Besenbacher, F. Mechanistic Insight into the Interaction between a Titanium Dioxide Photocatalyst and Pd Cocatalyst for Improved Photocatalytic Performance. ACS Catal. 2016, 6 (7), 4239–4247.

(75) Su, R.; Tiruvalam, R.; Logsdail, A. J.; He, Q.; Downing, C. A.; Jensen, M. T.; Dimitratos, N.; Kesavan, L.; Wells, P. P.; Bechstein, R.; Jensen, H. H.; Wendt, S.; Catlow, C. R. A.; Kiely, C. J.; Hutchings, G. J.; Besenbacher, F. Designer Titania-Supported Au-Pd Nanoparticles for Efficient Photocatalytic Hydrogen Production. ACS Nano 2014, 8 (4), 3490–3497.

(76) Sasikala, R.; Sudarsan, V.; Sudakar, C.; Naik, R.; Sakuntala, T.; Bharadwaj, S. R. Enhanced Photocatalytic Hydrogen Evolution over Nanometer Sized Sn and Eu Doped Titanium Oxide. Int. J. Hydrogen Energy 2008, 33 (19), 4966–4973.

(77) Nakibli, Y.; Kalisman, P.; Amirav, L. Less Is More: The Case of Metal Cocatalysts. J. Phys. Chem. Lett. 2015, 6 (12), 2265–2268.

(78) Kudo, A.; Miseki, Y. Heterogeneous Photocatalyst Materials for Water Splitting. Chem. Soc. Rev. 2009, 38 (1), 253–278.

(79) Katsiev, K.; Harrison, G.; Al-Salik, Y.; Thornton, G.; Idriss, H. Gold Cluster Coverage Effect on H_2 Production over Rutile TiO_2(110). ACS Catal. 2019, 9 (9), 8294–8305.

(80) Joo, J. B.; Dillon, R.; Lee, I.; Yin, Y.; Bardeen, C. J.; Zaera, F. Promotion of Atomic Hydrogen Recombination as an Alternative to Electron Trapping for the Role of Metals in the Photocatalytic Production of H_2. Proc. Natl. Acad. Sci. U. S. A. 2014, 111 (22), 7942–7947.

(81) Yoshihara, T.; Katoh, R.; Furube, A.; Tamaki, Y.; Murai, M.; Hara, K.; Murata, S.; Arakawa, H.; Tachiya, M. Identification of Reactive Species in Photoexcited Nanocrystalline TiO_2 Films by Wide-Wavelength-Range (400-2500 Nm) Transient Absorption Spectroscopy. J. Phys. Chem. B 2004, 108 (12), 3817–3823.

(82) Bowker, M.; James, D.; Stone, P.; Bennett, R.; Perkins, N.; Millard, L.; Greaves, J.; Dickinson, A. Catalysis at the Metal-Support Interface: Exemplified by the Photocatalytic Reforming of Methanol on Pd/TiO_2. J. Catal. 2003, 217 (2), 427–433.

(83) Bartholomew, C. H. Mechanisms of Catalyst Deactivation. Appl. Catal. A Gen. 2001, 212 (1–2), 17–60.

(84) Wrasman, C. J.; Boubnov, A.; Riscoe, A. R.; Hoffman, A. S.; Bare, S. R.; Cargnello, M. Synthesis of Colloidal Pd/Au Dilute Alloy Nanocrystals and Their Potential for Selective Catalytic Oxidations. J. Am. Chem. Soc. 2018, 140 (40), 12930–12939.

(85) Peng, S.; Lee, Y.; Wang, C.; Yin, H.; Dai, S.; Sun, S. A Facile Synthesis of Monodisperse Au Nanoparticles and Their Catalysis of CO Oxidation. Nano Res. 2008, 1 (3), 229–234.

(86) Willis, J. J.; Gallo, A.; Sokaras, D.; Aljama, H.; Nowak, S. H.; Goodman, E. D.; Wu, L.; Tassone, C. J.; Jaramillo, T. F.; Abild-Pedersen, F.; Cargnello, M. Systematic Structure-Property Relationship Studies in Palladium-Catalyzed Methane Complete Combustion. ACS Catal. 2017, 7 (11), 7810–7821.

(87) Cargnello, M.; Chen, C.; Diroll, B. T.; Doan-Nguyen, V. V. T.; Gorte, R. J.; Murray, C. B. Efficient Removal of Organic Ligands from Supported Nanocrystals by Fast Thermal Annealing Enables Catalytic Studies on Well-Defined Active Phases. J. Am. Chem. Soc. 2015, 137 (21), 6906–6911.

(88) Mazumder, V.; Sun, S. Oleylamine-Mediated Synthesis of Pd Nanoparticles for Catalytic Formic Acid Oxidation. J. Am. Chem. Soc. 2009, 131 (13), 4588–4589.

(89) Schneider, C. A.; Rasband, W. S.; Eliceiri, K. W. NIH Image to ImageJ: 25 Years of Image Analysis. Nat. Methods 2012, 9 (7), 671–675.

(90) Braslavsky, S. E.; Braun, A. M.; Cassano, A. E.; Emeline, A. V.; Litter, M. I.; Palmisano, L.; Parmon, V. N.; Serpone, N. Glossary of Terms Used in Photocatalysis and Radiation Catalysis (IUPAC Recommendations 2011). Pure Appl. Chem. 2011, 83 (4), 931–1014.

(91) Pinaud, B. A.; Benck, J. D.; Seitz, L. C.; Forman, A. J.; Chen, Z.; Deutsch, T. G.; James, B. D.; Baum, K. N.; Baum, G. N.; Ardo, S.; Wang, H.; Miller, E.; Jaramillo, T. F. Technical and Economic Feasibility of Centralized Facilities for Solar Hydrogen Production via Photocatalysis and Photoelectrochemistry. Energy Environ. Sci. 2013, 6 (7), 1983–2002.

(92) Perdew, J. P.; Burke, K.; Ernzerhof, M. Generalized Gradient Approximation Made Simple. Phys. Rev. Lett. 1996, 77 (18), 3865–3868.

(93) Grimme, S.; Antony, J.; Ehrlich, S.; Krieg, H. A Consistent and Accurate Ab Initio Parametrization of Density Functional Dispersion Correction (DFT-D) for the 94 Elements H-Pu. J. Chem. Phys. 2010, 132 (15), 154104.

(94) Grimme, S.; Ehrlich, S.; Goerigk, L. Effect of the Damping Function in Dispersion Corrected Density Functional Theory. J. Comput. Chem. 2011, 32 (7), 1456–1465.

(95) Kresse, G.; Hafner, J. Ab Initio Molecular Dynamics for Liquid Metals. Phys. Rev. B 1993, 47 (1), 558–561.

(96) Kresse, G.; Hafner, J. Ab Initio Molecular-Dynamics Simulation of the Liquid-Metal Amorphous- Semiconductor Transition in Germanium. Phys. Rev. B 1994, 49 (20), 14251–14269.

(97) Kresse, G.; Furthmüller, J. Efficiency of Ab-Initio Total Energy Calculations for Metals and Semiconductors Using a Plane-Wave Basis Set. Comput. Mater. Sci. 1996, 6 (1), 15–50.

(98) Kresse, G.; Furthmüller, J. Efficient Iterative Schemes for Ab Initio Total-Energy Calculations Using a Plane-Wave Basis Set. Phys. Rev. B 1996, 54 (16), 11169–11186.

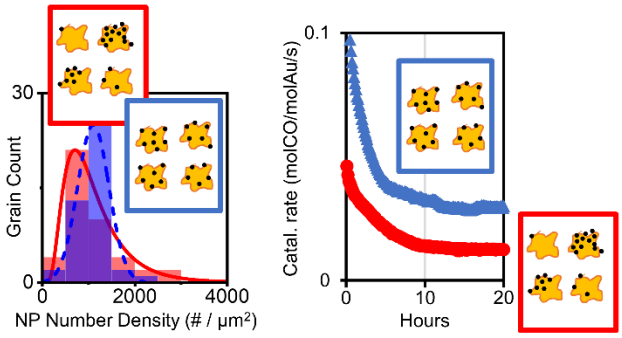

Table of contents graphic (TOC)

Supporting Information for

Nanoscale Spatial Distribution of Supported Nanoparticles Controls Activity and Stability in Powder Catalysts

Alexander Holm,[†, ‡, *] Emmett D. Goodman,[†] Joakim Halldin Stenlid,[‡] Aisulu Aitbekova,[†] Rosadriana Zelaya,[†] Benjamin T. Diroll,[§] Aaron C. Johnston-Peck,[∥] Kun-Che Kao,[†] Curtis W. Frank,[#] Lars G. M. Pettersson,[‡] Matteo Cargnello[†, *]

[†] Department of Chemical Engineering and SUNCAT Center for Interface Science and Catalysis, Stanford University, Stanford, CA 94305, USA

[‡] Department of Physics, AlbaNova University Center, Stockholm University, SE-106 91 Stockholm, Sweden

[§] Center for Nanoscale Materials, Argonne National Laboratory, 9700 S. Cass Avenue, Lemont, Illinois 60439, USA

[#] Department of Chemical Engineering, Stanford University, Stanford, CA 94305, USA

[∥] Material Measurement Laboratory, National Institute of Standards and Technology, Gaithersburg, MD, 20899, USA

Corresponding Authors

*E-mail: mcargnello@stanford.edu

*E-mail: alexander.holm@fysik.su.se

Supporting Discussion

Section S1 – Image Statistics

The purpose of the TEM image statistics is to obtain a measure of the spatial distribution of nanoparticles (NPs) dispersed on TiO_2 (P25, Aeroxide, Acros Organics). Image statistics to obtain NP number-density distributions of points in space have previously been developed in fields as diverse as astrophysics and fluid dynamics. In astrophysics, image statistics of number-density has been used to describe the spatial distribution of stars in galaxies,[1] and in fluid dynamics it has been used to describe the spatial distribution of particles under stationary flow.[2] Number-density distribution determinations from image statistics have in common that an area (or volume) element (bin) must be chosen with a bin size which must compromise between two requirements (ref[1], p. 875):

(1) Keep the Poisson noise in each bin low. Poisson noise will be significant if the bin is too small.

(2) Avoid overbinning, i.e. too large bin size with related information loss in high-density regions.

Ideal bin size which satisfies both requirements must be found by manual trial and error in the image analysis.[1] We have addressed the problem of using an appropriate bin size by acquiring one image for each grain with large field of view, then sub-dividing this image into, respectively, one, four or sixteen sub-regions. The NP number-density distribution was then estimated using bin sizes representing whole grains (bin sizes in the range 0.01 μm^2 to 0.07 μm^2 defined by the projected grain-area inside one image, illustrated in Figure S10 by the region denoted "1 tile") or using smaller regions within each grain (bin sizes in the range 0.0035 μm^2 to 0.02 μm^2 defined by the projected grain-area inside $1/4^{th}$ of the image, illustrated by the region denoted "4 tiles" in Figure S10) or even smaller regions within each grain (bin sizes in the range 0.0035 μm^2 to 0.006 μm^2 defined by the projected grain area inside $1/16^{th}$ of the image, illustrated by the region denoted "16 tiles" in Figure S10).

For a random distribution of particles in a 2-dimensional region, the number of particles in each bin is Poisson distributed:[2]

$$P(k) = \frac{\lambda^k e^{-\lambda}}{k!} \qquad \text{(eqn. S1)}$$

where λ is the average number of particles in each bin and *P(k)* is the probability that a given bin will have *k* particles.[2] When the average number of particles in each bin is sufficiently large (λ > 10) the Poisson distribution is well approximated by the normal distribution (because of the central value theorem).[3] Thus, when a bin is sufficiently large such that it contains more than 10 particles on average, the Poisson noise is low.[1,3] The average NP number-density was 1100 NPs μm^{-2} and 1123 NPs μm^{-2} for Au-TiO_2-C and Au-TiO_2-SA, respectively (Table S1). Thus, we chose 0.01 μm^2 as the lower limit for bin size, as this limits the Poisson noise. In addition, with this and larger bin sizes, a perfectly random distribution of particles is expected to result in a normal distribution of NP number-density (again, because the Poisson distribution is well approximated with a normal distribution for λ > 10). Note that the average NP number-densities for Pd-TiO_2-C and Pd-TiO_2-SA are higher (Table S1) at 1962 NPs μm^{-2} and 2142 μm^{-2}, respectively, meaning that choosing 0.01 μm^2 as the lower limit for bin size will result in minimized Poisson noise and expected normal distributions for randomly distributed NPs also for these samples.

For the smaller subsections in Figure S10 (denoted ”4 tiles” and “16 tiles”), a smallest bin size of 0.01 μm^2 was not possible, since there were not sufficient tiles of this size and larger. We thus conclude that to obtain reliable NP number-density distributions free of Poisson noise, but still avoiding substantial information loss in high NP number-density regions, an appropriate bin size for our samples could be defined by the projected area of entire TiO_2 grains in the full images (Figure S10). The distributions generated by considering entire grains are presented in Figure 2.

To allow fitting probability density functions to the NP number-density distributions, the small number of bins with apparent zero NP number-density (no NPs observed) must be assigned a small NP number-density, and a good estimation is ½ of the detection limit.[4] This approach produces reliable estimates of the true distributions, given that the number of values below the detection limit is small,[4] as in our case (e.g., the distributions generated from considering entire grains had no bins with apparent zero density). Our method has a detection limit given by an NP count of 1, in a bin of size 0.01 μm^2 (1 tile) or 0.0035 μm^2 (4 tiles and 16 tiles), giving detection limits of 100 or 286 NPs μm^{-2}, such that an apparent NP number-density of zero is estimated as 50 or 143 NPs μm^{-2} when fitting probability density functions to the data.

The NP number-density in each bin (projected grain-area in image tile) was determined by simply counting the particles observed in the bin, then measuring the projected grain-area of the bin and forming the ratio:

$$\rho_{\#} = \frac{Number\ of\ NPs}{Projected\ grain\ area\ (\mu m^2)} \qquad \text{(eqn. S2)}$$

The determination of NP number-density in one bin (region) is exemplified in Figure S11. Note that this ratio is an estimate of the true NP number-density, since the true NP number-density depends on the actual surface area of the grain, which depends on the thickness of the grain and the size and shape of the primary TiO_2 particles. However, the projected grain area scales directly onto the true grain area and since the same P25 TiO_2 stock sample is used for production of all catalysts, the NP number-densities in projected areas map onto real number-densities in the same fashion for all samples. Therefore, the NP number-density as defined here, allows comparison of NP spatial distribution between samples. However, we wish to emphasize that because the NP number densities measured are not the true number densities, but merely scale with the real NP number densities, it is the comparison of number densities between samples, and the type of number density distribution (e.g. normal or log-normal) that is of significance, not the actual values for number density that are measured. In addition, the scaling between projected support area in plane-view TEM images and real support area is expected to be very different for different supports (e.g. between porous supports and non-porous supports). Therefore, for appropriate comparison of NP spatial distribution between samples, it is imperative that the same support is used for all samples that are to be compared.

To summarize, the workflow for determining NP number-density distributions was as follows:

1) One micrograph per grain was acquired. (280 nm x 280 nm, 1024 pixels x 1024 pixels for Au-TiO_2-C and Au-TiO_2-SA and 312 nm x 312 nm, 1024 pixels x 1024 pixels for Pd-TiO_2-C and Pd-TiO_2-SA).
2) Each micrograph was split into 16 tiles (Figure S10).
3) The number of NPs were counted in each tile (Figure S11).
4) The projected area of the TiO_2 grain in each tile was measured (Figure S11).

5) The ratio ***number of NPs / projected grain area*** was calculated. This is the NP number-density (Figure S11).

6) Histograms (probability density functions, PDFs) of grain count (or region count) vs NP number-density were created. For each sample, 43 grains (43 full micrographs) were used for generation of histograms.

The probability density function of regions vs NP number-density ($PDF_{regions}$) is generated by measuring $\rho_{\#}$ on entire grains or sections of grains, according to the tiling in Figure S10. The probability density function (PDF_{NPs}) and cumulative distribution function (CDF_{NPs}) of NPs vs NP number-density is then given by:

$$PDF_{NPs}(i) = \frac{w_i \rho_{\#,i}}{\sum_i w_i \rho_i} \quad \text{(eqn. S3)}$$

$$CDF_{NPs}(i) = \frac{1}{\sum_i w_i \rho_{\#,i}} \sum_0^i w_j \rho_{\#,j} \quad \text{(eqn. S4)}$$

Where w_i is the $PDF_{regions}$ (whole grains or subsections of grains) at NP number-density $\rho_{\#,i}$. $PDF_{regions}$ generated by measuring $\rho_{\#}$ on whole grains is presented in the main text (Figure 2 E,K). CDF_{NPs} measured on whole grains is presented in the main text, Figure 2 F,L. Distributions were fitted to data using OriginPro. The Kolmogorov-Smirnov test, Kolmogorov-Smirnov (modified) test and the Anderson-Darling test were applied to judge the goodness of fit. Reports of all distribution fits are presented in Figure S14 – S25.

Section S2 – Statistical significance of difference between CO oxidation apparent activation energies between Au-TiO_2-SA and Au-TiO_2-C.

Given that:

$\overline{E_{a,SA}}$: Estimator for CO oxidation apparent activation energy on Au-TiO_2-SA (29.7 kJ mol^{-1}, see Figure 3 C)

$\overline{E_{a,C}}$: Estimator of CO oxidation apparent activation energy on Au-TiO_2-C (37.1 kJ mol^{-1}, see Figure 3 C)

$S_{Ea,SA}$: Estimator of standard deviation for the experimental determination of $E_{a,SA}$ (1.5 kJ mol^{-1})

$S_{Ea,C}$: Estimator of standard deviation for the experimental determination of $E_{a,C}$ (0.9 kJ mol^{-1})

n : Number of data points (4) used in the linear regression determination of $E_{a,SA}$ and $E_{a,C}$, respectively.

a null hypothesis (H_0) can be formed:

H_0: $E_{a,SA} = E_{a,C}$

Assuming the variances for the experimental determination of $E_{a,SA}$ and $E_{a,C}$ are the same, we have the pooled estimator for standard deviation, S_p:[5]

$$S_p = \sqrt{\frac{(n-1)S_{Ea,C}^2 + (n-1)S_{Ea,SA}^2}{2n-2}} = \sqrt{\frac{(4-1)0.9^2 + (4-1)1.5^2}{2*4-2}} = 1.23693$$

with the degrees of freedom (d.f.) for the pooled standard deviation being:[5]

$$d.f. = 2n - 2 = 2 * 4 - 2 = 6$$

and the t statistic:[5]

$$t = \frac{\overline{E_{a,C}} - \overline{E_{a,SA}}}{S_p\sqrt{\frac{2}{n}}} = \frac{37.1 - 29.7}{1.23693\sqrt{\frac{2}{4}}} = 8.46$$

Which, for *d.f.* = 6 degrees of freedom gives a p-value of 0.00007. Thus the null hypothesis $\mathbf{H_0}$ can be rejected at the 99.993 % level of significance, very strongly indicating that $E_{a,C} > E_{a,SA}$.

Section S3 – Computational details: CO oxidation by the Au-assisted Mars van-Krevelen mechanism

The spatially and temporally resolved microkinetic model was generated by considering previously proposed[6] elementary reactions (R1 – R7, Table S2) for CO oxidation by the Au-assisted Mars van-Krevelen mechanism, with the modification that—to spatially resolve the model—we distinguished reaction sites at the Au-TiO_2 perimeter (#) from reaction sites on the TiO_2 surface (*). Added to the model is, furthermore, elementary surface diffusion steps (R8-R11, Table S2). Kinetic parameters were taken from the literature for the anatase TiO_2(101) surface. This is a reasonable model system as anatase is present in the larger amount (~ 0.81 : 0.15 : 0.04 anatase : rutile : amorphous material)[7] in the P25 TiO_2 used in experiments, and (101) is one of the most prevalent low-index surface facets for anatase.[8,9]

The O_{ad} (surface-adsorbed O atoms) and O_{act} (surface-lattice oxygen) coverages (in %) were treated as variables on a 2D x×y surface lattice mesh discretized by $d_x = d_y = 0.1$ nm. The NP separation, x, was varied from 0.5 to 20 nm while y was kept constant at 1 nm. The reaction rate constants were obtained by transition state theory, i.e.

$$k = \frac{k_b T}{h} e^{-\frac{\Delta G^{\ddagger}}{k_b T}} \qquad \text{(eqn. S5)}$$

Where h and k_b are the Planck and Boltzmann constant, respectively, and T is the temperature (set to 353 K, as in the experiments). $\Delta G^{\ddagger} = \Delta H^{\ddagger} - T\Delta S^{\ddagger}$ is the reaction barrier.

Adsorption concentrations of the species X = {O_2*, CO*} were inferred from the gas phase partial pressures, p_X, and adsorption free energies ($\Delta G_{ads,X} = \Delta H_{ads,X} - T\Delta S_{ads,X}$) using Langmuir isotherms (equations S6 and S7).

$$\Theta_X = \frac{K_{ads,X} p_X}{1+K_{ads,X} p_X} \quad \text{(eqn. S6)}$$

with

$$K_{ads,X} = -k_b T \cdot ln\left(\Delta G_{ads,X}\right) \quad \text{(eqn. S7)}$$

where the total pressure is 1 bar, and the partial pressures of O_2 (g) and CO (g) are 0.0477 bar and 0.0023 bar, respectively. For the modelling we further used a CO_2 (g) partial pressure of 3 % of the p_{CO}, which is an average of the measured steady-state CO_2 partial pressures in the various experiments.

Two-dimensional diffusion constants, *D*, were determined using a similar expression as for the kinetic rate constants:

$$D = \frac{a^2}{z}\frac{k_b T}{h} e^{\frac{-\Delta G^{\ddagger}}{k_b T}} \quad \text{(eqn. S8)}$$

Where *a* is the separation distance between two equivalent oxygen sites. On the anatase (101) facet, this distance is 3.8 Å to 5.1 Å depending on the lattice direction. The 5.1 Å value is used in the model. For a 2D model, *z* is 4. $\Delta G^{\ddagger}$ is the diffusion free energy barrier.

To obtain the spatial and temporal variation of the O_{act} and O_{ad}, we solved the reaction-diffusion model until steady-state conditions were achieved (defined as a $\Delta\Theta_{Oact} < 0.001$ % per μs). The reaction-diffusion model reads:

$$\frac{\partial \mathbf{u}}{\partial t} = \boldsymbol{D} \, \Delta \, \mathbf{u} + \mathrm{f}(\mathbf{u}) \quad \text{(eqn. S9)}$$

Where **u** is the concentration vector of O_{act} and O_{ad}, ***D*** the diagonal matrix containing their surface diffusion constants, and f(**u**) describes the consumption and creation of the surface species from chemical reactions R4-R7, Table S2 (specified below by rate equations S12 - S13 and S15 - 16). This model was solved by using the central approximation and the finite-difference method for the spatial differentials (eqn. S10), and forward difference (eqn. S11) for the time with a logarithmic, progressive time-step, *h*, of < 1.5 μs.

$$\Delta \, \mathbf{u}(x,y) \approx \frac{\mathbf{u}(x+d_{x/y},y)+\mathbf{u}(x-d_{x/y},y)+\mathbf{u}(x,y+d_{x/y})+\mathbf{u}(x,y-d_{x/y})-4\mathbf{u}(x,y)}{d_{x/y}^2} \quad \text{(eqn. S10)}$$

$$\frac{\partial \mathbf{u}}{\partial t}(t;x,y) \approx \frac{\mathbf{u}(t+dt;x,y)-\mathbf{u}(t;x,y)}{h} \quad \text{(eqn. S11)}$$

An initial condition of a uniform O_{act} coverage of 0.9 was used for quicker convergence to steady-state coverages. An initial coverage of 0.1 was used for O_{ad}. The boundary conditions in the y-direction were periodic, while the reaction boundary conditions in the x-direction (from the Au-TiO_2 perimeter rate equations R2, R3, R6 and R7 in Table S2) were (using standard surface chemistry reaction expressions):[10]

$$\frac{\partial \Theta_{act}}{\partial t} = -k_{CO2}\frac{K_{ad,CO}p_{CO}}{1+K_{ad,CO}p_{CO}}\frac{\Theta_{Oact}}{(1-\Theta_{Oact})} + k_{-CO2}\frac{K_{ad,CO2}p_{CO2}}{1+K_{ad,CO2}p_{CO2}}\frac{(1-\Theta_{Oact})}{\Theta_{Oact}} \quad \text{(eqn. S12)}$$

$$\frac{\partial \Theta_{ad}}{\partial t} = -k_{CO2}\frac{K_{ad,CO}p_{CO}}{1+K_{ad,CO}p_{CO}}\frac{\Theta_{Oad}}{(1-\Theta_{Oad})} + k_{-CO2}\frac{K_{ad,CO2}p_{CO2}}{1+K_{ad,CO2}p_{CO2}}\frac{(1-\Theta_{Oad})}{\Theta_{Oad}} \quad \text{(eqn. S13)}$$

The boundary condition for the surface diffusion in the x-direction was (R8 and R11 in Table S2):

$$\frac{\partial \mathbf{u}}{\partial x} = 0 \quad \text{(eqn. S14)}$$

where k_{CO2} and k_{-CO2} are the forward and backward reaction rate constants for the CO_2 production whereas K_{CO} and K_{CO2} are the CO and CO_2 adsorption equilibrium constants. The above boundary conditions (eqn. S12 – S14) were added to the reaction expressions used for the reoxidation of the TiO_2 surface (eqn. S15 – S16), with the modification that the reoxidation kinetics is slower at the perimeter due to stabilization effect on oxygen vacancies in the proximity of the Au NP[11] (as described below). As previously implemented,[12] a linear interpolation is used to modify the reaction barriers of reactions R6 and R7, Table S2, from oxidizing ($\Theta_{Oact} = 1$) to reducing ($\Theta_{Oact} = 0$) conditions, using the extreme values of the barrier listed in Table S2. The barrier for diffusion of O_{act} to the Au-TiO_2 perimeter from the TiO_2 surface (R9) was shifted by 1.5 eV (see below) compared to the diffusion barrier on the TiO_2 surface (R8) to account for the larger stability[11] of $\square_{O_{act}}$ (1.5 eV, see below) at the Au-TiO_2 perimeter compared to on the TiO_2 surface. The reoxidation (R1, R4 and R5 in Table S2) on the surface was modelled through the following rate equations (using standard surface chemistry reaction expressions):[10]

$$\frac{\partial \Theta_{Oact}}{\partial t} = k_{Ox,Oact} \frac{K_{ad,O2} p_{O2}}{1+K_{ad,O2} p_{O2}} \frac{(1-\Theta_{Oact})}{\Theta_{Oact}} + k_{Ox,Oad} \frac{\Theta_{Oad}}{(1-\Theta_{Oad})} \frac{(1-\Theta_{Oact})}{\Theta_{Oact}} \qquad \text{(eqn. S15)}$$

$$\frac{\partial \Theta_{Oad}}{\partial t} = k_{Ox,Oact} \frac{K_{ad,O2} p_{O2}}{1+K_{ad,O2} p_{O2}} \frac{(1-\Theta_{Oact})}{\Theta_{Oact}} - k_{Ox,Oad} \frac{\Theta_{Oad}}{(1-\Theta_{Oad})} \frac{(1-\Theta_{Oact})}{\Theta_{Oact}} \qquad \text{(eqn. S16)}$$

Here, $k_{\mathrm{Ox,Oact}}$ and $k_{\mathrm{Ox,Oad}}$ are the reaction constants for the forward reoxidation reactions (R4, R5, Table S2) of O_{act} and O_{ad} respectively, whereas $K_{\mathrm{ad,O2}}$ is the adsorption constant for O_2 (g). The rate equations for all elementary steps are listed in Table S3. The barriers for the reverse reoxidation reactions, leading to O_2 (g), are very high compared to the forward reactions (Table S2)[12] and these backward reactions have therefore been omitted in our model. Also note that as the rate-determining reaction steps are expected to be the explicit surface reactions (Table S2) leading to the formation and consumption of O_{ad} and O_{act},[11,12] only these species are modelled explicitly. This means that the system of differential equations simplifies to include the rates of Θ_{Oad} and Θ_{Oact}. All other species have a constant, homogeneous, concentration in our model. From a macroscopic perspective this is a good approximation. On the atomic level, it is possible that additional understanding could be obtained from a more detailed kinetic Monte Carlo simulation that accounts for the variations of all species in time and space. This is, however, beyond the scope of the current study.

It should, furthermore, be pointed out that for the anatase (101) surface there is strong support in the literature that oxygen vacancies tend to migrate into the subsurface.[13,14] However, since the subsurface vacancies heal through the surface, and since diffusion can take place within the subsurface,[14,15] our model is appropriate both for the case when oxygen vacancies exist only at the surface and when they exist both at the surface and subsurface.

As mentioned above, it is known from theoretical studies that vacancy formation is more beneficial at the Au-TiO_2 perimeter than at the TiO_2 surface.[12] We studied this effect by using identical DFT parameters as in Schlexer et al.[11] (except that the D3(BJ) dispersion correction model[16,17] was used here), and a 4×5 surface slab model with Au nanorods on TiO_2 (101) containing 5 unique O lattice sites at various distances from the Au rod. We arrive at the same

conclusion as Schlexer et al.,[11] i.e. that the surface-lattice oxygen vacancy ($\square_{O_{act}}$) formation is more beneficial (1.5 to 1.9 eV) at the site immediately next to the Au rod (Table S5) than at the TiO_2 surface . However, we also find that this effect quickly vanishes, and already at the next site the vacancy formation energy is the same as on the pure TiO_2 (101) surface. In addition, our results show that the formation energy of $\square_{O_{act}}$ is dependent on the O_{act} coverage at the perimeter, with lower coverage leading to a decrease in vacancy stabilization (Table S6). In our model, two different perimeter O_{act} sites exists. One is more hidden under the Au-rod (position 6 in Figure S27), whereas one is more exposed (position 1 in Figure S27). We use the relative (vs the TiO_2 (101) surface) stabilization of $\square_{O_{act}}$ of the more exposed site (position 1) in our microkinetic model as this oxygen is more readily available for CO abstraction without reorganization of the Au-nanostructure.

Different values for the activation energy of the reoxidation of the surface oxygen vacancies ($\square_{O_{act}}$) exist in the literature[11,12,15] (Table S2, rxn R4), and we tested this range of values in our model. The results (Figure S26 and Table S4) are qualitatively the same irrespective of the reoxidation barrier used. And for presentation in the paper (Figure 4), we therefore used an intermediate value (0.8 eV) for this barrier. In all cases, the majority (>>99 %) of the CO_2 is generated from the reaction of O_{act} rather than O_{ad} at steady-state. The concentration of O_{ad} is low (<<0.01 coverage) and homogeneous on the surfaces, except at the Au/TiO_2 perimeter where its concentration is further reduced.

Section S4 – Difference in number of surface sites and perimeter sites between Pd-TiO_2-C and Pd-TiO_2-SA after photocatalytic deactivation

Volume of NPs conserved:

$$N_{SA}V_{SA} = N_C V_C \quad \text{(eqn. S17)}$$

$$N_{SA}d_{SA}^3 = N_C d_C^3 \quad \text{(eqn. S18)}$$

$$\frac{N_{SA}}{N_C} = \left(\frac{d_C}{d_{SA}}\right)^3 \quad \text{(eqn. S19)}$$

Fraction of Pd-TiO_2-SA perimeter sites to Pd-TiO_2-C perimeter sites after deactivation (average particle diameters taken from Figure 5 in the main text):

$$\frac{N_{SA}d_{SA}}{N_C d_C} = \left(\frac{d_C}{d_{SA}}\right)^3 \left(\frac{d_{SA}}{d_C}\right) = \left(\frac{d_C}{d_{SA}}\right)^2 = \left(\frac{4.8\ nm}{4.2\ nm}\right)^2 = 1.31 \rightarrow 131\ \%$$

Fraction of Pd-TiO_2-SA surface sites to Pd-TiO_2-C surface sites after deactivation (particle diameters taken from Figure 5 in the main text):

$$\frac{N_{SA}d_{SA}^2}{N_C d_C^2} = \left(\frac{d_C}{d_{SA}}\right)^3 \left(\frac{d_{SA}}{d_C}\right)^2 = \frac{d_C}{d_{SA}} = \frac{4.8\ nm}{4.2\ nm} = 1.14 \rightarrow 114\ \%$$

Where

N_{SA}: Number of Pd NPs in the surfactant-assisted sample, Pd-TiO_2-SA.

N_C: Number of Pd NPs in the conventional sample, Pd-TiO_2-C.

d_{SA}: Average diameter (size) of Pd NPs in Pd-TiO_2-SA, post catalysis (From Figure 5 C).

d_C: Average diameter (size) of Pd NPs in Pd-TiO_2-C, post catalysis (From Figure 5 F).

Disclaimer: Certain commercial equipment, instruments, or materials are identified in this paper in order to specify the experimental procedure adequately. Such identification is not intended to imply recommendation or endorsement by the National Institute of Standards and Technology, nor is it intended to imply that the materials or equipment identified are necessarily the best available for the purpose.

Sample	Metal wt % by ICP-MS	$\langle\rho_{\#}\rangle$ (number of NPs / μm^2)	μ (Lognormal distribution)	σ (Lognormal distribution)	μ (Normal distribution)	σ (Normal distribution)
Au-TiO_2-SA	0.36	1100	-	-	1100	341
Au-TiO_2-C	0.35	1123	6.868	0.557	-	-
Pd-TiO_2-SA	0.90	2142	-	-	2142	658
Pd-TiO_2-C	0.98	1962	6.793	1.256	-	-

Table S1. ICP-MS data for the weight loading of Au in Au-TiO_2-SA and Au-TiO_2-C and of Pd in Pd-TiO_2-SA and Pd-TiO_2-C. Statistical parameters describing the normal, $\rho_{\#} \sim N(\mu, \sigma^2)$ distributions of Au-TiO_2-SA and Pd-TiO_2-SA and lognormal, $ln(\rho_{\#}) \sim N(\mu, \sigma^2)$, distributions of Au-$TiO_2$-C and Pd-$TiO_2$-C, which were presented in Figure 2 (E,K). The average NP number-densities were calculated according to equations 4 and 5 in the main text.

	Reaction	E_a	E_{-a}	References	
R1*	$O_2(g) + * \rightarrow O_2^*$	0	0.57	[18,19] The entropic part was obtained from vibrational calculations using DFT calculation with the Gaussian 16 software at the PBE/6-311G(2d,2p)+D3 level of theory at the experimental temperature and pressure	Adsorption / desorption steps
R1#	$O_2(g) + \# \rightarrow O_2^\#$	0	0.57	[18,19] Same parameters as R1*	
R2	$CO(g) + \# \rightarrow CO^\#$	0	0.81	[11,20]	
R3	$CO_2^\# \rightarrow CO_2(g) + \#$	0.8		[11]	
R4*	$\square_{O_{act}}{}^* + O_2{}^* \rightarrow O_{act}{}^* + O_{ad}{}^*$	0.44-1.04	2.43	[11,12,15] The barrier was varied between 0.44 eV and 1.04 eV to test the different values reported in the literature (See Figure S26).	Surface reaction steps
R4#	$\square_{O_{act}}{}^\# + O_2{}^\# \rightarrow O_{act}{}^\# + O_{ad}{}^\#$	1.94-2.54		Barriers shifted by 1.5 eV (Section S3 and Table S5) compared to barriers for reaction R4* to account for the larger stability[11] of $\square_{O_{act}}$ at the Au-TiO_2 perimeter compared to on the TiO_2 surface.	
R5*	$\square_{O_{act}}{}^* + O_{ad}{}^* \rightarrow O_{act}{}^*$	0.25	2.43	[11,12]	
R5#	$\square_{O_{act}}{}^\# + O_{ad}{}^\# \rightarrow O_{act}{}^\#$	1.75		Barrier shifted by 1.5 eV (Section S3 and Table S5) compared to barriers for reaction R5* to account for the larger stability[11] of $\square_{O_{act}}$ at the Au-TiO_2 perimeter compared to on the TiO_2 surface.	
R6	$O_{act}{}^\# + CO^\# \rightarrow CO_2{}^\# + \square_{O_{act}}{}^\#$	0.85 to 2.51	0.68 to 1.05	[12] Barriers linearly interpolated from oxidizing to reducing conditions.	

R7	$O_{ad}^{\#} + CO^{\#} \rightarrow CO_2^{\#} + \#$	0.85 to 2.51	0.68 to 1.05	[12] Barriers linearly interpolated from oxidizing to reducing conditions.	
R8	$\square_{O_{act}}^{*} + O_{act}^{*} \rightarrow O_{act}^{*} + \square_{O_{act}}^{*}$	0.82	0.82	[14,21]	Surface Diffusion steps
R9	$\square_{O_{act}}^{\#} + O_{act}^{*} \rightarrow O_{act}^{\#} + \square_{O_{act}}^{*}$	1.5 to 0.82	0.82	[14,21] Diffusion barriers shifted to 1.5 eV at $\Theta_{Oact} = 1$ to account for the larger stability of $\square_{O_{act}}$ (1.5 eV) at the Au-TiO_2 perimeter compared to on the TiO_2 surface (see Table S5 and ref [11]). At $\Theta_{Oact} = 0$ the barrier from R8 was used, with a linear interpolation in-between the extremes.	
R10	$* + O_{ad}^{*} \rightarrow O_{ad}^{*} + *$			Assumed not to move	
R11	$\# + O_{ad}^{*} \rightarrow O_{ad}^{\#} + *$			Assumed not to move	

Table S2. Energetics in eV of the elementary steps considered for the spatially and temporally resolved modelling of CO oxidation on Au-TiO_2 via the Au-assisted Mars van Krevelen mechanism. Where applicable, activation energies in the literature were converted to Gibbs activation free energies (barriers) using a prefactor $\nu = \frac{k_b T}{h} e^{\frac{\Delta S^{\ddagger}}{k_b}} = 1e13$. R1-R7 were previously proposed as elementary steps. R4#, R5# and R8-R11 were added in this work to spatially resolve these previously proposed elementary steps. In the above, E_a and E_{-a} are the activation Gibbs free energies at 353 K and the experimental partial pressures (p_{O2} = *0.0477 bar,* p_{CO} = *0.0023 bar,* p_{CO2} = *6.9 * 10^{-5} bar).*

	Elementary step	Equation for rate calculation
R1*	$O_2(g) + * \rightarrow O_2^*$	Instantaneous and modelled by adsorption isotherms (see Section S3).
R1#	$O_2(g) + \# \rightarrow O_2^\#$	Instantaneous and modelled by adsorption isotherms (see Section S3).
R2	$CO(g) + \# \rightarrow CO^\#$	Instantaneous and modelled by adsorption isotherms (see Section S3).
R3	$CO_2^\# \rightarrow CO_2(g) + \#$	Instantaneous and modelled by adsorption isotherms (see Section S3). The barrier of 0.8 eV is lower than the barrier for R6-R7 why the desorption of CO_2 is rapid compared to its generation
R4*	$\square_{O_{act}}{}^* + O_2{}^* \rightarrow O_{act}{}^* + O_{ad}{}^*$	$r_{4*} = k^*_{Ox,Oact} \frac{K_{ad,O2}p_{O2}}{1+K_{ad,O2}p_{O2}} \frac{(1-\Theta_{Oact})}{\Theta_{Oact}}$
R4#	$\square_{O_{act}}{}^\# + O_2{}^\# \rightarrow O_{act}{}^\# + O_{ad}{}^\#$	$r_{4\#} = k^\#_{Ox,Oact} \frac{K_{ad,O2}p_{O2}}{1+K_{ad,O2}p_{O2}} \frac{(1-\Theta_{Oact})}{\Theta_{Oact}}$
R5*	$\square_{O_{act}}{}^* + O_{ad}{}^* \rightarrow O_{act}{}^*$	$r_{5*} = k^*_{Ox,Oad} \frac{\Theta_{Oad}}{(1-\Theta_{Oad})} \frac{(1-\Theta_{Oact})}{\Theta_{Oact}}$
R5#	$\square_{O_{act}}{}^\# + O_{ad}{}^\# \rightarrow O_{act}{}^\#$	$r_{5\#} = k^\#_{Ox,Oad} \frac{\Theta_{Oad}}{(1-\Theta_{Oad})} \frac{(1-\Theta_{Oact})}{\Theta_{Oact}}$
R6	$O_{act}{}^\# + CO^\# \rightleftharpoons CO_2{}^\# + \square_{O_{act}}{}^\#$	$r_6 = k_{CO2} \frac{K_{ad,CO}p_{CO}}{1+K_{ad,CO}p_{CO}} \frac{\Theta_{Oact}}{(1-\Theta_{Oact})} - k_{-CO2} \frac{K_{ad,CO2}p_{CO2}}{1+K_{ad,CO2}p_{CO2}} \frac{(1-\Theta_{Oact})}{\Theta_{Oact}}$
R7	$O_{ad}{}^\# + CO^\# \rightleftharpoons CO_2{}^\# + \#$	$r_7 = k_{CO2} \frac{K_{ad,CO}p_{CO}}{1+K_{ad,CO}p_{CO}} \frac{\Theta_{Oad}}{(1-\Theta_{Oad})} + k_{-CO2} \frac{K_{ad,CO2}p_{CO2}}{1+K_{ad,CO2}p_{CO2}} \frac{(1-\Theta_{Oad})}{\Theta_{Oad}}$
R8	$\square_{O_{act}}{}^* + O_{act}{}^* \rightarrow O_{act}{}^* + \square_{O_{act}}{}^*$	Modelled as a diffusion process (see Section S3).
R9	$\square_{O_{act}}{}^\# + O_{act}{}^* \rightarrow O_{act}{}^\# + \square_{O_{act}}{}^*$	Modelled as a diffusion process (see Section S3).
R10	$* + O_{ad}{}^* \rightarrow O_{ad}{}^* + *$	Modelled as a diffusion process (see Section S3).
R11	$\# + O_{ad}{}^* \rightarrow O_{ad}{}^\# + *$	Modelled as a diffusion process (see Section S3).

Table S3. Rate equations for the elementary steps in the CO oxidation on Au-TiO_2 via the Au-assisted Mars van Krevelen mechanism.

↓ E_a / Δd →	**0.5 nm**	**1 nm**	**2 nm**	**5 nm**	**10 nm**	**20 nm**
0.4 eV	4.23	4.23	4.23	4.23	4.23	4.23
0.6 eV	3.06	3.06	3.06	3.06	3.06	3.06
0.8 eV	3.34E-01	6.32E-01	1.27	1.51	1.52	1.52
1.0 eV	4.41E-02	5.63E-02	9.01E-02	2.71E-01	4.69E-01	4.76E-01

Table S4. CO_2 production rates in 10^{-5} nmol m^{-1} s^{-1} for the simulated combinations of reoxidation barrier, E_a, and NP separation, Δd.

Position	**Site information**	**$\Delta\Delta E^{vac}$**
1	Perimeter	-1.49
2	Lattice	0.00
3	Lattice	0.00
4	Lattice	-0.01
5	Lattice	-0.02
6	Perimeter	-1.89

Table S5. O_{act} vacancy formation energies, $\Delta\Delta E^{vac}$, relative a pristine TiO_2 (101) surface in eV for different positions on the Au-TiO_2 (101) surface estimated by DFT calculations at the PBE-D3 level of theory. Positions depicted in Figure S27.

Coverage	**$\Delta\Delta E^{vac}$ (pos 1)**	**$\Delta\Delta E^{vac}$ (pos 6)**
0.25	0.00	0.00
0.50	0.35	-0.03
0.75	0.26	0.09
1.00	0.61	0.42

Table S6. O_{act} vacancy formation energies, $\Delta\Delta E^{vac}$, at the Au-TiO_2(101) perimeter (position 1 and 6 in Figure S27) as a function of O_{act} vacancy coverage. Energies are relative 25% coverage.

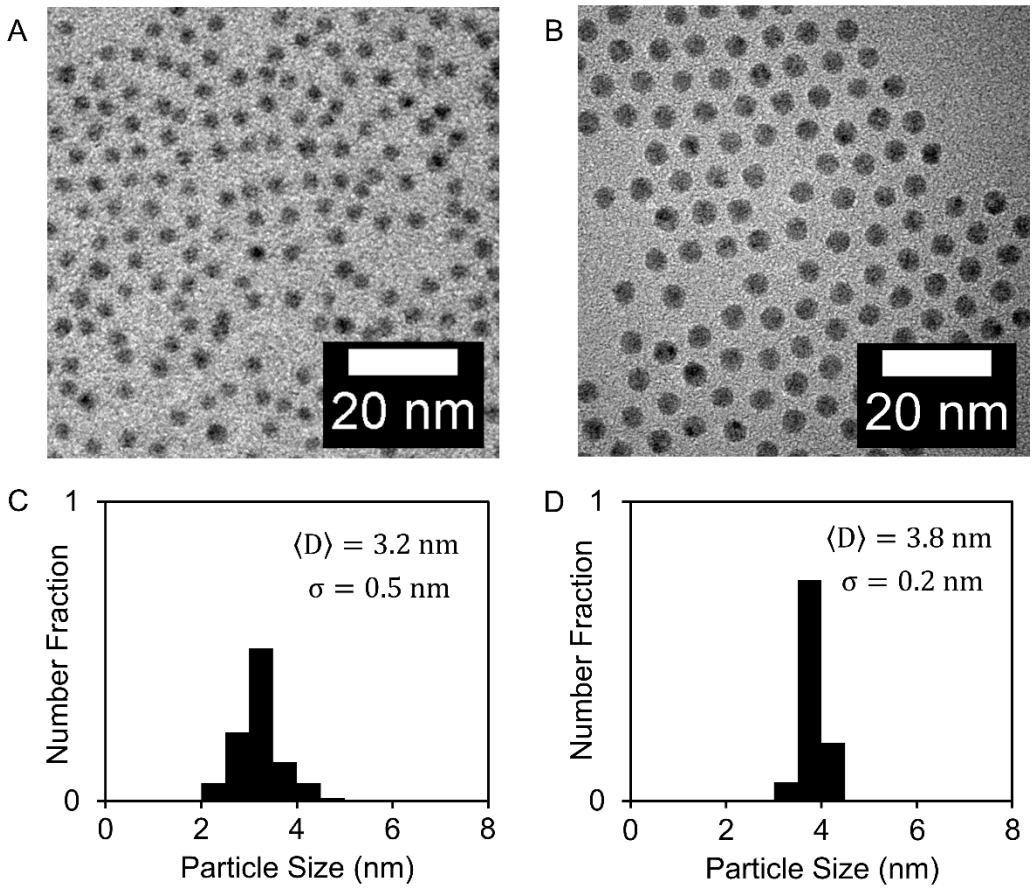

Figure S1. (A) TEM micrograph of unsupported Au NPs and **(B)** of Pd NPs. (Reproduced from main text). **(C)** NP size distribution of Au NPs and **(D)** of Pd NPs.

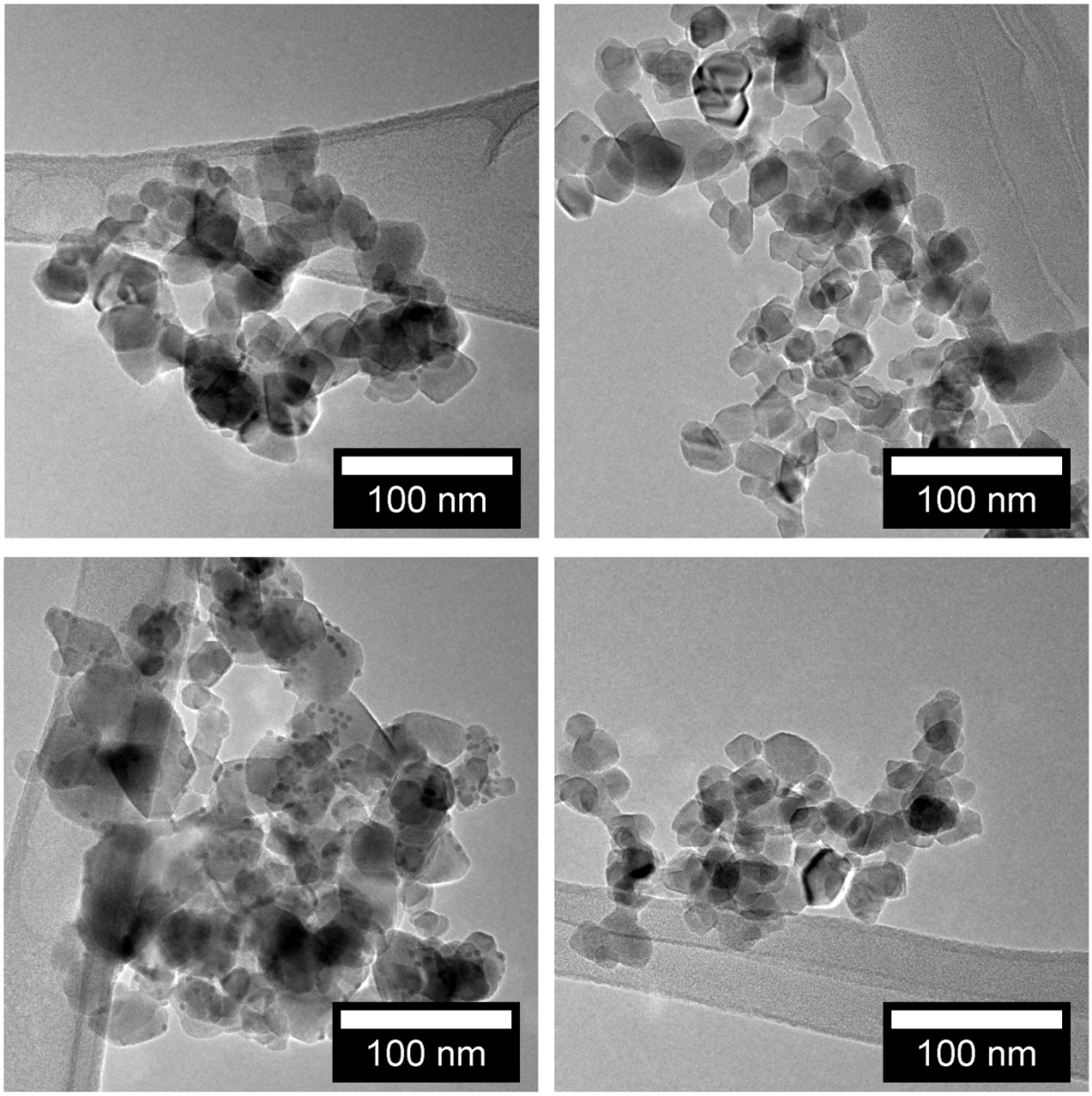

Figure S2. TEM micrographs to illustrate approximate sizes of the TiO_2 grains used in this study. Images are of the Pd-TiO_2-C sample.

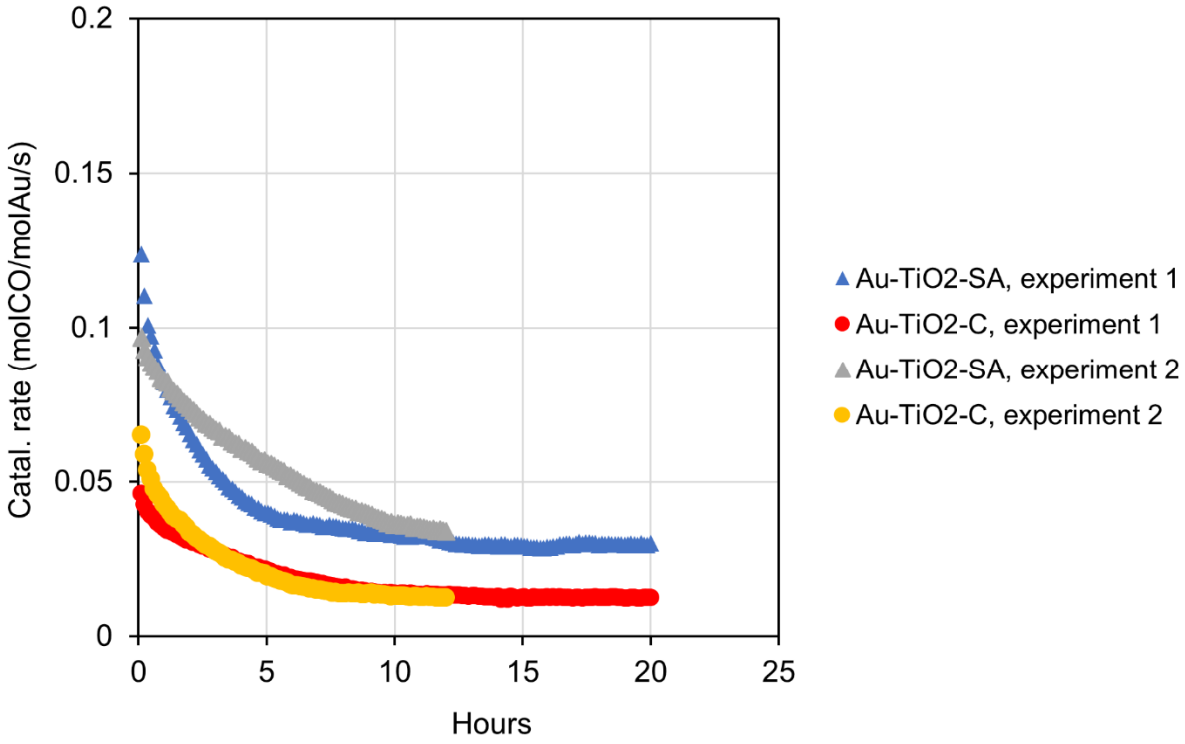

Figure S3. Repeat experiments measuring transient CO oxidation rates on Au-TiO_2-SA and Au-TiO_2-C. Curves from experiment 1 are reproduced from the main text, Figure 3 A.

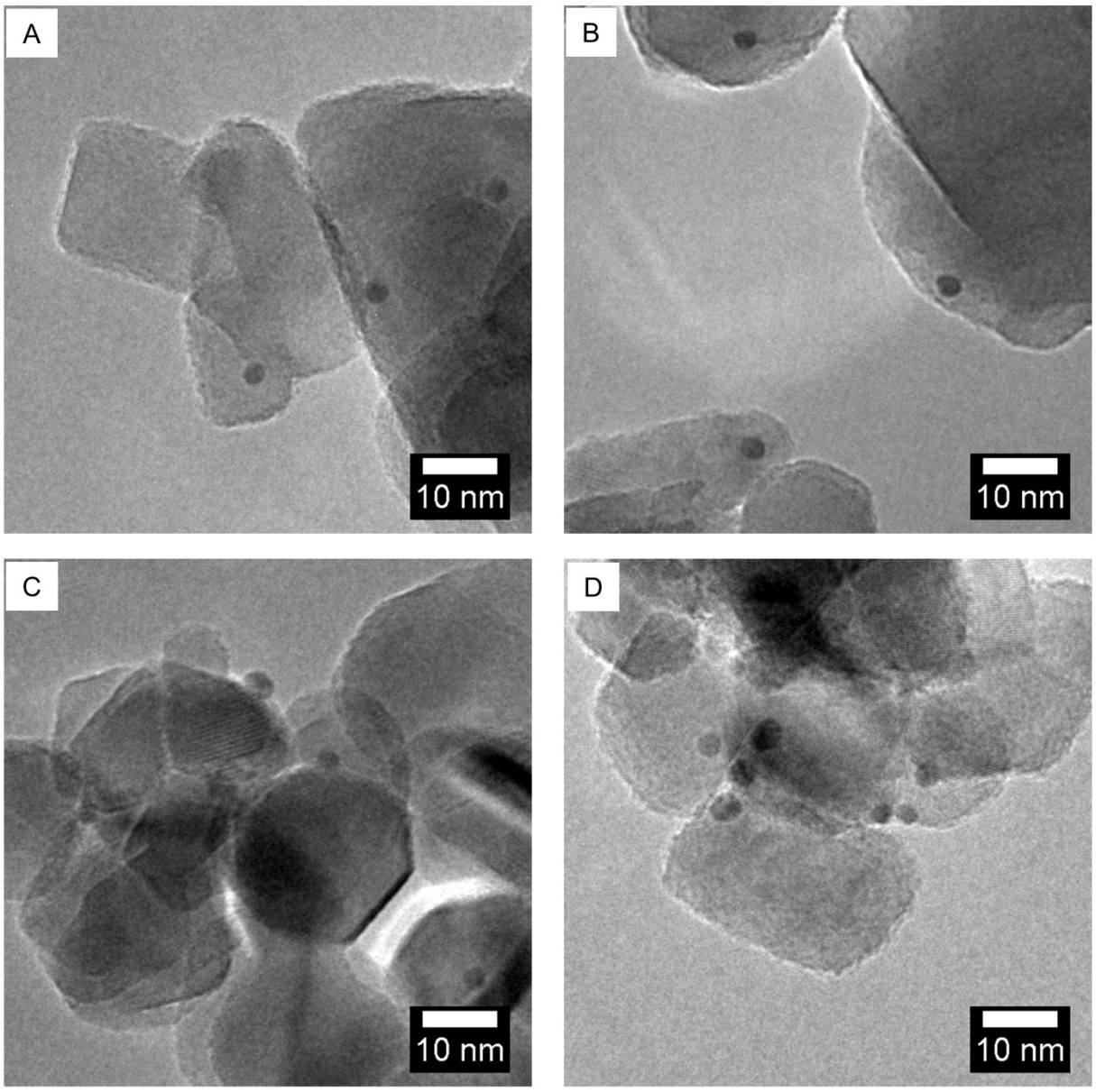

Figure S4. (A) Typical TEM image of Au-TiO_2-SA before catalysis. **(B)** Typical TEM image of Au-TiO_2-SA after catalysis. **(C)** Typical TEM image of Au-TiO_2-C before catalysis. **(D)** Typical TEM image of Au-TiO_2-C after catalysis.

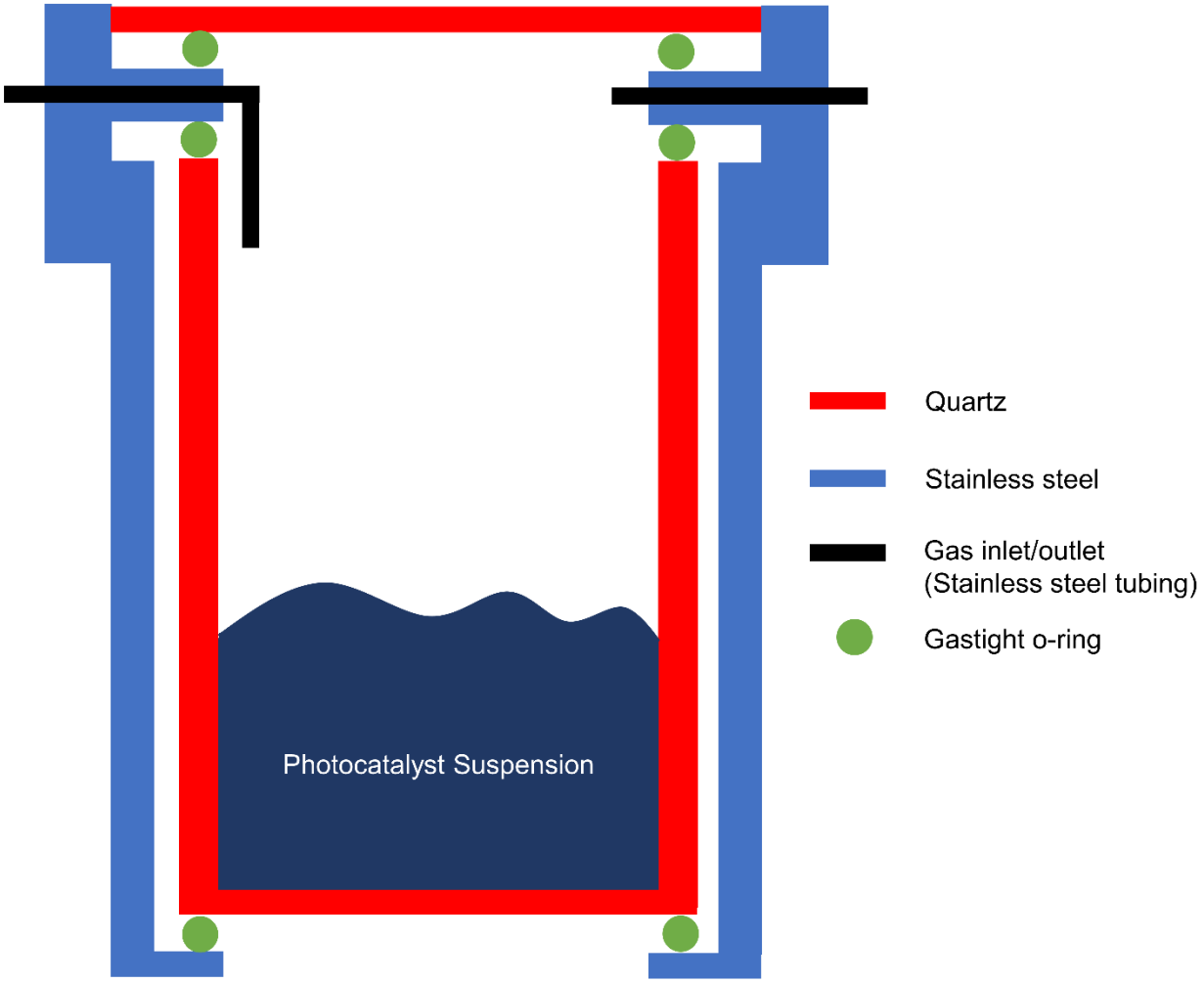

Figure S5. Schematic drawing of the custom-made quartz photoreactor used in this study.

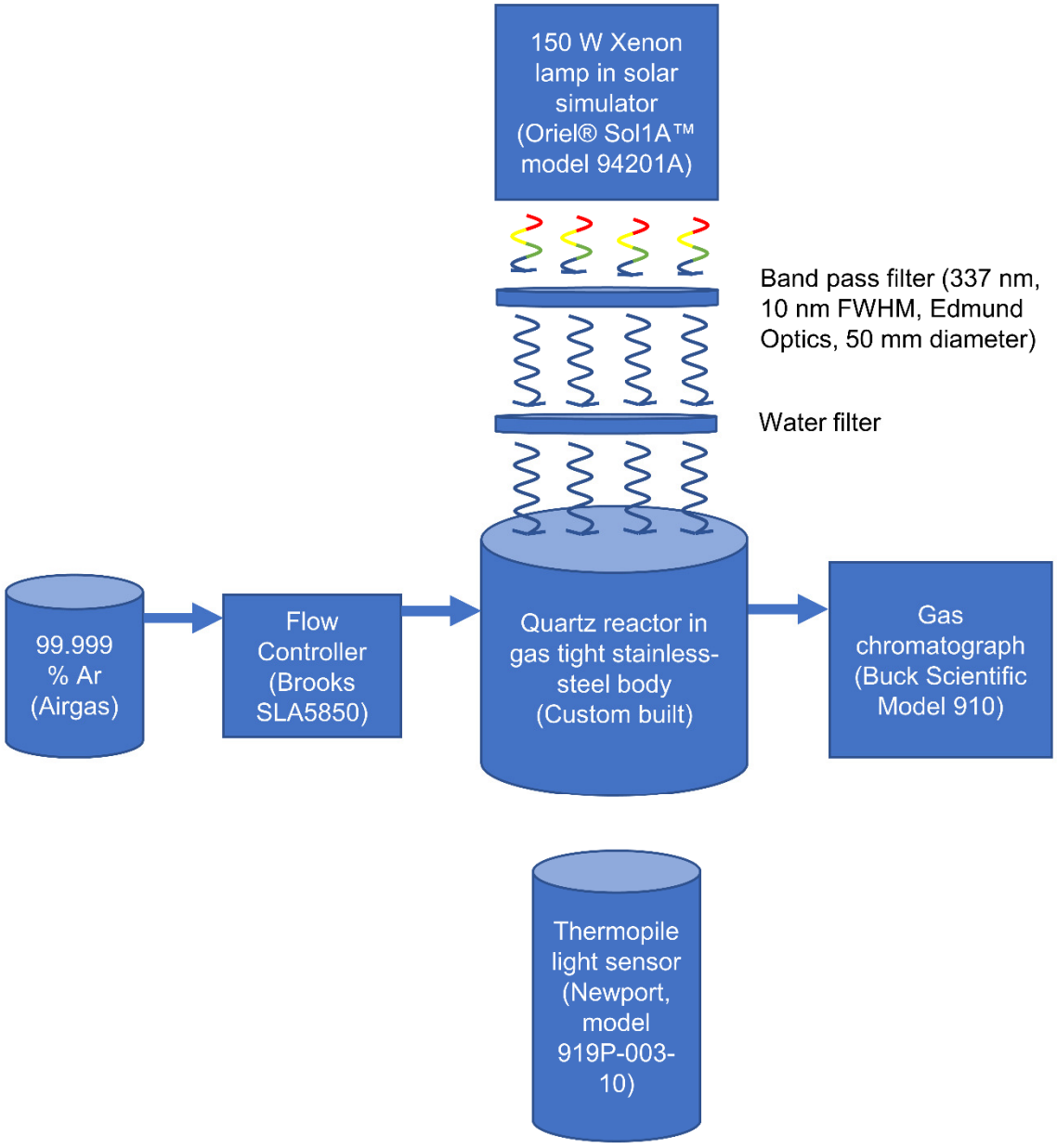

Figure S6. Schematic of the set-up used for photocatalysis measurements. The quartz photoreactor was illustrated in Figure S5.

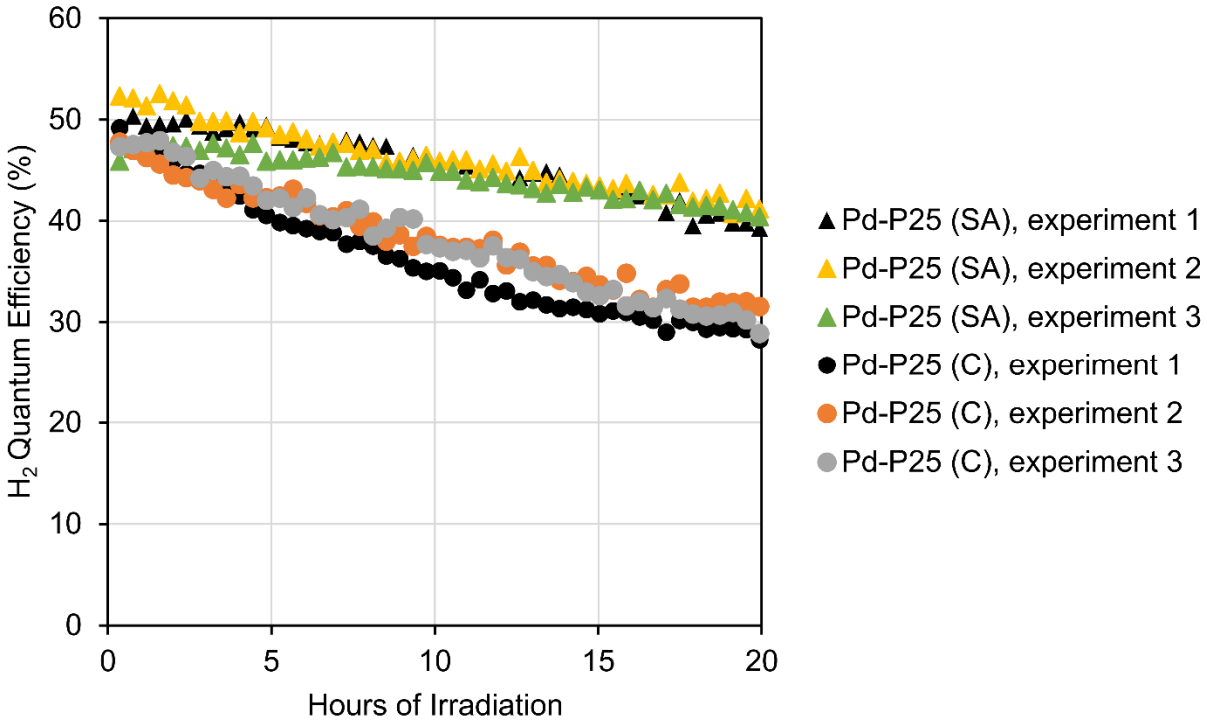

Figure S7. Repeat experiments measuring transient photocatalytic quantum efficiencies of H_2 production with Pd-TiO_2-SA and Pd-TiO_2-C. Curves from experiment 1 (black markers) are reproduced from the main text, Figure 5 A.

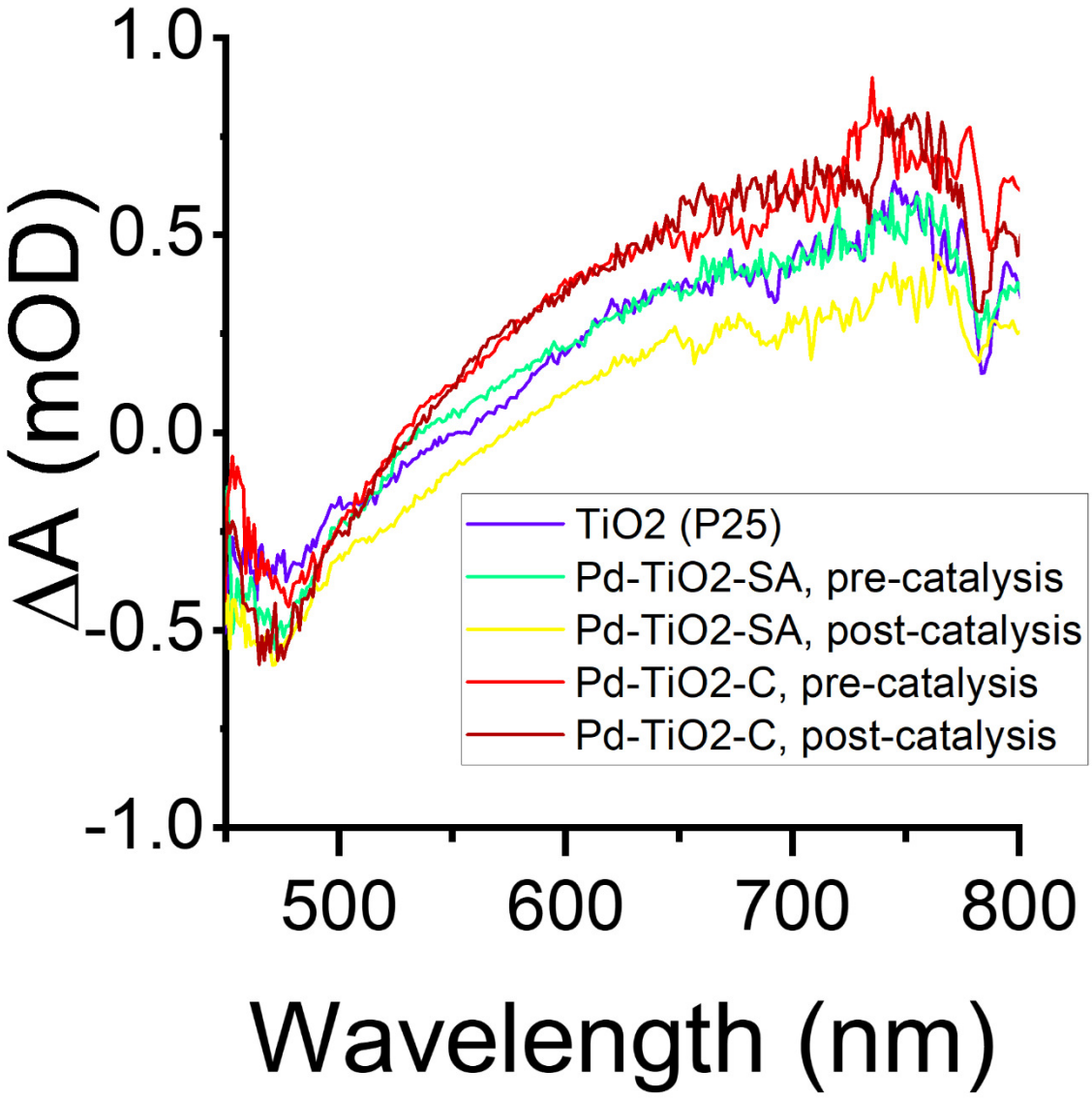

Figure S8. Absorption spectra at 50 ps delay time in 1:1 water:ethanol of pure TiO_2, Pd-TiO_2-SA and Pd-TiO_2-C before and after photocatalysis.

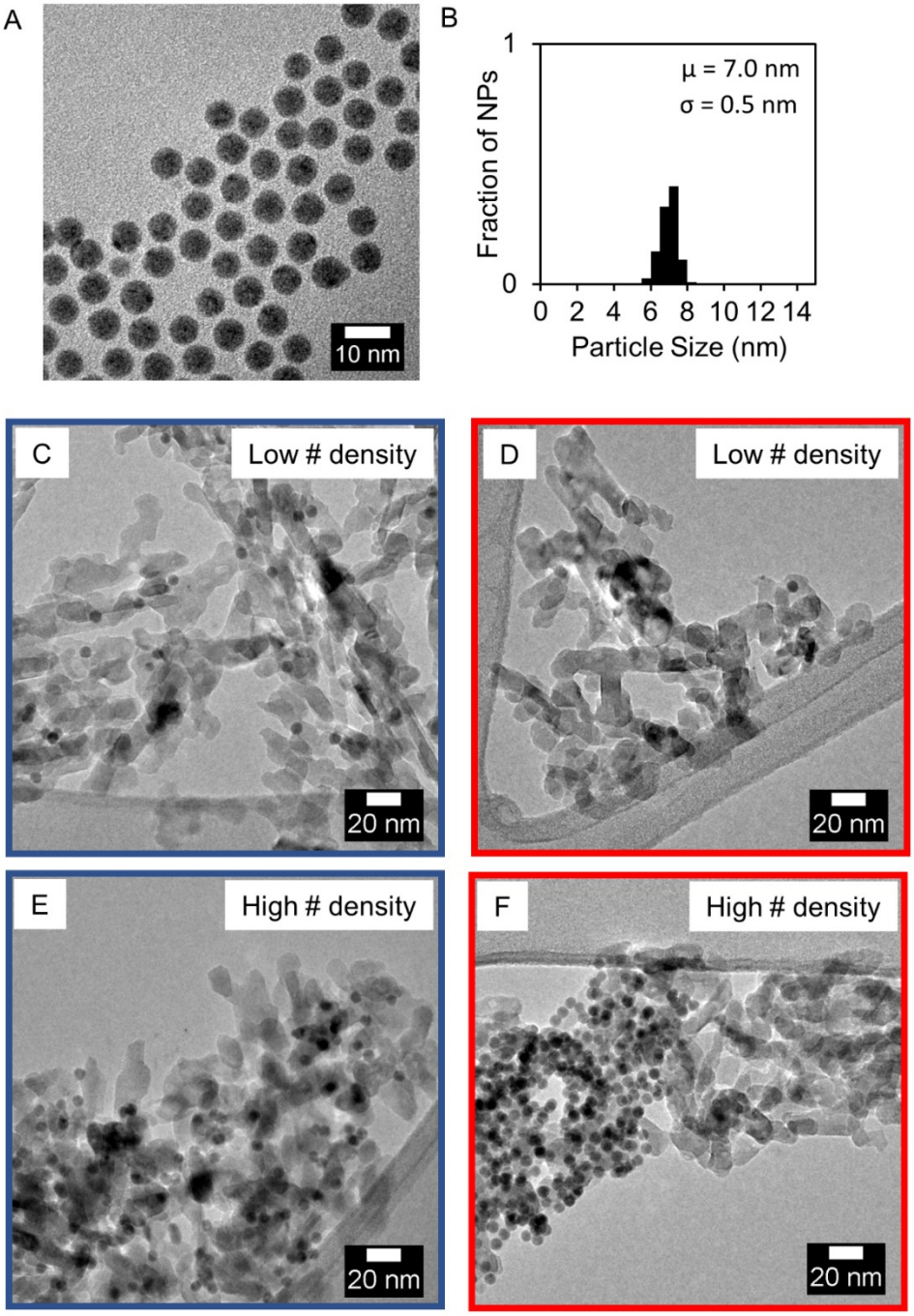

Figure S9. (A) TEM micrograph of Pd NPs used for impregnation onto Al_2O_3. Note that a different batch of Pd NPs (7.0 nm +/- 0.5 nm) were used compared to the Pd NPs described in the main text (Figure 1 B). The fact that uniform depositions were obtained with the surfactant-assisted deposition further establishes the generality of the protocol. **(B)** NP size distribution. **(C, E)** Typical TEM micrographs of Pd-Al_2O_3-SA prepared by the surfactant-assisted method exemplifying regions with low and high NP number-density. The NPs are uniformly distributed in this sample. Pd weight loading by ICP-MS was 0.80 wt. %. **(D, F)** Typical TEM micrographs of Pd-Al_2O_3-C prepared by the conventional method exemplifying regions with low and high NP

number-density. The NPs are non-uniformly distributed in this sample. Pd weight loading by ICP-MS was 1.0 wt. %.

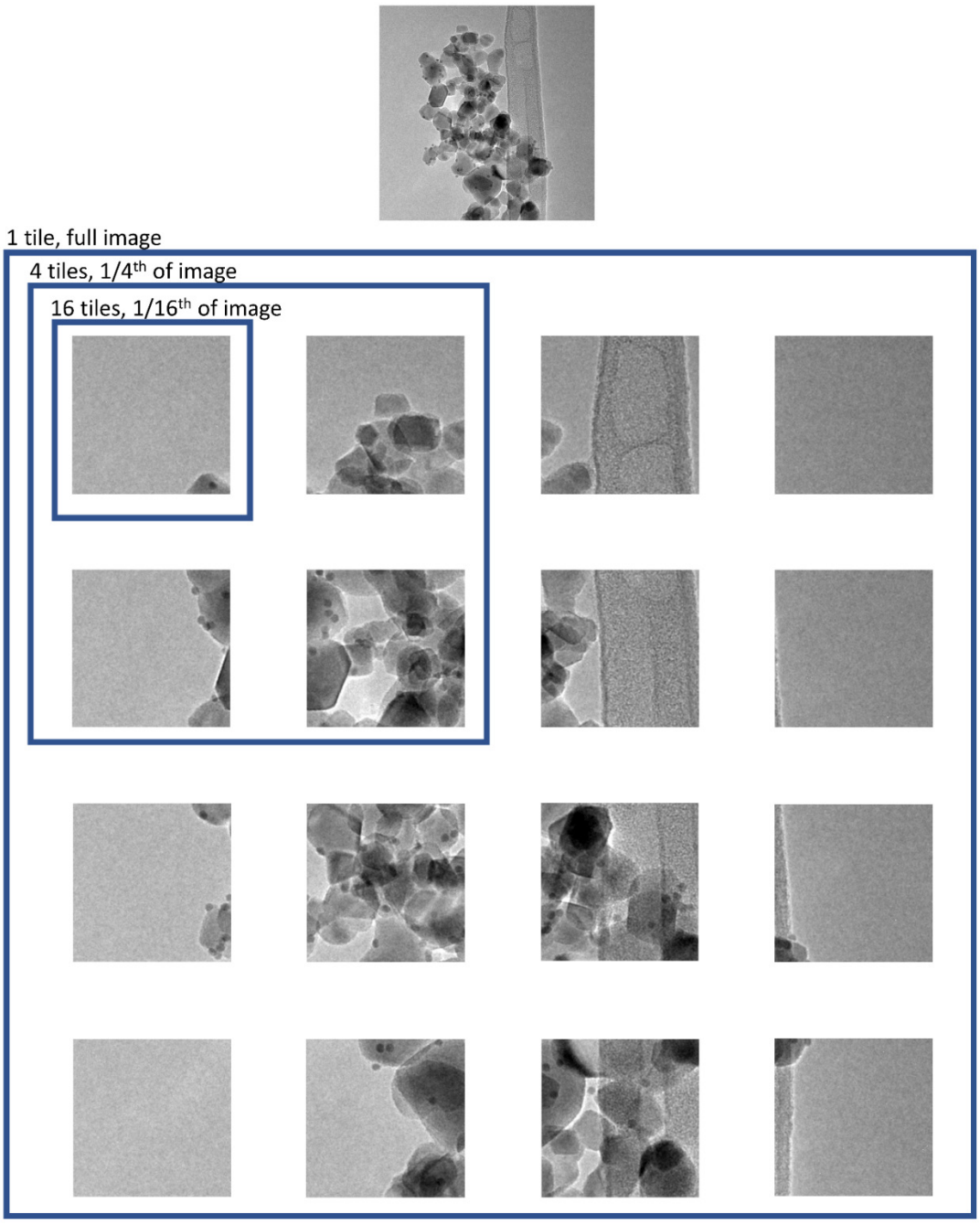

Figure S10. Illustration of how each image was subdivided into 1, 4 or 16 tiles before NP number-density was determined. Number-densities were determined for the entire grain (projected area within full image, 1 tile); for sections of the grain each within 1/4th of the image; or for sections of the grain each within 1/16th of the image. The tiling was the same for all images. The image used for illustration is of Pd-TiO_2-C, but the subdivision of images used for the other samples is analogous.

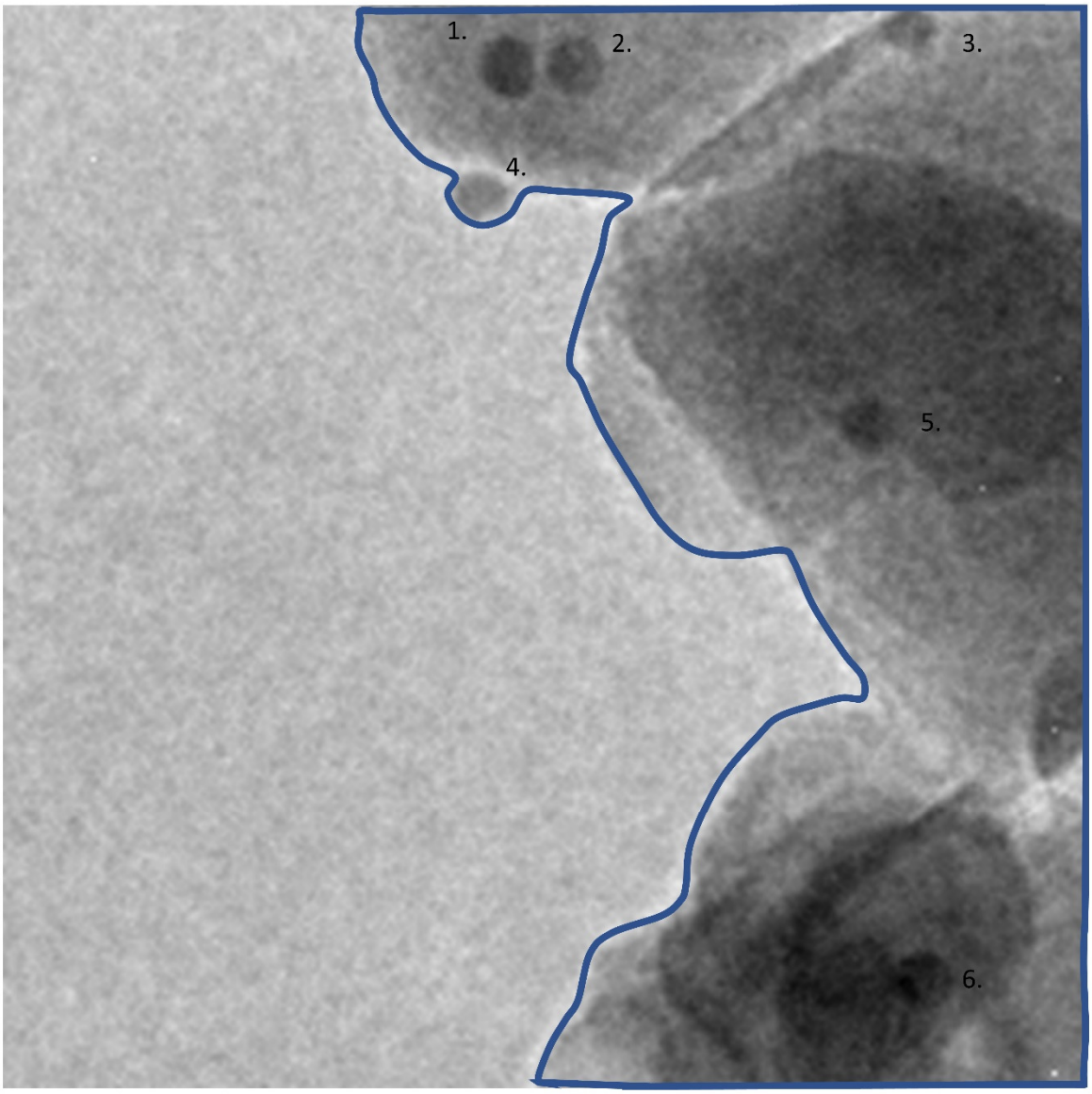

Number of Pd NPs: 6
Projected Area: 0.0026 μm^2
NP number density: 6/0.0026 = 2300 NPs μm^{-2}

Figure S11. Illustration of determination of NP number-density in one bin. Particles are counted, projected grain area measured, and NP number-density determined as the ratio: number of particles / projected grain area. The image used for illustration is of Pd-TiO_2-C (it is a tile taken from Figure S10), but the determination of NP number-density is analogous for all samples.

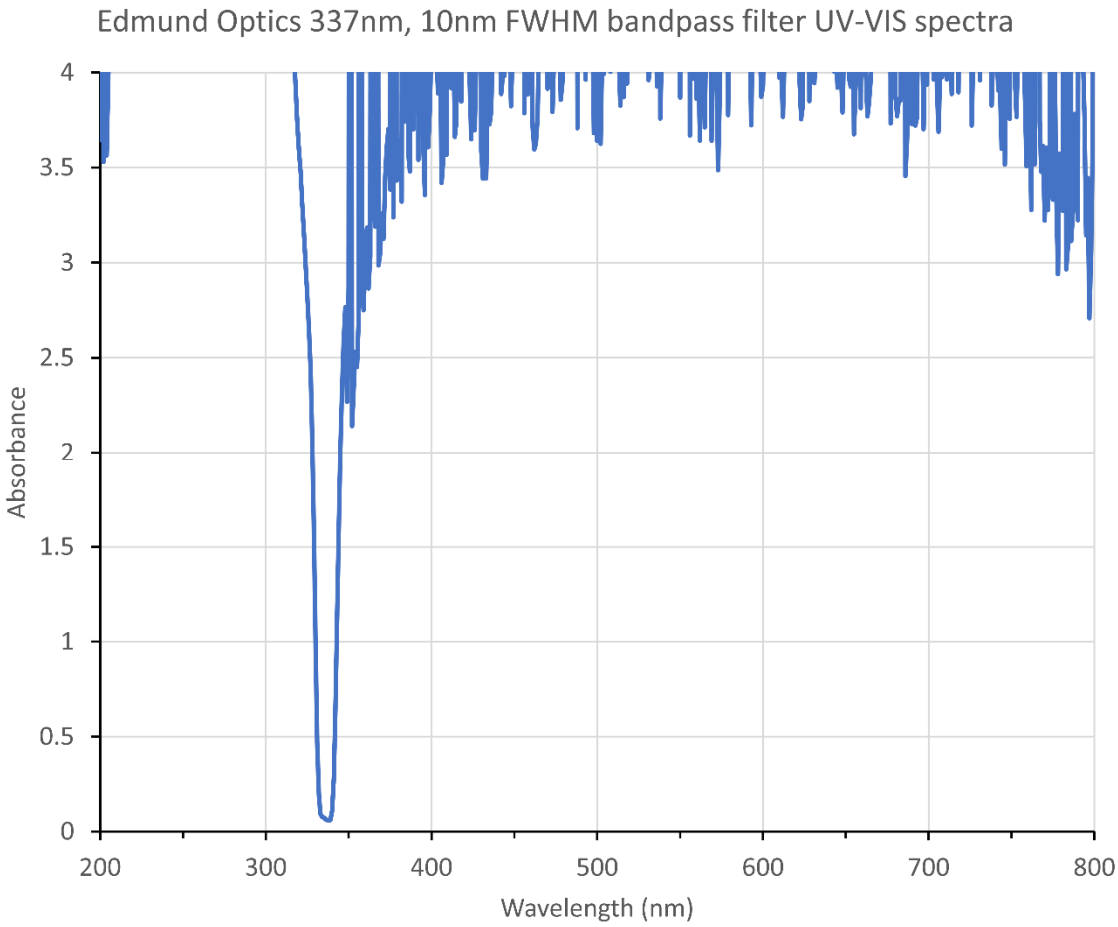

Figure S12. UV-Vis spectrum of the bandpass filter (337 nm, 10 nm FWHM, Edmund Optics, 50 mm diameter) used in the photoreactor set-up (Figure S6).

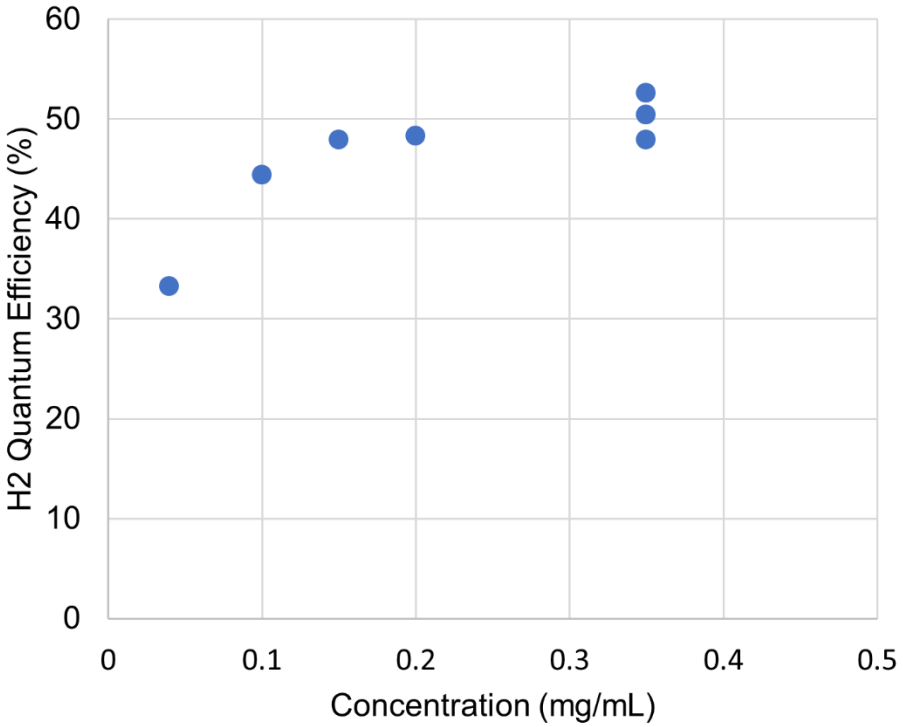

Figure S13. Variation of quantum efficiency with concentration of Pd-TiO_2-SA catalyst. The quantum efficiency at 0.35 mg/mL was measured in three independent experiments.

Distribution Fit (2/29/2020 02:50:28)

Notes

Input Data

Descriptive Statistics

	N	Missing	Mean	Standard Deviation	SE of mean	Lower 95% CI of Mean	Upper 95% CI of Mean
A	43	0	1099.83631	340.8191	51.97443	994.94768	1204.72495

Quantiles

Parameter Estimates

	Distribution	Parameter	Estimate	Lower 95%	Upper 95%
A	Normal	Location mu	1099.83631	997.96831	1201.70432
		Scale sigma	340.8191	274.8479	422.62524
	Lognormal	Location mu	6.94413	6.83127	7.05699
		Scale sigma	0.3776	0.30451	0.46823
	Weibull	Scale alpha	1217.51683	1113.67194	1331.04479
		Shape beta	3.52544	2.81868	4.40941
	Exponential	Mean theta	1099.83631	815.6823	1482.97925
	Gamma	Shape alpha	8.66898	5.72552	13.12565
		Scale theta	126.87032	82.77344	194.45947

Goodness-of-Fit Tests

	Distribution	Goodness of Fit tests	Statistics	P-value	Decision at level(5%)
A	Normal	K-S test	0.08873	0.96009	Can't reject Normal
		K-S modified test	0.08873	>0.15	Can't reject Normal
		A-D test	0.44117	0.27693	Can't reject Normal
	Lognormal	K-S test	0.14151	0.3255	Can't reject Lognormal
		K-S modified test	0.13478	0.04877	Reject Lognormal
		A-D test	1.51101	5.81711E-4	Reject Lognormal
	Weibull	K-S modified test	0.09234	>0.1	Can't reject Weibull
		A-D test	0.53669	0.17725	Can't reject Weibull
	Exponential	K-S test	0.41512	3.18438E-7	Reject Exponential
		K-S modified test	0.39186	<=0.01	Reject Exponential
		A-D test	9.75829	5.82242E-7	Reject Exponential
	Gamma	K-S test	0.12049	0.53079	Can't reject Gamma
		K-S modified test	0.11135	>0.25	Can't reject Gamma
		A-D test	0.96654	0.01634	Reject Gamma

Histogram

A

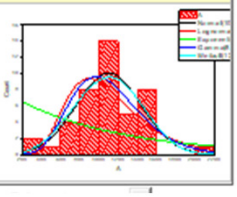

Figure S14. Report of distribution fit in OriginPro of distribution of NP number-density in Au-TiO_2-SA (1 tile, bin size 0.01 μm^2 – 0.07 μm^2).

Notes

Input Data

Descriptive Statistics

	N	Missing	Mean	Standard Deviation	SE of mean	Lower 95% CI of Mean	Upper 95% CI of Mean
B	43	0	1114.36924	628.12455	95.7881	921.06104	1307.67744

Quantiles

Parameter Estimates

	Distribution	Parameter	Estimate	Lower 95%	Upper 95%
B	Normal	Location mu	1114.36924	926.62802	1302.11046
		Scale sigma	628.12455	506.5406	778.89206
	Lognormal	Location mu	6.86849	6.70201	7.03496
		Scale sigma	0.55698	0.44916	0.69067
	Weibull	Scale alpha	1263.33998	1071.53992	1489.47126
		Shape beta	1.92419	1.5419	2.40127
	Exponential	Mean theta	1114.36924	826.46049	1502.57492
	Gamma	Shape alpha	3.54651	2.36687	5.31406
		Scale theta	314.21581	203.49806	485.17208

Goodness-of-Fit Tests

	Distribution	Goodness of Fit tests	Statistics	P-value	Decision at level(5%)
B	Normal	K-S test	0.17263	0.13676	Can't reject Normal
		K-S modified test	0.17263	<=0.01	Reject Normal
		A-D test	1.298	0.00198	Reject Normal
	Lognormal	K-S test	0.07704	1	Can't reject Lognormal
		K-S modified test	0.0755	>0.15	Can't reject Lognormal
		A-D test	0.16468	0.93705	Can't reject Lognormal
	Weibull	K-S modified test	0.12978	>0.1	Can't reject Weibull
		A-D test	0.56452	0.15086	Can't reject Weibull
	Exponential	K-S test	0.27082	0.00282	Reject Exponential
		K-S modified test	0.24757	<=0.01	Reject Exponential
		A-D test	4.55469	4.69669E-5	Reject Exponential
	Gamma	K-S test	0.10151	0.77247	Can't reject Gamma
		K-S modified test	0.11187	>0.25	Can't reject Gamma
		A-D test	0.29529	>=0.25	Can't reject Gamma

Histogram

B

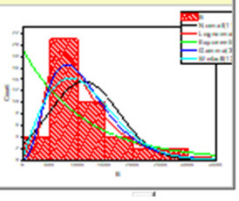

Figure S15. Report of distribution fit in OriginPro of distribution of NP number-density in Au-TiO_2-C (1 tile, bin size 0.01 μm^2 – 0.07 μm^2).

Notes

Input Data

Descriptive Statistics

	N	Missing	Mean	Standard Deviation	SE of mean	Lower 95% CI of Mean	Upper 95% CI of Mean
A	120	0	1099.86937	499.379	45.58686	1009.60284	1190.1359

Quantiles

Parameter Estimates

	Distribution	Parameter	Estimate	Lower 95%	Upper 95%
A	Normal	Location mu	1099.86937	1010.52077	1189.21797
		Scale sigma	499.379	439.68211	567.18111
	Lognormal	Location mu	6.89075	6.80001	6.98149
		Scale sigma	0.50717	0.44654	0.57603
	Weibull	Scale alpha	1240.70844	1143.57992	1346.08645
		Shape beta	2.31678	2.03192	2.64158
	Exponential	Mean theta	1099.86937	919.68138	1315.36058
	Gamma	Shape alpha	4.61652	3.61541	5.89484
		Scale theta	238.24648	184.02545	308.44312

Goodness-of-Fit Tests

	Distribution	Goodness of Fit tests	Statistics	P-value	Decision at level(5%)
A	Normal	K-S test	0.07998	0.41995	Can't reject Normal
		K-S modified test	0.07998	0.05886	Can't reject Normal
		A-D test	0.82297	0.03265	Reject Normal
	Lognormal	K-S test	0.10592	0.1295	Can't reject Lognormal
		K-S modified test	0.09758	<=0.01	Reject Lognormal
		A-D test	1.56771	4.67847E-4	Reject Lognormal
	Weibull	K-S modified test	0.06563	>0.1	Can't reject Weibull
		A-D test	0.57427	0.14808	Can't reject Weibull
	Exponential	K-S test	0.27979	1.01306E-8	Reject Exponential
		K-S modified test	0.27146	<=0.01	Reject Exponential
		A-D test	17.48191	0	Reject Exponential
	Gamma	K-S test	0.07275	0.54975	Can't reject Gamma
		K-S modified test	0.06751	0.24833	Can't reject Gamma
		A-D test	0.59301	0.14023	Can't reject Gamma

Histogram

A

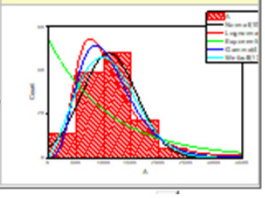

Figure S16. Report of distribution fit in OriginPro of distribution of NP number-density in Au-TiO_2-SA (4 tiles, bin size 0.0035 μm^2 – 0.02 μm^2).

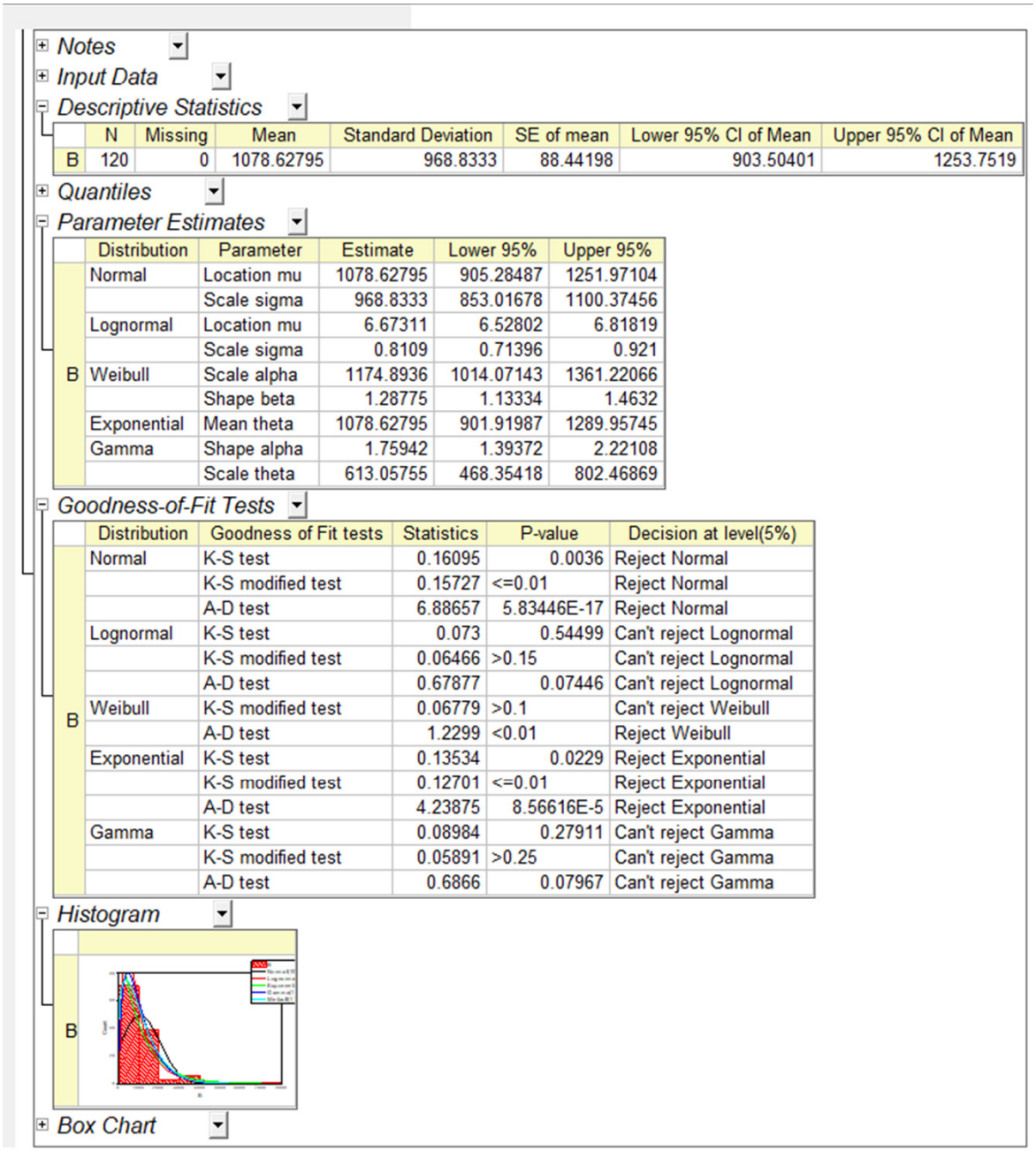

Notes

Input Data

Descriptive Statistics

	N	Missing	Mean	Standard Deviation	SE of mean	Lower 95% CI of Mean	Upper 95% CI of Mean
B	120	0	1078.62795	968.8333	88.44198	903.50401	1253.7519

Quantiles

Parameter Estimates

	Distribution	Parameter	Estimate	Lower 95%	Upper 95%
B	Normal	Location mu	1078.62795	905.28487	1251.97104
		Scale sigma	968.8333	853.01678	1100.37456
	Lognormal	Location mu	6.67311	6.52802	6.81819
		Scale sigma	0.8109	0.71396	0.921
	Weibull	Scale alpha	1174.8936	1014.07143	1361.22066
		Shape beta	1.28775	1.13334	1.4632
	Exponential	Mean theta	1078.62795	901.91987	1289.95745
	Gamma	Shape alpha	1.75942	1.39372	2.22108
		Scale theta	613.05755	468.35418	802.46869

Goodness-of-Fit Tests

	Distribution	Goodness of Fit tests	Statistics	P-value	Decision at level(5%)
B	Normal	K-S test	0.16095	0.0036	Reject Normal
		K-S modified test	0.15727	<=0.01	Reject Normal
		A-D test	6.88657	5.83446E-17	Reject Normal
	Lognormal	K-S test	0.073	0.54499	Can't reject Lognormal
		K-S modified test	0.06466	>0.15	Can't reject Lognormal
		A-D test	0.67877	0.07446	Can't reject Lognormal
	Weibull	K-S modified test	0.06779	>0.1	Can't reject Weibull
		A-D test	1.2299	<0.01	Reject Weibull
	Exponential	K-S test	0.13534	0.0229	Reject Exponential
		K-S modified test	0.12701	<=0.01	Reject Exponential
		A-D test	4.23875	8.56616E-5	Reject Exponential
	Gamma	K-S test	0.08984	0.27911	Can't reject Gamma
		K-S modified test	0.05891	>0.25	Can't reject Gamma
		A-D test	0.6866	0.07967	Can't reject Gamma

Histogram

B

Box Chart

Figure S17. Report of distribution fit in OriginPro of distribution of NP number-density in Au-TiO_2-C (4 tiles, bin size 0.0035 μm^2 – 0.02 μm^2).

Notes

Input Data

Descriptive Statistics

	N	Missing	Mean	Standard Deviation	SE of mean	Lower 95% CI of Mean	Upper 95% CI of Mean
A	156	0	1129.96098	635.12737	50.85089	1029.51079	1230.41117

Quantiles

Parameter Estimates

	Distribution	Parameter	Estimate	Lower 95%	Upper 95%
A	Normal	Location mu	1129.96098	1030.29507	1229.62689
		Scale sigma	635.12737	568.11684	710.04192
	Lognormal	Location mu	6.84693	6.74304	6.95083
		Scale sigma	0.66208	0.59222	0.74017
	Weibull	Scale alpha	1273.72006	1165.58954	1391.88175
		Shape beta	1.86453	1.6535	2.10248
	Exponential	Mean theta	1129.96098	965.85689	1321.94721
	Gamma	Shape alpha	2.88802	2.34012	3.5642
		Scale theta	391.25763	310.94747	492.30994

Goodness-of-Fit Tests

	Distribution	Goodness of Fit tests	Statistics	P-value	Decision at level(5%)
A	Normal	K-S test	0.10046	0.08239	Can't reject Normal
		K-S modified test	0.10046	<=0.01	Reject Normal
		A-D test	1.65259	2.92837E-4	Reject Normal
	Lognormal	K-S test	0.1227	0.01717	Reject Lognormal
		K-S modified test	0.11629	<=0.01	Reject Lognormal
		A-D test	2.41815	3.8427E-6	Reject Lognormal
	Weibull	K-S modified test	0.05456	>0.1	Can't reject Weibull
		A-D test	0.42509	>=0.25	Can't reject Weibull
	Exponential	K-S test	0.2218	3.54657E-7	Reject Exponential
		K-S modified test	0.21539	<=0.01	Reject Exponential
		A-D test	13.81914	0	Reject Exponential
	Gamma	K-S test	0.06878	0.44852	Can't reject Gamma
		K-S modified test	0.07498	0.04586	Reject Gamma
		A-D test	0.70317	0.07288	Can't reject Gamma

Histogram

A

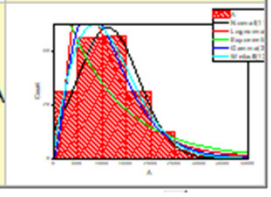

Figure S18. Report of distribution fit in OriginPro of distribution of NP number-density in Au-TiO_2-SA (16 tiles, bin size 0.0035 μm^2 – 0.006 μm^2).

Notes

Input Data

Descriptive Statistics

	N	Missing	Mean	Standard Deviation	SE of mean	Lower 95% CI of Mean	Upper 95% CI of Mean
B	156	0	1172.89983	1301.52102	104.20508	967.05446	1378.7452

Quantiles

Parameter Estimates

	Distribution	Parameter	Estimate	Lower 95%	Upper 95%
B	Normal	Location mu	1172.89983	968.66163	1377.13803
		Scale sigma	1301.52102	1164.20114	1455.03805
	Lognormal	Location mu	6.66759	6.52709	6.8081
		Scale sigma	0.89537	0.8009	1.00098
	Weibull	Scale alpha	1229.07497	1058.81137	1426.71803
		Shape beta	1.1163	0.99933	1.24695
	Exponential	Mean theta	1172.89983	1002.55973	1372.18159
	Gamma	Shape alpha	1.39429	1.14052	1.70454
		Scale theta	841.21442	661.13981	1070.33594

Goodness-of-Fit Tests

	Distribution	Goodness of Fit tests	Statistics	P-value	Decision at level(5%)
B	Normal	K-S test	0.21438	9.85373E-7	Reject Normal
		K-S modified test	0.20797	<=0.01	Reject Normal
		A-D test	12.61973	2.6208E-30	Reject Normal
	Lognormal	K-S test	0.05993	0.64285	Can't reject Lognormal
		K-S modified test	0.05352	>0.15	Can't reject Lognormal
		A-D test	0.73304	0.05493	Can't reject Lognormal
	Weibull	K-S modified test	0.08412	>0.1	Can't reject Weibull
		A-D test	2.07925	<0.01	Reject Weibull
	Exponential	K-S test	0.1234	0.01627	Reject Exponential
		K-S modified test	0.11699	<=0.01	Reject Exponential
		A-D test	3.11534	7.37618E-4	Reject Exponential
	Gamma	K-S test	0.16864	2.50175E-4	Reject Gamma
		K-S modified test	0.07764	0.03241	Reject Gamma
		A-D test	1.60991	<0.005	Reject Gamma

Histogram

B

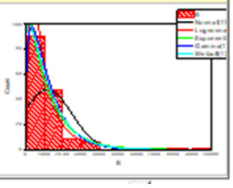

Figure S19. Report of distribution fit in OriginPro of distribution of NP number-density in Au-TiO_2-C (16 tiles, bin size 0.0035 μm^2 – 0.006 μm^2).

Distribution Fit (1/2/2020 01:52:16)

Notes

Input Data

Descriptive Statistics

	N	Missing	Mean	Standard Deviation	SE of mean	Lower 95% CI of Mean	Upper 95% CI of Mean
B	43	0	2142.27083	657.65797	100.2919	1939.87358	2344.66808

Quantiles

Parameter Estimates

	Distribution	Parameter	Estimate	Lower 95%	Upper 95%
B	Normal	Location mu	2142.27083	1945.70232	2338.83934
		Scale sigma	657.65797	530.35734	815.51433
	Lognormal	Location mu	7.6164	7.51164	7.72116
		Scale sigma	0.35048	0.28264	0.43461
	Weibull	Scale alpha	2373.63578	2170.75695	2595.47566
		Shape beta	3.5282	2.82457	4.4071
	Exponential	Mean theta	2142.27083	1588.79314	2888.56
	Gamma	Shape alpha	9.55849	6.30852	14.48275
		Scale theta	224.12235	146.28623	343.37359

Goodness-of-Fit Tests

	Distribution	Goodness of Fit tests	Statistics	P-value	Decision at level(5%)
B	Normal	K-S test	0.09772	0.82641	Can't reject Normal
		K-S modified test	0.09772	>0.15	Can't reject Normal
		A-D test	0.31824	0.52452	Can't reject Normal
	Lognormal	K-S test	0.11675	0.57439	Can't reject Lognormal
		K-S modified test	0.09349	>0.15	Can't reject Lognormal
		A-D test	0.91975	0.01762	Reject Lognormal
	Weibull	K-S modified test	0.1061	>0.1	Can't reject Weibull
		A-D test	0.42921	>=0.25	Can't reject Weibull
	Exponential	K-S test	0.38744	2.54283E-6	Reject Exponential
		K-S modified test	0.36418	<=0.01	Reject Exponential
		A-D test	9.86134	5.80724E-7	Reject Exponential
	Gamma	K-S test	0.08865	0.96127	Can't reject Gamma
		K-S modified test	0.08559	>0.25	Can't reject Gamma
		A-D test	0.55201	0.17359	Can't reject Gamma

Histogram

B

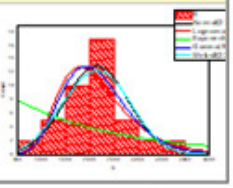

Figure S20. Report of distribution fit in OriginPro of distribution of NP number-density in Pd-TiO_2-SA (1 tile, bin size 0.01 μm^2 – 0.07 μm^2).

Notes

Input Data

Descriptive Statistics

	N	Missing	Mean	Standard Deviation	SE of mean	Lower 95% CI of Mean	Upper 95% CI of Mean
A	43	0	1813.10083	2516.75204	383.80109	1038.55887	2587.64278

Quantiles

Parameter Estimates

	Distribution	Parameter	Estimate	Lower 95%	Upper 95%
A	Normal	Location mu	1813.10083	1060.86452	2565.33714
		Scale sigma	2516.75204	2029.59284	3120.84312
	Lognormal	Location mu	6.79314	6.41774	7.16853
		Scale sigma	1.25596	1.01285	1.55742
	Weibull	Scale alpha	1646.2773	1134.45402	2389.01614
		Shape beta	0.85088	0.683	1.06001
	Exponential	Mean theta	1813.10083	1344.66759	2444.71915
	Gamma	Shape alpha	0.83204	0.577	1.1998
		Scale theta	2179.1138	1333.28341	3561.53609

Goodness-of-Fit Tests

	Distribution	Goodness of Fit tests	Statistics	P-value	Decision at level(5%)
A	Normal	K-S test	0.25253	0.00665	Reject Normal
		K-S modified test	0.25253	<=0.01	Reject Normal
		A-D test	4.88537	2.6496E-12	Reject Normal
	Lognormal	K-S test	0.07437	1	Can't reject Lognormal
		K-S modified test	0.05247	>0.15	Can't reject Lognormal
		A-D test	0.1833	0.90476	Can't reject Lognormal
	Weibull	K-S modified test	0.11171	>0.1	Can't reject Weibull
		A-D test	0.60001	0.1172	Can't reject Weibull
	Exponential	K-S test	0.15803	0.20985	Can't reject Exponential
		K-S modified test	0.15803	0.06851	Can't reject Exponential
		A-D test	1.28859	0.05263	Can't reject Exponential
	Gamma	K-S test	0.16119	0.1919	Can't reject Gamma
		K-S modified test	0.13433	0.07926	Can't reject Gamma
		A-D test	0.81124	0.04518	Reject Gamma

Histogram

A

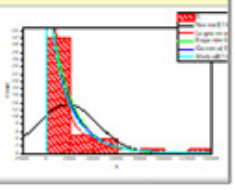

Figure S21. Report of distribution fit in OriginPro of distribution of NP number-density in Pd-TiO_2-C (1 tile, bin size 0.01 μm^2 – 0.07 μm^2).

Notes

Input Data

Descriptive Statistics

	N	Missing	Mean	Standard Deviation	SE of mean	Lower 95% CI of Mean	Upper 95% CI of Mean
B	128	0	2087.37308	810.18629	71.61103	1945.66778	2229.07838

Quantiles

Parameter Estimates

	Distribution	Parameter	Estimate	Lower 95%	Upper 95%
B	Normal	Location mu	2087.37308	1947.01805	2227.72812
		Scale sigma	810.18629	716.25936	916.43037
	Lognormal	Location mu	7.55031	7.46764	7.63299
		Scale sigma	0.47724	0.42191	0.53982
	Weibull	Scale alpha	2342.45863	2194.39389	2500.51391
		Shape beta	2.79143	2.43727	3.19705
	Exponential	Mean theta	2087.37308	1755.35023	2482.19774
	Gamma	Shape alpha	5.51757	4.34915	6.9999
		Scale theta	378.31369	294.88896	485.33945

Goodness-of-Fit Tests

	Distribution	Goodness of Fit tests	Statistics	P-value	Decision at level(5%)
B	Normal	K-S test	0.06775	0.6064	Can't reject Normal
		K-S modified test	0.06775	>0.15	Can't reject Normal
		A-D test	0.47895	0.23122	Can't reject Normal
	Lognormal	K-S test	0.11269	0.07363	Can't reject Lognormal
		K-S modified test	0.10488	<=0.01	Reject Lognormal
		A-D test	2.11827	2.06554E-5	Reject Lognormal
	Weibull	K-S modified test	0.05559	>0.1	Can't reject Weibull
		A-D test	0.34529	>=0.25	Can't reject Weibull
	Exponential	K-S test	0.32321	3.20149E-12	Reject Exponential
		K-S modified test	0.3154	<=0.01	Reject Exponential
		A-D test	21.58724	0	Reject Exponential
	Gamma	K-S test	0.05779	0.83932	Can't reject Gamma
		K-S modified test	0.07156	0.1401	Can't reject Gamma
		A-D test	0.82008	0.03769	Reject Gamma

Histogram

B

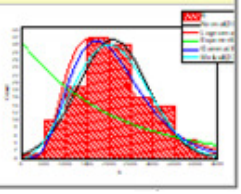

Figure S22. Report of distribution fit in OriginPro of distribution of NP number-density in Pd-TiO_2-SA (4 tiles, bin size 0.0035 μm^2 – 0.02 μm^2).

Notes

Input Data

Descriptive Statistics

	N	Missing	Mean	Standard Deviation	SE of mean	Lower 95% CI of Mean	Upper 95% CI of Mean
A	140	0	1833.95998	2971.04048	251.09875	1337.49313	2330.42684

Quantiles

Parameter Estimates

	Distribution	Parameter	Estimate	Lower 95%	Upper 95%
A	Normal	Location mu	1833.95998	1341.81547	2326.10449
		Scale sigma	2971.04048	2640.97825	3342.35298
	Lognormal	Location mu	6.63178	6.41126	6.85229
		Scale sigma	1.33123	1.18334	1.4976
	Weibull	Scale alpha	1493.05627	1182.08894	1885.82853
		Shape beta	0.75314	0.66755	0.84971
	Exponential	Mean theta	1833.95998	1553.99706	2164.36008
	Gamma	Shape alpha	0.68669	0.56264	0.83809
		Scale theta	2670.72968	2013.98625	3541.63144

Goodness-of-Fit Tests

	Distribution	Goodness of Fit tests	Statistics	P-value	Decision at level(5%)
A	Normal	K-S test	0.27444	1.02729E-9	Reject Normal
		K-S modified test	0.26729	<=0.01	Reject Normal
		A-D test	18.83332	3.21997E-44	Reject Normal
	Lognormal	K-S test	0.04883	1	Can't reject Lognormal
		K-S modified test	0.04883	>0.15	Can't reject Lognormal
		A-D test	0.4302	0.30379	Can't reject Lognormal
	Weibull	K-S modified test	0.10401	>0.1	Can't reject Weibull
		A-D test	2.45289	<0.01	Reject Weibull
	Exponential	K-S test	0.21202	5.70815E-6	Reject Exponential
		K-S modified test	0.21202	<=0.01	Reject Exponential
		A-D test	10.56784	0	Reject Exponential
	Gamma	K-S test	0.22095	1.90436E-6	Reject Gamma
		K-S modified test	0.14069	<=0.005	Reject Gamma
		A-D test	3.95794	<0.005	Reject Gamma

Histogram

A

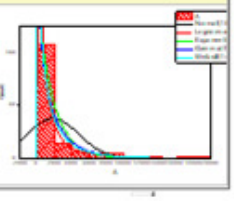

Figure S23. Report of distribution fit in OriginPro of distribution of NP number-density in Pd-TiO_2-C (4 tiles, bin size 0.0035 μm^2 – 0.02 μm^2).

Notes

Input Data

Descriptive Statistics

	N	Missing	Mean	Standard Deviation	SE of mean	Lower 95% CI of Mean	Upper 95% CI of Mean
B	191	0	2144.79848	1039.32271	75.20275	1996.45893	2293.13803

Quantiles

Parameter Estimates

	Distribution	Parameter	Estimate	Lower 95%	Upper 95%
B	Normal	Location mu	2144.79848	1997.40379	2292.19317
		Scale sigma	1039.32271	939.78202	1149.40665
	Lognormal	Location mu	7.53452	7.45435	7.61469
		Scale sigma	0.56528	0.51114	0.62516
	Weibull	Scale alpha	2423.98874	2263.90649	2595.3905
		Shape beta	2.18863	1.9621	2.44133
	Exponential	Mean theta	2144.79848	1861.21143	2471.59481
	Gamma	Shape alpha	3.82759	3.15749	4.63992
		Scale theta	560.35159	456.18827	688.29894

Goodness-of-Fit Tests

	Distribution	Goodness of Fit tests	Statistics	P-value	Decision at level(5%)
B	Normal	K-S test	0.05627	0.5892	Can't reject Normal
		K-S modified test	0.05627	0.1437	Can't reject Normal
		A-D test	1.17189	0.00453	Reject Normal
	Lognormal	K-S test	0.08358	0.13492	Can't reject Lognormal
		K-S modified test	0.07834	<=0.01	Reject Lognormal
		A-D test	1.87099	8.56934E-5	Reject Lognormal
	Weibull	K-S modified test	0.03764	>0.1	Can't reject Weibull
		A-D test	0.23473	>=0.25	Can't reject Weibull
	Exponential	K-S test	0.25996	9.38356E-12	Reject Exponential
		K-S modified test	0.25472	<=0.01	Reject Exponential
		A-D test	22.74583	0	Reject Exponential
	Gamma	K-S test	0.03928	1	Can't reject Gamma
		K-S modified test	0.0437	>0.25	Can't reject Gamma
		A-D test	0.46804	>=0.25	Can't reject Gamma

Histogram

B

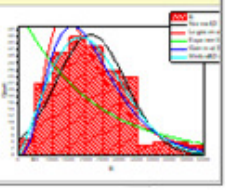

Figure S24. Report of distribution fit in OriginPro of distribution of NP number-density in Pd-TiO_2-SA (16 tiles, bin size 0.0035 μm^2 – 0.006 μm^2).

Notes

Input Data

Descriptive Statistics

	N	Missing	Mean	Standard Deviation	SE of mean	Lower 95% CI of Mean	Upper 95% CI of Mean
A	228	0	1818.75604	3415.00767	226.16441	1373.10597	2264.40611

Quantiles

Parameter Estimates

	Distribution	Parameter	Estimate	Lower 95%	Upper 95%
A	Normal	Location mu	1818.75604	1375.48195	2262.03014
		Scale sigma	3415.00767	3114.57466	3744.42056
	Lognormal	Location mu	6.4952	6.32085	6.66954
		Scale sigma	1.34317	1.22501	1.47273
	Weibull	Scale alpha	1340.98691	1100.09031	1634.63478
		Shape beta	0.69729	0.63555	0.76502
	Exponential	Mean theta	1818.75604	1597.35796	2070.84049
	Gamma	Shape alpha	0.60986	0.52262	0.71168
		Scale theta	2982.23301	2376.95151	3741.6471

Goodness-of-Fit Tests

	Distribution	Goodness of Fit tests	Statistics	P-value	Decision at level(5%)
A	Normal	K-S test	0.31182	7.52933E-20	Reject Normal
		K-S modified test	0.30743	<=0.01	Reject Normal
		A-D test	36.32475	8.47975E-80	Reject Normal
	Lognormal	K-S test	0.12697	0.0012	Reject Lognormal
		K-S modified test	0.12258	<=0.01	Reject Lognormal
		A-D test	5.29287	4.19615E-13	Reject Lognormal
	Weibull	K-S modified test	0.18501	<=0.01	Reject Weibull
		A-D test	8.43265	<0.01	Reject Weibull
	Exponential	K-S test	0.27039	4.95659E-15	Reject Exponential
		K-S modified test	0.27039	<=0.01	Reject Exponential
		A-D test	33.70093	0	Reject Exponential
	Gamma	K-S test	0.37592	1.1719E-28	Reject Gamma
		K-S modified test	0.17723	<=0.005	Reject Gamma
		A-D test	12.26119	<0.005	Reject Gamma

Histogram

A

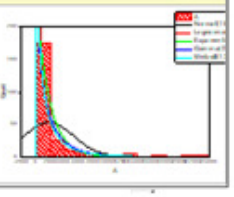

Figure S25. Report of distribution fit in OriginPro of distribution of NP number-density in Pd-TiO_2-C (16 tiles, bin size 0.0035 μm^2 – 0.006 μm^2).

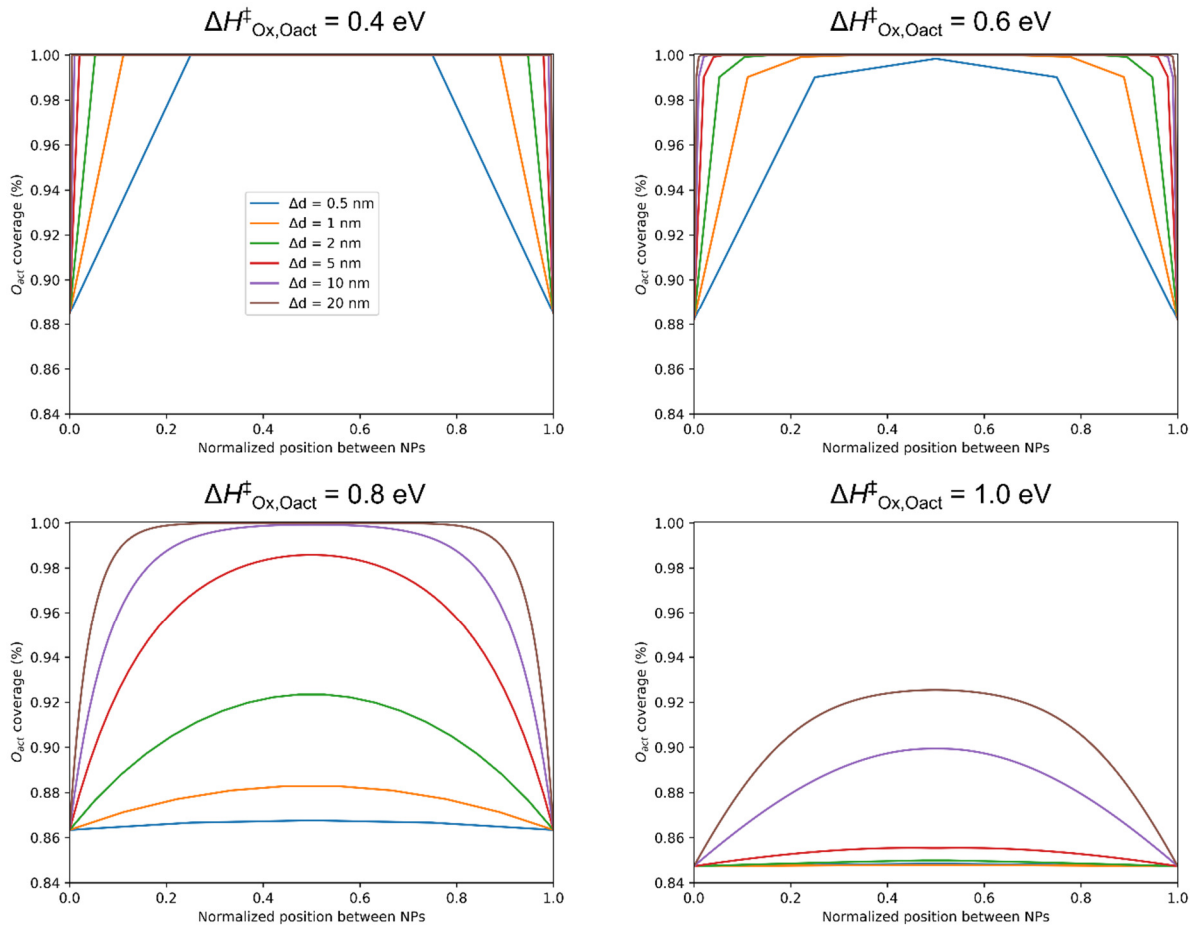

Figure S26. Steady-state O_{act} concentration profiles obtained with the microkinetic model for varied NP separation and varied activation barrier ($\Delta H^{\ddagger}_{Ox,Oact}$) for the O_{act} surface reoxidation reaction (reaction R4 in Table S2).

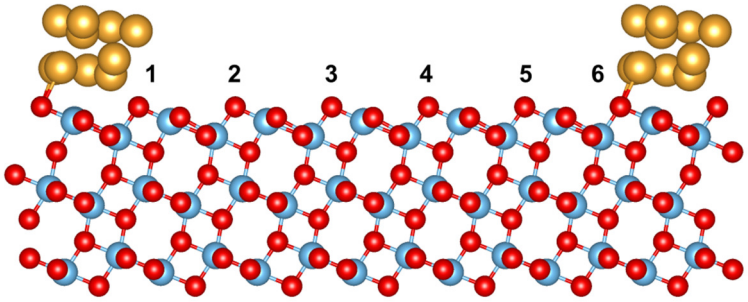

Figure S27. Side-view of the model surface of TiO_2 (101) including an Au nanorod used in the DFT calculations. The surface O-positions included in the vacancy formation calculations of Table S5 are enumerated.

REFERENCES

(1) Jurić, M.; Ivezić, Ž.; Brooks, A.; Lupton, R. H.; Schlegel, D.; Finkbeiner, D.; Padmanabhan, N.; Bond, N.; Sesar, B.; Rockosi, C. M.; Knapp, G. R.; Gunn, J. E.; Sumi, T.; Schneider, D. P.; Barentine, J. C.; Brewington, H. J.; Brinkmann, J.; Fukugita, M.; Harvanek, M.; Kleinman, S. J.; Krzesinski, J.; Long, D.; Neilsen, Jr., E. H.; Nitta, A.; Snedden, S. A.; York, D. G. The Milky Way Tomography with SDSS. I. Stellar Number Density Distribution. Astrophys. J. 2008, 673 (2), 864–914.

(2) Fessler, J. R.; Kulick, J. D.; Eaton, J. K. Preferential Concentration of Heavy Particles in a Turbulent Channel Flow. Phys. Fluids 1994, 6 (11), 3742–3749.

(3) Grami, A. Probability , Random Variables , Statistics , and Random Processes; JohnWiley & Sons, Inc.: Hoboken, NJ, USA, 2020.

(4) Lotz, A.; Kendzia, B.; Gawrych, K.; Lehnert, M.; Brüning, T.; Pesch, B. Statistical Methods for the Analysis of Left-Censored Variables. Dtsch. Gesellschaft fur Medizinische Inform. Biometrie und Epidemiol. e.V. 2013, 9 (2), 1–7.

(5) Ross, S. M. Introduction to Probability and Statistics for Engineers and Scientists, 5th ed.; Academic Press: Waltham, MA 02451, USA, 2014.

(6) Widmann, D.; Behm, R. J. Dynamic Surface Composition in a Mars-van Krevelen Type Reaction: CO Oxidation on Au/TiO2. J. Catal. 2018, 357, 263–273.

(7) Ohtani, B.; Prieto-Mahaney, O. O.; Li, D.; Abe, R. What Is Degussa (Evonic) P25? Crystalline Composition Analysis, Reconstruction from Isolated Pure Particles and Photocatalytic Activity Test. J. Photochem. Photobiol. A Chem. 2010, 216 (2–3), 179–182.

(8) Hengerer, R.; Bolliger, B.; Erbudak, M.; Grätzel, M. Structure and Stability of the Anatase TiO2 (101) and (001) Surfaces. Surf. Sci. 2000, 460 (1–3), 162–169.

(9) Turković, A.; Dubček, P.; Fox, N. D. Self-Organization of Nanoparticles in a TiO2 Thin Film on a Glass Substrate. Vacuum 2005, 80 (1–3), 108–112.

(10) Campbell, C. T.; Árnadóttir, L.; Sellers, J. R. V. Kinetic Prefactors of Reactions on Solid Surfaces. Zeitschrift fur Phys. Chemie 2013, 227 (11), 1435–1454.

(11) Schlexer, P.; Widmann, D.; Behm, R. J.; Pacchioni, G. CO Oxidation on a Au/TiO2 Nanoparticle Catalyst via the Au-Assisted Mars-van Krevelen Mechanism. ACS Catal. 2018, 8 (7), 6513–6525.

(12) Wang, Y. G.; Cantu, D. C.; Lee, M. S.; Li, J.; Glezakou, V. A.; Rousseau, R. CO Oxidation on Au/TiO2: Condition-Dependent Active Sites and Mechanistic Pathways. J. Am. Chem. Soc. 2016, 138 (33), 10467–10476.

(13) Scheiber, P.; Fidler, M.; Dulub, O.; Schmid, M.; Diebold, U.; Hou, W.; Aschauer, U.; Selloni, A. (Sub)Surface Mobility of Oxygen Vacancies at the TiO 2 Anatase (101) Surface. Phys. Rev. Lett. 2012, 109 (13), 1–5.

(14) Cheng, H.; Selloni, A. Energetics and Diffusion of Intrinsic Surface and Subsurface Defects on Anatase TiO2 (101). J. Chem. Phys. 2009, 131 (5).

(15) Li, Y. F.; Aschauer, U.; Chen, J.; Selloni, A. Adsorption and Reactions of O2 on Anatase TiO2. Acc. Chem. Res. 2014, 47 (11), 3361–3368.

(16) Grimme, S.; Antony, J.; Ehrlich, S.; Krieg, H. A Consistent and Accurate Ab Initio Parametrization of Density Functional Dispersion Correction (DFT-D) for the 94 Elements H-Pu. J. Chem. Phys. 2010, 132 (15), 154104.

(17) Grimme, S.; Ehrlich, S.; Goerigk, L. Effect of the Damping Function in Dispersion Corrected Density Functional Theory. J. Comput. Chem. 2011, 32 (7), 1456–1465.

(18) Aschauer, U.; Chen, J.; Selloni, A. Peroxide and Superoxide States of Adsorbed O2 on Anatase TiO2 (101) with Subsurface Defects. Phys. Chem. Chem. Phys. 2010, 12 (40), 12956–12960.

(19) Frisch, M. J. et Al. Gaussian16 Revision B.01. (2016).

(20) Xia, X.; Naumann D'Alnoncourt, R.; Muhler, M. Entropy of Adsorption of Carbon Monoxide on Energetically Heterogeneous Surfaces. J. Therm. Anal. Calorim. 2008, 91 (1), 167–172.

(21) Frank, O.; Zukalova, M.; Laskova, B.; Kürti, J.; Koltai, J.; Kavan, L. Raman Spectra of Titanium Dioxide (Anatase, Rutile) with Identified Oxygen Isotopes (16, 17, 18). Phys. Chem. Chem. Phys. 2012, 14 (42), 14567–14572.